การหาขอบเขตของมะเร็งหลอดอาหารในภาพเพ็ท/ซีทีด้วยการเลื่อนค่าระดับกั้นของโอซึและแอ็กทีฟคอนทัวร์

นายกิติวัฒน์ คำวัน

วิทยานิพนธ์นี้เป็นส่วนหนึ่งของการศึกษาตามหลักสูตรปริญญาวิทยาศาสตรดุษฎีบัณฑิต
สาขาวิชาวิศวกรรมชีวเวช (สหสาขาวิชา)
คณะวิศวกรรมศาสตร์ จุฬาลงกรณ์มหาวิทยาลัย
ปีการศึกษา 2554
ลิขสิทธิ์ของจุฬาลงกรณ์มหาวิทยาลัย

บทคัดย่อและแฟ้มข้อมูลฉบับเต็มของวิทยานิพนธ์ตั้งแต่ปีการศึกษา 2554 ที่ให้บริการในคลังปัญญาจุฬาฯ (CUIR)
เป็นแฟ้มข้อมูลของนิสิตเจ้าของวิทยานิพนธ์ที่ส่งผ่านทางบัณฑิตวิทยาลัย
The abstract and full text of theses from the academic year 2011 in Chulalongkorn University Intellectual Repository(CUIR)
are the thesis authors' files submitted through the Graduate School.

DETERMINATION OF MALIGNANT TUMOR BOUNDARY IN ESOPHAGEAL CANCER USING SHIFTED OTSU THRESHOLD AND ACTIVE CONTOUR ON PET/CT IMAGES

Mr. Kitiwat Khamwan

A Dissertation Submitted in Partial Fulfillment of the Requirements
for the Degree of Doctor of Philosophy Program in Biomedical Engineering
(Interdisciplinary Program)
Faculty of Engineering
Chulalongkorn University
Academic Year 2011
Copyright of Chulalongkorn University

Thesis Title	DETERMINATION OF MALIGNANT TUMOR BOUNDARY IN ESOPHAGEAL CANCER USING SHIFTED OTSU THRESHOLD AND ACTIVE CONTOUR ON PET/CT IMAGES
By	Mr.Kitiwat Khamwan
Field of Study	Biomedical Engineering
Thesis Advisor	Associate Professor Anchali Krisanachinda, Ph.D.
Thesis Co-advisor	Assistant Professor Charnchai Pluempitiwiriyawej, Ph.D.

Accepted by the Faculty of Engineering, Chulalongkorn University in Partial Fulfillment of the Requirements for the Doctoral Degree

…….. Dean of the Faculty of Engineering
(Associate Professor Boonsom Lerdhirunwong, Dr.Ing.)

THESIS COMMITTEE

…….. Chairman
(Associate Professor Mana Sriyudthsak, D.Eng.)

……. Thesis Advisor
(Associate Professor Anchali Krisanachinda, Ph.D.)

…….. Thesis Co-advisor
(Assistant Professor Charnchai Pluempitiwiriyawej, Ph.D.)

…….. Examiner
(Associate Professor Tawatchai Chaiwatanarat, M.D.)

…….. Examiner
(Assistant Professor Supatana Auetavekiat, Ph.D.)

…….. External Examiner
(Associate Professor Malulee Tuntawiroon, M.Sc.)

กิติวัฒน์ คำวัน: การหาขอบเขตของมะเร็งหลอดอาหารในภาพเพ็ท/ซีทีด้วยการเลื่อนค่าระดับกั้นของโอซึและแอ็กทีฟคอนทัวร์. (DETERMINATION OF MALIGNANT TUMOR BOUNDARY IN ESOPHAGEAL CANCER USING SHIFTED OTSU THRESHOLD AND ACTIVE CONTOUR ON PET/CT IMAGES) อ.ที่ปรึกษาวิทยานิพนธ์หลัก: รศ.ดร.อัญชลี กฤษณจินดา, อ.ที่ปรึกษาวิทยานิพนธ์ร่วม: ผศ.ดร.ชาญชัย ปลื้มปิติวิริยะเวช, 90 หน้า.

วิทยานิพนธ์ฉบับนี้ได้นำเสนอการหาขอบเขตก้อนมะเร็งของหลอดอาหารในภาพเพ็ทด้วยระเบียบวิธีแอ็กทีฟคอนทัวร์แบบอาณาบริเวณร่วมกับค่าระดับกั้นที่เหมาะสม ซึ่งค่านี้หาได้จากค่าต่ำสุดที่อยู่ในช่วงระหว่างค่าระดับกั้นของโอซึ และค่าพิกเซลสูงสุดของภาพจากการกระจายของฮีสโตแกรม เมื่อนำไปคำนวณค่าถ่วงน้ำหนัก และฝังเข้าไปยังแรงภายนอกของแอ็กทีฟคอนทัวร์ ทำให้ทั้งสองวิธีนี้สามารถทำงานร่วมกันอย่างต่อเนื่องและมีประสิทธิภาพ ทำการทดสอบความสามารถของวิธีการที่พัฒนาขึ้นกับก้อนมะเร็งจำลองซึ่งมีปริมาตรตั้งแต่ 0.52 ถึง 26.53 ลูกบาศก์เซนติเมตร มีอัตราส่วนความเข้มข้นระหว่างก้อนมะเร็งและพื้นหลังที่แตกต่างกัน 4 อัตราส่วน ผลการทดลองพบว่า ปริมาตรของก้อนมะเร็งที่ได้จากการแบ่งส่วนภาพด้วยวิธีการ ที่พัฒนาขึ้น มีความถูกต้องมากกว่าแอ็กทีฟคอนทัวร์แบบเดิม แต่ความคลาดเคลื่อนจะเพิ่มมากขึ้นเมื่อก้อนมะเร็งมีขนาดเล็กลงและมีความแตกต่างของความเข้มข้นระหว่างก้อนมะเร็งและพื้นหลังลดลงที่ความเข้มข้น 16 เท่า และก้อนมะเร็งมีขนาดเส้นผ่านศูนย์กลาง 3.7 เซนติเมตร จะให้ค่าความคลาดเคลื่อนน้อยที่สุด ซึ่งมีค่าเท่ากับ 1.51 เปอร์เซ็นต์ ผลการทดสอบทางคลินิกในผู้ป่วยมะเร็งหลอดอาหารที่ทำการตรวจด้วยเพ็ท/ซีทีจำนวน 10 ราย พบว่าความแตกต่างระหว่างวิธีการวาดขอบเขตก้อนมะเร็งด้วยมือจากแพทย์ทางรังสีรักษากับวิธีการอัตโนมัติมีค่าเท่ากับ -4.06 ± 6.35 เปอร์เซ็นต์ ประโยชน์ของงานวิจัยนี้ไม่เพียงแต่จะช่วยเพิ่มความถูกต้องและความคงเส้นคงวาในการวาดขอบเขตของก้อนมะเร็งในภาพเพ็ท ยังสามารถใช้เป็นแนวทางสำหรับแพทย์รังสีรักษาเพื่อใช้ในการวางแผนการรักษา และเอื้อประโยชน์ในการวิเคราะห์ภาพเพ็ทสำหรับงานทางด้านคลินิก

สาขาวิชา วิศวกรรมชีวเวช ลายมือชื่อนิสิต .....

ปีการศึกษา 2554 ลายมือชื่อ อ.ที่ปรึกษาวิทยานิพนธ์หลัก .....

ลายมือชื่อ อ.ที่ปรึกษาวิทยานิพนธ์ร่วม .....

5187759621: MAJOR BIOMEDICAL ENGINEERING
KEYWORDS: POSITRON EMISSION TOMOGRAPHY / ACTIVE CONTOUR / OPTIMAL THRESHOLD/ TUMOR BOUNDARY DELINEATION

KITIWAT KHAMWAN: DETERMINATION OF MALIGNANT TUMOR BOUNDARY IN ESOPHAGEAL CANCER USING SHIFTED OTSU THRESHOLD AND ACTIVE CONTOUR ON PET/CT IMAGES. ADVISOR: ASSOC.PROF.ANCHALI KRISANACHINDA, Ph.D., CO-ADVISOR: ASST.PROF.CHARNCHAI PLUEMPITIWIRIYAWEJ, Ph.D., 90 pp.

This dissertation presents an automatic method to trace the boundary of the tumor in PET image. A double-stage threshold that locates the local minimum between the Otsu's threshold and the pixel with maximum intensity gray level within the image is proposed. The gray level in accordance with this scheme is chosen and embedded into the external force of a region-based active contour so that both algorithms are performed consecutively. The automated tumor contouring method is validated using the IEC/2001 torso phantom with six hot spheres (0.52-26.53 cc) insert and the variation of the source-to-background ratio (SBR). The results show that the tumor volumes segmented by automated algorithm are at higher accuracy than the traditional active contour. The accuracy of the detected volume is reduced in small sphere with low SBR. The least volume mismatch was at SBR 16 in the largest sphere (3.7 cm diameter) of 1.51 %. The average volume mismatch between the automated and manual method is -4.06 ± 6.35 % in clinically implemented with 10 esophageal cancer patients underwent whole-body ^{18}F-FDG PET/CT imaging. The advantage of the study is not only to improve the precision and accuracy of PET tumor contouring, but also to use by radiation oncologist for radiation therapy planning. Furthermore, this method can contribute to clinical PET image analysis.

Field of Study : Biomedical Engineering Student's Signature .....

Academic Year : 2011 Advisor's Signature .....

Co-advisor's Signature .....

ACKNOWLEDGEMENTS

The success of this dissertation depends on the contribution of many people. First of all, I wish to express gratitude and deepest appreciation to Associate Professor Dr.Anchali Krisanachinda, and Assistant Professor Dr.Charnchai Pluempitiwiriyawej, my supervisors, for their helpful, supervision, guidance, encouragement, polishing of the writing to improve the English expression and invaluable advice during my whole doctoral study.

I gratefully acknowledge the member of my dissertation committee: Associate Professor Dr.Mana Sriyudthsak, Associate Professor Tawatchai Chaiwatanarat, M.D., Assistant Professor Dr.Supatana Auetavekiat and Associate Professor Malulee Tuntawiroon for their valuable suggestion and guidance.

I wish to express the deepest appreciation to Associate Professor Sivalee Suriyapee, Head of Medical Physics at Division of Radiation Oncology, Department of Radiology, Faculty of Medicine, Chulalongkorn University, and Professor Franco Milano, University of Florence, Italy for their valuable suggestion to this study.

I would like to greatly thank medical physicists, nuclear medicine physicians and staffs at PET/CT center, Division of Nuclear Medicine, medical physicists and radiation oncologists at Division of Radiation Oncology, King Chulalongkorn Memorial Hospital, Thai Red Cross Society for their kind contribution and suggestion to this work. I also wish to express gratitude to all lecturers and staff in Biomedical Engineering Program, Chulalongkorn University, for their unlimited teaching throughout whole study.

I would like to thank the 90th Anniversary of Chulalongkorn University Fund (Ratchadaphiseksomphot Endowment Fund) for the research grant, and the Faculty of Graduate Studies for the scholarship to present part of this research in 11th AOCMP at Kyushu University.

Last but not least, my gratefulness to every member in my family for their financial supports, valuable encouragement and entirely cares during doctoral course study.

CONTENTS

Page

ABSTRACT (THAI) iv
ABSTRACT (ENGLISH) v
ACKNOWLEDGEMENTS vi
CONTENTS vii
LIST OF TABLES ix
LIST OF FIGURES x
LIST OF ABBREVIATIONS xiii
CHAPTER I INTRODUCION 1
1.1 Background and rationale 1
1.2 Research objectives 3
1.3 Expected benefits 4
1.4 Definitions 4
1.5 Significance of the study 5
1.6 Organization of dissertation 5
CHAPTER II LITERATURE REVIEWS 6
2.1 Theories 6
2.1.1 Positron emission tomography (PET) 6
Basic PET imaging 6
Iterative reconstruction 8
Partial volume effect 9
2.1.2 Thresholding 10
Otsu’s method 11
2.1.3 Active contour 12
2.1.4 Esophageal cancer 16
2.2 Related literature reviews 17
CHAPTER III RESEARCH METHODOLOGY 20
3.1 Research design model 20
3.2 Key words 21
3.3 Materials 21

Page

3.3.1 PET/CT system 21
3.3.2 Phantom sets 22
3.3.3 Fluorine-18 solution 23
3.3.4 Apparatus 24
3.4 Methods 24
3.4.1 PET tumor boundary delineation 24
Shifted-optimal thresholding method 25
Region-based active contour 27
3.4.2 Phantom study 32
Phantom preparation 32
PET data acquisition and image reconstruction 33
3.4.3 Patient study 34
3.4.4 Validation 35
3.4.5 Statistical analysis 36
3.5 Ethical consideration 36
CHAPTER IV RESULTS 37
4.1 Segmentation results of phantom study 37
Comparison with other methods 42
4.2 Segmentation results of patient study 50
CHAPTER V DISCUSSION AND CONCLUSIONS 58
5.1 Discussion 58
5.2 Conclusions 62
5.3 Recommendations 62
REFERENCES 63
APPENDICES 70
Appendix A Example of esophageal tumor traced by automated algorithm 71
Appendix B Performance measurement of PET 81
Appendix C List of publications 89
VITAE 90

LIST OF TABLES

Table **Page**

3.1 PET data acquisition and image reconstruction 34
4.1 The results of tumor volume detection at SBR 4 and 8 38
4.2 The results of tumor volume detection at SBR 12 and 16 38
4.3 The results of mutual overlapping part based on shifted-optimal thresholding embedded into a region-based active contour 41
4.4 The results of tumor volume detection based on ACWE method 42
4.5 The results of tumor volume detection based on Otsu's method 42
4.6 The results of mutual overlapping part based on Otsu's method 46
4.7 The results of mutual overlapping part based on ACWE method 47
4.8 Statistics description of *MOP* for Otsu, ACWE and our method 47
4.9 The characteristics of 10 esophageal cancer patients underwent ^{18}F-FDG whole-body PET/CT imaging 51
4.10 The results of tumor delineation in 10 esophageal cancer patients 51
4.11 The difference of diameter equivalent of esophageal tumor between manual and automatic methods 53

LIST OF FIGURES

Figure **Page**

1.1 Tumor contouring of esophagus in CT image 1
1.2 Axial contrast enhancement CT image and fused PET/CT image obtained at the same level..... 2
2.1 True coincidence detection, scatter, and random coincidence detection in PET imaging..... 6
2.2 PET sinogram 7
2.3 The conceptual step of iterative reconstruction method 8
2.4 Schematic presentation of partial volume effect 9
2.5 Example of recovery coefficient for sphere diameter function 10
2.6 Iteration steps of active contour (snake) energy minimization 12
2.7 Description of the parametric active contour 13
2.8 Topology change using level set..... 14
2.9 a U shape image, edge map, saddle point and stationary point..... 15
2.10 Staging of esophageal cancer 17
3.1 Research frameworks..... 20
3.2 Combined PET/CT system at King Chulalongkorn Memorial Hospital 21
3.3 Phantom sets..... 23
3.4 Fluorine-18 productions..... 23
3.5 Chemical structure of ^{18}F-fluorodeoxyglucose 24
3.6 Cross-sectional slice of ^{18}F-FDG thoracic imaging with esophageal tumor in a red box..... 25
3.7 Optimal thresholding according to shifted-optimal thresholding method and overlapping part corresponds to the gray level..... 26
3.8 Pixel value corresponding to the blurred area between tumor background in PET image 27
3.9 The scheme of the average intensity inside (c_1) and outside (c_2) contour in the input image $I(x,y)$ according to ACWE method..... 28
3.10 Level set function $\phi(x, y)$ of the contour 30

Figure **Page**

3.11 Setup for IEC/2001 body phantom for PET acquisition 33
3.12 *MOP*: segmented region and ground truth region 36
4.1 PET image of the IEC/2001 phantom showing the six spheres simulate the tumor for delineation and CT image of IEC/2001 phantom 37
4.2 Correlation between the true volume and detected volume 39
4.3 Volume detection errors (%) at various sphere diameters and SBRs..... 39
4.4 Tumor volume mismatch (cc) at various sphere diameters and SBRs 40
4.5 Bland-Altman plot between the ground truth and automatic methods 40
4.6 *MOP* results by our method at various SBRs and sphere diameters 41
4.7 Comparison of segmentation results between the ground-truth Otsu, ACWE and our automatic method at SBR 4 43
4.8 Comparison of segmentation results between the ground-truth Otsu, ACWE and our automatic method at SBR 8 44
4.9 Comparison of segmentation results between the ground-truth Otsu, ACWE and our automatic method at SBR 12 44
4.10 Comparison of segmentation results between the ground-truth Otsu, ACWE and our automatic method at SBR 16 45
4.11 Comparison of average volume detection error for all SBR at various sphere diameters 45
4.12 Comparison of average volume detection error for all sphere diameters at various SBRs 46
4.13 *MOP* for Otsu's method, ACWE and our method at SBR 4 48
4.14 *MOP* for Otsu's method, ACWE and our method at SBR 8 48
4.15 *MOP* for Otsu's method, ACWE and our method at SBR 12 49
4.16 *MOP* for Otsu's method, ACWE and our method at SBR 16 49
4.17 The efficiency of active contour 50
4.18 The statistical relation between radiation oncologist manual tracing and automatic method for 10 esophageal cancer patients 52
4.19 Bland-Altman plot between the manual and automatic method (n=10) 52
4.20 The esophageal tumor of whole-body PET image 54

Figure **Page**

4.21 The efficiency of the active contour in esophageal tumor with small structure. 55
4.22 The segmentation results based on threshold method..... 55
4.23 Comparison of esophageal tumor tracing with round shape 56
4.24 Comparison of esophageal tumor tracing with irregular shape..... 57
5.1 Otsu threshold with significantly different variances of two clusters 59

LIST OF ABBREVIATIONS

µCi	microcurie
AAPM	American Association of Physicists in Medicine
AC	adenocarcinoma
ACM	active contour model
ACWE	active contour without edges
AEC	automatic exposure control
CT	computed tomography
cm	centimeter
cc	cubic-centimeter
DE_{vol}	volume detection error
DICOM	digital imaging and communications in medicine
ESF	edge stopping function
^{18}F-FDG	fluorine-18 fluoro-2-deoxy-D-glucose
FBP	filtered-back projection
FOV	field of view
FWHM	full width at half maximum
GAC	geometric active contour
GTV	gross tumor volume
IAEA	International Atomic Energy Agency
IEC	International Electrotechnical Commission
IRB	institutional review board
ITM	iterative threshold method
kBq	kilobecquerel
keV	kiloelectronvolt
kg	kilogram
LOR	line of response
LSM	level set method
LSO	lutetium oxyorthosilicate
mA	milliampere
MBq	megabecquerel

mCi	millicurie
mL	milliliter
mm	millimeter
MOP	mutual overlapping part
NEMA	National Electrical Manufacturers Association
ns	nanosecond
PAC	parametric active contour
PACS	picture archiving and communication systems
PET	positron emission tomography
PSF	point spread function
PVE	partial volume effect
OSEM	ordered subsets expectation maximization
RC	recovery coefficient
RTL	relative threshold level
SBR	source-to-background ratio
SCC	squamous-cell carcinoma
SD	standard deviation
SDF	signed distance function
SNR	signal-to-noise ratio
SUV	standardized uptake value
TAC	traditional active contour

CHAPTER I

INTRODUCTION

1.1 Background and rationale

Positron emission tomography (PET) is a powerful molecular imaging modality provides the functional information corresponding to the location and concentration of the radiotracer in the target organs (Boellaard, 2009). The tomographic imaging is based on the detection of the dual 511 keV annihilation photons in same coincidences which is originated from positron-emitting radiotracer. The level of glucose metabolism of the cancer cell is much higher than the normal cell. Therefore, the PET image is very useful for revealing the primary tumor site detection in oncology patients. Due to the widespread in clinical use of PET imaging and the clearer anatomical detail is required, the PET/CT scanner was developed to improve the localization of a certain disease (Townsend, 2008). As this hybrid system provides the combination of functional and anatomical features simultaneously, the ^{18}F-fluoro-2-deoxy-D-glucose (FDG) PET/CT imaging has raised the need to define the contour of the gross tumor volume (GTV) in radiation oncology for diagnosis purposes (Brambilla *et al*., 2008).

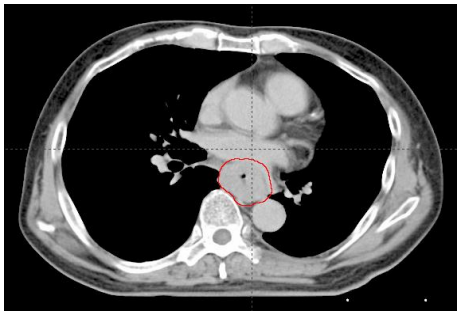

Figure 1.1 Tumor contouring of esophagus in CT image.

Among several types of cancer, esophageal carcinoma is one of cancer which is being incorporated PET image in order to delineate the tumor in treatment planning process (Macmanus and Leoung, 2007). Esophageal carcinoma ranks the ten most common malignancies in the world especially elderly people who live in developing

countries (Wieder *et al*., 2008). In Thailand, this cancer shows significantly higher evidence in the South than other regions due to tobacco smoking and alcohol drinking. Chemo/radio therapy and palliative resection are the available approaches for esophageal cancer treatment depending on the tumor stage. Traditionally, the gross tumor volume of esophageal cancer is usually identified and delineated in CT image (figure 1.1). However, due to the low contrast of soft tissue, it is difficult to distinguish between tumor and its surrounding tissue. In contrast, as illustrated in figure 1.2, ^{18}F- FDG-PET image has high sensitivity than CT image for revealing the tumor of esophagus (Bruzzi *et al*., 2007; Macmanus and Leoung, 2007). According to the advantage from functional imaging such as PET, the accuracy and consistency of the tumor boundary delineation is of great concerned to the implementation of the treatment planning process. The significance of the process is not only to optimize the coverage treated volume of esophageal tumor, but also to reduce the complications to the surrounding normal structure, e.g. heart, trachea and lungs. Moreover, the efficiency of the planning process could be improved and increased survival rate of the patient.

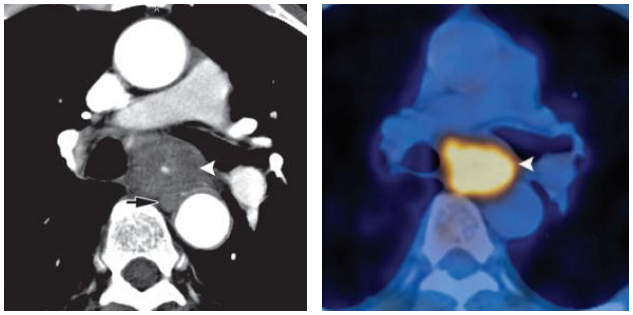

Figure 1.2 Axial contrast enhancement CT image (left) and fused PET/CT image obtained at the same level (right). (Bruzzi *et al*., 2007)

However, the tumor delineation on PET images is not a simple task due to the limited spatial resolution, indistinct boundary of the tumor, presence of noise, and the partial volume effect (Li *et al.*, 2008; van Dalen *et al.*, 2007). Since PET tumor contouring is mostly dependent on the experience of the radiation oncologists, it is subject to significant intra-observer and inter-observer variabilities (Cheebsumon *et al.*, 2011; Day *et al.*, 2009; Jentzen *et al.*, 2007). In order to trace the tumors in PET

image more accurately and precisely, a computer-assisted algorithm is used. Several automatic or semi-automatic techniques such as thresholding-based method (Brambilla *et al.*, 2008; Daisne *et al.*, 2003; Drever *et al.*, 2007; Jentzen *et al.*, 2007; van Dalen *et al.*, 2007), region growing method (Day *et al.*, 2009), and gradient-based method (Geets *et al.*, 2007) are implemented for medical image segmentation. However, this issue is still needed further study to improve the accuracy and consistency of PET tumor contouring.

Among many proposed techniques for image segmentation, a deformable model called active contour (Chan and Vese, 2001; Kass *et al.*, 1988) is one of the most successful method. The active contour has now been extensively implemented for image segmentation because it is very effective in segmenting an object according to key image features (Phumeechanya *et al.*, 2010; Zhang *et al.*, 2010). In the past, only a few studies have implemented this model to segment ^{18}F-FDG PET tumor image (Li *et al.*, 2008). Moreover, most of the previous studies show segmented results with large errors. According to these reasons, this dissertation is aimed to develop an automatic and operator-independent in tracing the boundary of esophageal tumor in PET images. The algorithm is based on a region-based active contour model, an advanced segmentation technique. Moreover, the shifted-optimal thresholding has been embedded within the external force of active contour. The efficiency of the proposed method is first tested in several spherical lesions of the anthropomorphic phantom. In clinically implementation, the tumor delineation results by both automatic and manual methods have also been compared and evaluated with histological proven esophageal carcinoma patients who underwent a whole-body PET/CT imaging at King Chulalongkorn Memorial Hospital.

1.2 Research objectives

1.2.1 To develop an automatic algorithm to trace PET tumor boundary in esophageal cancer patients.

1.2.2 To evaluate the efficiency of active contour segmentation at various sphere volume (tumor size) and source-to-background ratio (SBR) in phantom.

1.3 Expected benefits

1.3.1 Obtain an automatic computer program for delineating PET tumor boundary in esophageal cancer.

1.3.2 Reduce the erroneous of tumor boundary delineation in PET image.

1.3.3 Improve the accuracy and consistency for PET tumor delineation in esophageal cancer.

1.3.4 Accelerate the treatment planning process in esophageal cancer patient with high accuracy.

1.4 Definitions

Active contour: an energy minimizing spline in order to evolve a contour under the some constraints to extract the desired object. According to the nature of constraint, the energy function of active contour which is minimized is a weighted combination between internal force and external force (Chan and Vese, 2001; Zhang *et al*., 2010).

Fluorodeoxyglucose (FDG): the main compound clinically used for PET or PET/CT imaging. Normally, it is labeled with ^{18}F and behaves similar to the glucose metabolism tracer and trapped within the cells during metabolism. The resulting distribution provides a functional image related to the location of glucose uptake in active tumors (Abouzied *et al*., 2005; Boellaard, 2009; Yu, 2006).

Full width at half maximum (FWHM): a parameter commonly used to describe the spatial and energy resolutions of an imaging system. The value is measured by the full width of the profile at a point that is half the maximum value of the curve of function (Daube-Witherspoon *et al*., 2002; NEMA, 2007).

Partial volume effect: the phenomenon which is occurred when the object only partially occupies the sensitive volume of an imaging instrument or it is smaller than twice the detector's resolution. Then it will appear to spread out with the measured counts (signal) less than the true counts. The effect also contains the

spillover effect due to contamination of activity from the neighboring tissue to the hot or cold area (Soret *et al.*, 2007).

Prompt counts: coincident events acquired in the standard coincident time window of a positron emission tomography. Prompt counts include true, scattered, and random coincidences (IAEA human health series no.1, 2009).

Standardized uptake value (SUV): the most widely used method to measure the quantification of ^{18}F-FDG studies. The SUV indicates the ^{18}F-FDG uptake within the tissues or tumor to distinguish between benign and malignant tissue. The value is obtained by measured the activity concentration over the region of interest (ROI) and normalized to the injected dose per patient's body weight (Boellaard, 2009).

1.5 Significance of the study

1.5.1 The automatic algorithm to trace PET tumor boundary which is novel, simple and robust was developed.

1.5.2 Independent of sphere volume and the SBR threshold-volume curves calibration.

1.5.3 Independent of operator's skill.

1.5.4 Not specific for particular PET scanner.

1.6 Organization of dissertation

The outline of this dissertation consists of five chapters. Chapter I explains statement of the problem and the objectives of this dissertation. Chapter II provides the basic physics of PET imaging, fundamental of image segmentation by active contour method, and literature reviews for tumor delineation on PET images from previously researchers. Chapter III, describes the materials and methods including a region-based active contour and shifted-optimal threshold (combined algorithm) that is performed with both *in-vitro* and *in-vivo* studies. Chapter IV, the experimental results of an automatic tumor tracing method, and the comparison of the results with other publication techniques are presented. Chapter V, discussion and conclusions of the dissertation are finally drawn.

CHAPTER II

LITERATURE REVIEWS

2.1 Theories

2.1.1 Positron emission tomography (PET)

Basic PET imaging

PET, a powerful nuclear medicine imaging, is based on the detection in coincidence at nearly 180° opposing directions of the two 511 keV gamma photon. These photons are produced by the annihilation reaction which is originated from positron (β^+) emitting source combined with an electron in the matter. Usually, the positron has been obtained from certain injected radiopharmaceuticals within the patient. The two photons are then detected by the detectors within coincidence time window and along the straight line connecting the center between two opposing detectors, called the line of response (LOR). By acquiring a large number of LORs, it is used to reconstruct the distribution of the radioactive nuclei inside the patient to determine the metabolic activity of living cells (IAEA human health series no.1, 2009).

$$\beta^+ + e^- \xrightarrow{annihilation} photon\,(511\,keV) + photon\,(511\,keV)$$

In order to detect the two gammas emitted from positron event, two opposing detectors are used and a valid event is also recorded. As illustrated in figure 2.1, there are three types of coincident events that are usually detected in PET system.

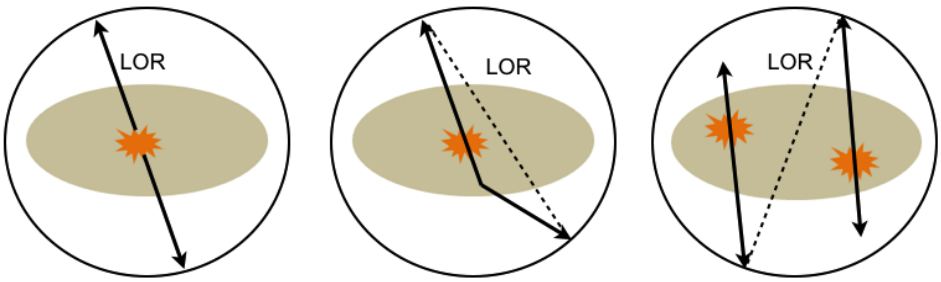

Figure 2.1 True coincidence detection (left), scatter (middle), and random coincidence detection (right) in PET imaging.

□ *True coincidence*: occurs when both photons from same annihilation event are detected by detectors within the coincidence time window.

□ *Random coincidence*: occurs when both participating photons arising from different positron annihilation and are detected within coincidence time window.

□ *Scattered coincidence*: occurs when at least one participating photon from same annihilation is scattered before coincidence detection.

In order to acquire the coincidence events, three steps are followed. Firstly, the location of the opposing detectors is determined for each coincidence event. Secondly, the pulse height of the detected photon is checked if it is within the energy window set for 511 keV. Finally, the position of LOR is determined in terms of polar coordinates to store the event. Unlike the conventional planar imaging where individual events are stored in as (*x*,*y*) matrix, the coincident events in PET system are stored in the form of a *sinogram* (Saha, 2005; Lewellen, 2008).

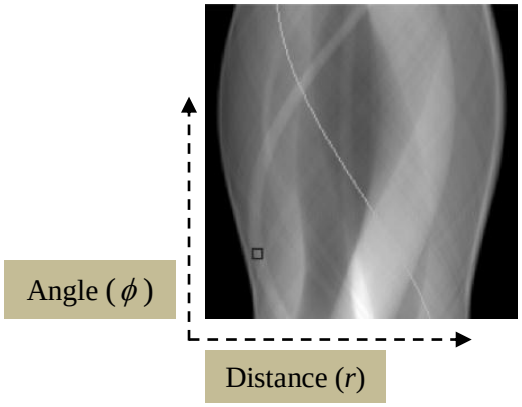

Figure 2.2 PET sinogram.

Many coincident events arise from different locations along the LOR and all are detected by the same pair detector and stored in the same pixel. For the data storage in sinogram, each LOR is defined by the distance (*r*) from the center of the scan field and the angle of orientation (ϕ) of the LOR. If the distance against the angle in (r, ϕ) coordinates are plotted, the shaded area of sinogram will be obtained as shown in figure 2.2 (Fahey, 2002).

In the final sinogram, the total counts in each pixel representing the number of coincident events detected along LOR by two opposing detectors during the counting time will be shown.

Iterative reconstruction

Iterative algorithm is widely used for reconstructing 2D and 3D PET images. An initial estimate of the image is first made. The projection are then computed from the image and compared with the measured projections. If there is a difference between the estimated and measured projections, the corrections are performed to improve the estimated image. A new iteration is created to assess the convergence between the estimated and measured projections. The process is continued until a reasonable agreement between the two sets of projection is achieved (Saha, 2005). To gain more insight, the basic concept of iterative reconstruction technique is shown as in figure 2.3.

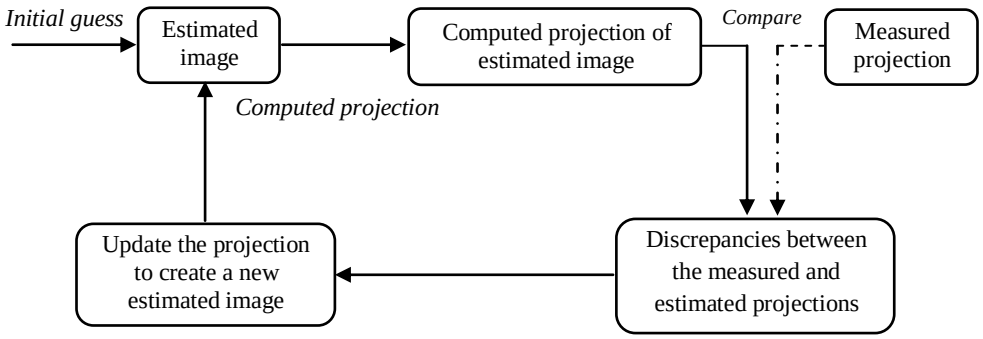

Figure 2.3 The conceptual step of iterative reconstruction method.

Unfolding of the estimated image into a set of projections is considered as the forward projections, as opposed to the back-projection (Saha, 2005). This projection is accomplished by determining the weighted sum of the radioactivity in all pixels along LOR across the estimated image. Hence, a projection q_i from an estimated image can be given by:

$$q_i = \sum_{j=1}^{N} a_{ij} C_j \tag{2.1}$$

where C_j is the counts (activity) in the j^{th} pixel, a_{ij} is the probability that an emission from pixel j is recorded in the i^{th} LOR.

The most widely used iterative algorithm in PET is an *ordered-subset expectation maximization* (OSEM) algorithm. The projections from this model are

grouped into subsets around the object to be imaged and separated by some fixed angle. The computation time decreases with the increasing number of subsets. Based on the iterative image reconstruction method, it can be improved insensitivity to noise and capability to reconstruct an optimal image from incomplete data (Saha, 2005).

Partial volume effect (PVE)

The quantitative data analysis of PET image is usually measured in terms of activity concentration (Bq/cc) in region of interest (Boellaard, 2009). The *partial volume effect* refers to both under/overestimation of activities around small structures in the reconstruction PET image. This phenomenon is usually occurred due to the relatively low image resolution of the PET system and the limited image sampling (Soret *et al*., 2007). A schematic presentation of PVE for 3 conditions of radioactivity distribution is illustrated as in figure 2.4.

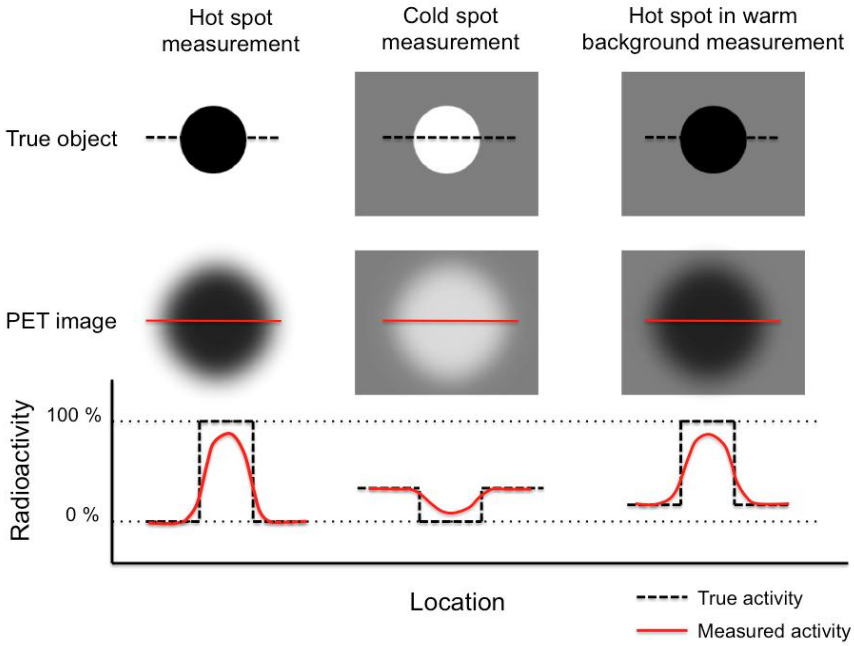

Figure 2.4 Schematic presentation of partial volume effect (Verel *et al*., 2005).

A structure that is smaller than twice of the scanner's resolution will be shown partial loss of intensity (activity). In case of the hot spot lesion relative to a cold background, the structure will appear to be smeared over the larger area than its occupies in the reconstruction image. The activity concentration is also lower than it actually has. In contrast, a cold lesion relative to a hot background would appear

smaller with high activity concentration. These can be reduced the contrast between high and low uptake regions. The effect also contains the *spillover effect* due to the contamination of activity from the neighboring tissue to these hot or cold areas.

Recovery coefficient (RC)

RC is a conversion factor that usually applied for correcting the over/underestimation of activities from partial volume effect in a small structure. This coefficient can be determined by measuring the activity concentration within different object sizes. The RC value is the ratio between the reconstructed count activity and true count activity of region of interest and should be 1 for larger object. The example of the RC curve is illustrated as in figure 2.5 (Soret *et al.*, 2007).

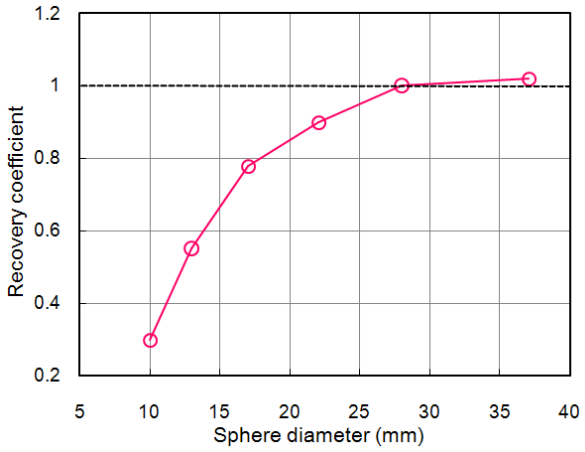

Figure 2.5 Example of recovery coefficient for sphere diameter function.

2.1.2 Thresholding

The simplest property that pixels in a region can be shared is the intensity. The thresholding is the natural way through such method to separate dark and light regions. The computational of the method is inexpensive, fast and still widely used in simple applications (Sonka *et al.*, 2008).

Thresholding will create a binary image from gray level by turning all pixels below desired threshold to zero and pixels about that threshold to one. The method is transformed the input image (f) to an output binary image (g) as follows:

$$g(x,y) = \begin{cases} 1 & \text{if } f(x,y) \geq T \\ 0 & \text{if } f(x,y) < T \end{cases} \qquad (2.2)$$

where T is the threshold, $g(x,y) = 1$ for pixels element of the object, and $g(x,y) = 0$ for pixels element of the background.

Normally, if the gray level between object and background are clearly distinct, this method can be used as a suitable segmentation method (Sonka *et al*., 2008). However, the thresholding considers only the intensity, not any relationships between the neighboring pixels. Uneven illumination and the shadow for the whole image can be influenced the segmentation of desired region: losing too much of the object and getting too many background pixels. To accomplish more suitable threshold, the approach based on histogram analysis of the image, Otsu' method, was proposed in order to find the appropriate threshold to classify the object and background areas.

Otsu's method

The threshold according to Otsu's method (Otsu, 1979) is utilized the cluster-based that derived automatically from the histogram of a given image. The gray-level histogram of the image is approximated using a weighted sum of two probability density functions assuming normal distributions. The method is iteratively calculated in order to find the threshold level that minimizes the probability of segmentation error (minimizing their overlap) between the background and the foreground regions. The gray level maximizing the inter-class variance (or minimizing the intra-class) of the two pixel groups is finally chosen. The weighted sum of variance of two clusters of pixels can be defined as in equation (2.3):

$$\sigma^2_{Between} = \omega_1\omega_2(\mu_1 - \mu_2)^2 \tag{2.3}$$

where ω_1 and ω_2 are the number of pixels of two clusters separated by Otsu's threshold (T_{Otsu}), μ_1 and μ_2 are the average intensities of these two pixel groups.

On the other hand, the optimal threshold calculated by maximizing sum of inter-class variances is the average of the mean level of two clusters (Xu *et al.*, 2011). The overall process of Otsu's threshold method can be summarized as follows:

□ separate the pixels into two clusters according to the threshold.

□ find the mean value of each cluster.

□ square the difference between the means.

□ multiply by the number of pixels in each cluster in order to find maximize between-class variance.

2.1.3 Active contour

The active contour model (ACM) or "*snake*" is a powerful method for image segmentation and visual tracking. This model was first introduced by Kass *et al.* (Kass *et al.*, 1988). The active contour is defined as an energy-minimization spline. Their energy depends on its shape and location within the image (Sonka, 2008). The basic idea of active contour is to iteratively evolve an initial curve toward the boundary of target object under influences of two forces: *internal and external forces* in order to detect the desired object. The external force is the main part of model that derived from image data (image dependent) to push the contour toward the desired boundary of the object within the image domain; whereas, the internal force keeps the contour to be smooth at all time (Chan and Vese, 2001). Unlike other segmentation methods, the contour is *active*, always minimizing its energy functional as seen in figure 2.6.

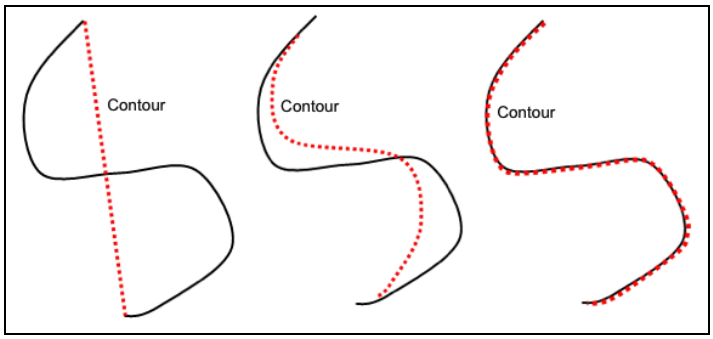

Figure 2.6 Iteration steps of active contour (snake) energy minimization.

Typically, the energy function (E) of the active contour is defined (in 2-dimensional) as in equation (2.4) (Kass *et al.*, 1988; Boscolo, 2002):

$$E_{snake} = \int_0^1 E_{\text{internal}}(C)ds + \int_0^1 E_{\text{external}}(C)ds \qquad (2.4)$$

where $E_{internal}$ is the internal energy and $E_{external}$ is the external energy.

The optimal contour is the one that minimizes energy function for a specific image and specific parameter selection (Sonka *et al.*, 2008). The internal energy ($E_{internal}$) obtaining from the contour itself for smoothing the contour can be written as in equation (2.5):

$$E_{\text{internal}} = \frac{1}{2}\left(\alpha \left| \frac{\partial C}{\partial s} \right|^2 + \beta \left| \frac{\partial^2 C}{\partial s^2} \right|^2 \right) \tag{2.5}$$

where α and β are the parameters to control the elasticity (stretching) and rigidity (resistance to bending) of the contour (Sonka et al., 2008).

There are two categories to represent deformable active contour model: *parametric active contour (PAC) and geometric active contour (GAC)*. For the parametric model, the contour $C(s)$ is represented analytically in the parametric form as $C(s) = [x(s), y(s)],\ s \in [0,1]$ whose shape is controlled by the parameters, where x and y are the coordinate function along the contour, and s is the arc length of the contour. To gain more insight, the description of parametric active contour is illustrated as in figure 2.7.

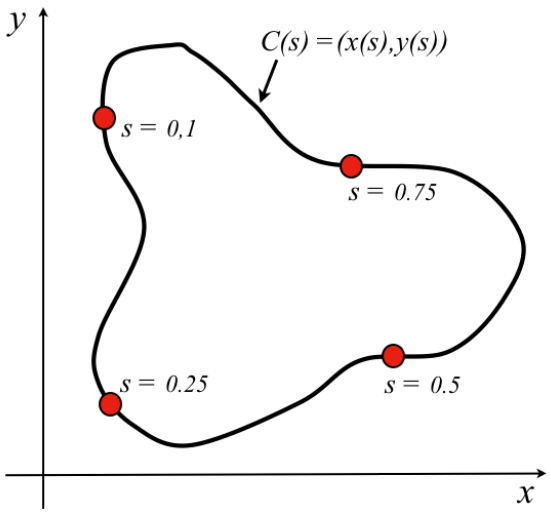

Figure 2.7 Description of the parametric active contour.

While the geometric model, the curve is evolved using only geometric computations, independent of any parameterization: the active contour is embedded implicitly as the zero level set $C = \{(x, y) \in \Omega : \phi(x, y) = 0\}$ of signed distance

function $\phi(x, y)$, where Ω is the image spatial domain. Therefore, the contour can automatically handle any topological change during the deformation. Based on the geometric model, the contour can be split and combined together (Osher and Sethian, 1988). The level set concept of curve embedding and topology change are illustrated as in figure 2.8. As the level set function is updated for t = 1, 2, 3, the zero level set changes topology, eventually providing a 2-object boundary.

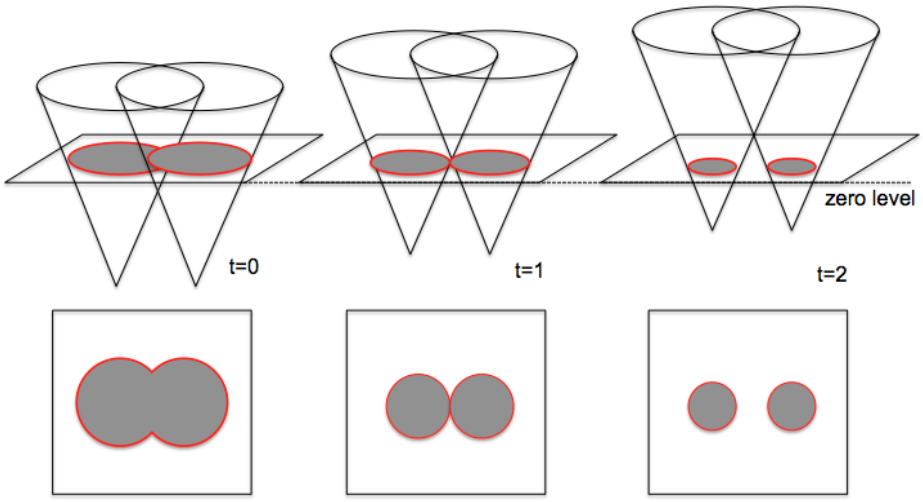

Figure 2.8 Topology change using level set.

Usually, the external force of the active contour model can be classified into two types: edge-based model and region-based model. For edge-based external force, this model utilizing the gradient vector of the image to construct edge map to stop the evolving curve on the boundary of the object. One of the most popular edge-based models is the geodesic active contour model (Caselles *et al*., 1997). The edge stopping function (ESF) $g(|\nabla I|)$ according to geodesic active contour can be defined as follows:

$$g(|\nabla I|) = \frac{1}{1+|\nabla(G_\sigma * I)|^2} \tag{2.6}$$

where ∇ and * are the gradient and convolution operators, G_σ is the 2-dimensional Gaussian kernel, I is the input gray-scale image. The terms $\nabla(G_\sigma * I)$ denotes gradient of a Gaussian-smoothed image, where σ is a standard deviation (smoothing parameter).

Nevertheless, the edge-based active contour is usually suffered from saddle point and stationary point problems. The saddle point occurs when the contour is tangent to the force vector, while the stationary point occurs when all of vectors are pointing outward in all directions to the nearest edge points (Phumeechanya *et al.*, 2010). These critical points are commonly found in the image with a small opening at the concave part resulting in obstruct the contour during evolve into concavity region (figure 2.9). The edge-based active contour may fail to segment the object when the initial contour is far from the desired boundary. Furthermore, the leakage problem and converges to the wrong segmentation will be occurred if the target boundary is not well clarify (Zhang *et al.*, 2008).

Figure 2.9 (a) a U shape image (b) edge map (c) saddle point (rectangle) and stationary point (circle). (Phumeechanya *et al*., 2010)

Later on, the region-based active contour model is proposed to overcome the limitation of the edge-based model especially the leakage problem. The external force of the model utilizes statistically calculated of the average intensity inside and outside the contours to control the evolution. The model is less sensitive to noise and has better performance for image segmentation with weak edges or without edges (Chan and Vese, 2001; Zhang *et al*., 2010). Based on the entirely regional information, the segmentation result is significantly robust to the initial curve placement. Moreover, the contour can be detected both interior and exterior boundaries of the object simultaneously.

According to these advantages, C-V model (Chan and Vese, 2001) is the outstanding region-based method to overcome the inherent problems of edge-based stopping criteria. The model is based on techniques of curve evolution, Mumford-

Shah functional for segmentation (Mumford and Shah, 1989) and implemented via the level set method (Osher and Sethian, 1988). The detail of the C-V model will be described later in chapter 3.

2.1.4 Esophageal cancer

Esophageal cancer is a malignancy of the esophagus. This cancer is the third most common malignancy of the digestive tract leading cause of cancer mortality (Hatt *et al.*, 2012) Approximately 90-95 percent of all esophageal cancers worldwide, squamous-cell carcinoma (SCC) and adenocarcinoma (AC) are commonly found. SCC arises from the squamous epithelium cells occurring in the upper and middle parts of the esophagus, whereas AC begins from glandular (secretory) cells that occur at the esophagogastric junction, the distal part of the esophagus (Enzinger and Mayer, 2003). Tobacco smoking and substantial alcohol drinking are the greatest risk factors for squamous-cell carcinoma, whereas gastroesophageal reflux and obesity are the major factors for adenocarcinoma. Esophageal tumors lead to painful, difficulty swallowing (dysphagia), weight loss and other symptoms that could be diagnosed with biopsy.

Barium swallowing is usually used to detect esophageal cancer with dysphagia, while CT is complementary considered to find out stage and follow-up the cancer. Currently, PET imaging is being used to identify esophageal cancer especially the primary tumor. Even though the spatial resolution is limited, it has advantage of total body coverage that can show the metastatic distant sites. Several approaches including surgery, radiation and chemotherapy are available to treat esophageal cancer patients depending on the tumor stage (Lyer *et al.*, 2003).

The staging of the esophageal cancer can be classified in accordance with the American Joint Committee on Cancer (AJCC) system based on the tumor, node and metastasis (TNM) classification (Bruzzi *et al.*, 2007). The two most important prognostic indicators for esophageal cancer are the advanced tumor depth (T stage) and/or nodal involvement (N stage), while the presence or absence of distant metastases is additionally described in terms of M stage. As illustrated in figure 2.10, T1 lesion is involved mucosa (m) or submucosa (s), T2 lesion invades muscularis

propria (mp), T3 lesion invades adventitia (a) and T4 lesion is involved nearby organ (A-aorta).

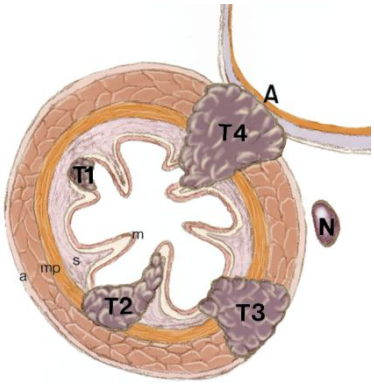

Figure 2.10 Staging of esophageal cancer (Lyer *et al*., 2003).

2.2 Related literature reviews

Manual contouring is the majority method for delineating PET tumor. After the tumor is visualized, the contouring has been performed slice-by-slice. Several factors such as the physically limited spatial resolution itself, windowing, contrast between lesion and background, and spillover artifact from PVE are usually occurred (IAEA, 2008). Based on these reasons, different operator, the visual definition of the tumor can be very subjective that depends on their experiences. This can be affected the accurate and consistent delineation of PET target tumor. To reduce the variability for metabolic tumor boundary definition in ^{18}F-FDG PET imaging, several methods based on an automatic or semi-automatic approach have been proposed.

Originally, when the simple manual thresholding was used to trace a PET tumor volume, the method is not appropriate due to lack of standardized value of window level setting. For more accurate results, the method based on the FDG standardized uptake value (SUV) was suggested. For instance, the SUV cutoff for appropriate threshold level of 2.5 was used in accordance with this approach (Zhong *et al*., 2009). This method is mostly performed in clinically practice to distinguish the difference between the tumor and normal tissue.

A fixed threshold level in the range of 40-50 % of the maximum standardized uptake value (SUV_{max}) within a tumor had also been reported in literature (Erdi *et al*., 2002). Nevertheless, the methods may lead to error in volumetric measurements and

may be inaccurate for particular lesions. Based on the thresholding technique, Daisne *et al*. (Daisne *et al*., 2003) proposed the optimal thresholding method utilizing the relationship of source-to-background ratio (SBR) for PET tumor volume. The best threshold was selected when the least square error from the ground truth and calculated volume was obtained. However, the method cannot be directly implemented with other situation due to the parameter for fitting function must be reprocessed. Another limitation is that the method may be inaccurately segmented for tumor with complex shape.

Brambilla *et al.* (Brambilla *et al.*, 2008) adopted the optimal percentage threshold to define FDG tumor boundary based on target-to-background (*T/B*) ratios and target size that derived from the IEC phantom (NEMA, 2007). Both variables were critically affected the variance of the threshold. Moreover, the method has not yet been implemented with the patient in clinical situation.

As the limitation of one threshold level, Jentzen *et al*. (Jentzen *et al.*, 2007) introduced the iterative threshold method (ITM) with various SBR to estimate the tumor volumes in PET imaging. Similarity, an iterative technique to determine local threshold level based on slice specific contrast was also proposed by Drever *et al.* (Drever *et al*., 2007). However, the accuracy of the tumor volume obtained from both methods depends on the proper characteristics of the tumor-to-background calibration threshold curves (initial SBR), stopping criteria and reconstruction method that are derived for a specific PET scanner. As the tumor size of each method was established based on anthropomorphic phantom, this related information is difficult to provide in actual situation. Additionally, the quantified measurement of the FDG average activity concentration is strongly dependent on the size and the type of region of interest (Boellaard, 2009).

The relative threshold level (RTL), an iterative method that is independent of the SBR was then proposed by van Dalen *et al.* (van Dalen *et al*., 2007). Their method provides accurate volume down to the spatial resolution of PET imaging. However, to predict the RTL, the measurement of the full width at half maximum (FWHM) from point spread function (PSF) is prior required in order to convolute the overlapping between the phantom sphere diameter and the PSF. As the dependency to the sphere diameter is expected, the accuracy of the PET tumor volume from iterative procedure

is affected especially on the small diameters resulting in a large change in the RTL method.

Later on, Geets *et al*. (Geets *et al*., 2007) developed the gradient-based watershed method. Even though this method provides the higher accuracy of PET tumor volume than threshold-based, the gradient-based method is much more complex procedure than the threshold-based method. The PET image must be performed via the de-noising, de-blurring, gradient estimator and watershed transform. The PSF was also considered for an isotropic Gaussian kernel in a de-blurring process.

PET tumor segmentation with anal and rectal cancer by using confidence connected region growing (CCRG) was then proposed by Day *et al*. (Day et al., 2009). The method is iterative scheme that based on the statistics for a tumor region. Difference of seed pixel chosen could be affected the variability of tumor volume by this method. Recently, Li *et al*. (Li *et al*., 2008) published a two-stage method based on dual-front active contour and adaptive region growing to segment PET image. Even though the method was validated in IEC torso phantom with different SBRs, only one head and neck cancer patient was implemented in clinical study.

Since the limitation of these methods as mentioned previously, this dissertation is aimed to develop an automatic method to improve the accurate and consistent PET tumor boundary tracing based on the combination between a region-based active contour and optimal thresholding method.

CHAPTER III

RESEARCH METHODOLOGY

3.1 Research design model

This dissertation has been designed as an experimental study to determine the boundary of a tumor in PET image. According to the research framework as in figure 3.1, the scope of the research was set as the following steps:

□ Calibrate the PET/CT system in accordance with NEMA NU2-2007.

□ Develop an automatic algorithm to trace tumor boundary in PET images.

□ Verify the designed algorithm with the ground truth on IEC/2001 body phantom

□ Implement the proposed algorithm in ^{18}F-PET/CT imaging of esophageal cancer.

□ Evaluate the efficiency of automatic method and compare to manual method performed by experienced radiation oncologist.

□ Compare the delineation results to other published studies.

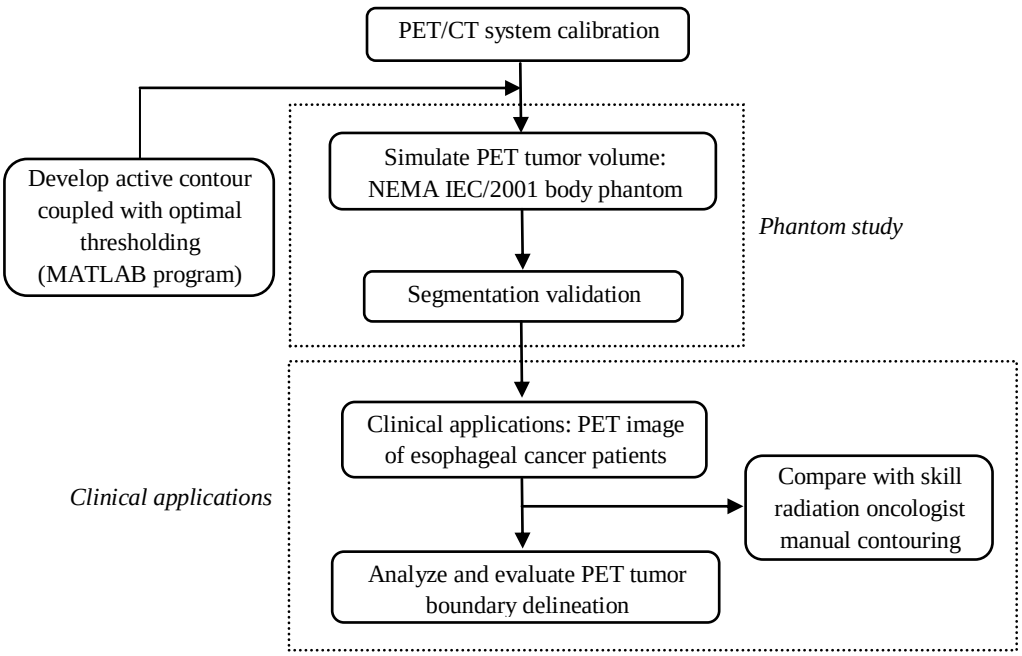

Figure 3.1 Research frameworks.

3.2 Key words

□ Automatic tumor delineation

□ ^{18}F-FDG

□ Positron emission tomography

□ Active contour

□ Optimal thresholding

3.3 Materials

3.3.1 PET/CT system

Figure 3.2 Combined PET/CT system at King Chulalongkorn Memorial Hospital.

The PET/CT system model Biograph 16 HI-REZ manufactured by Siemens Medical Solutions as shown in figure 3.2 was used to acquire the PET/CT tomographic imaging. This system was installed at PET/CT center, Division of Nuclear Medicine, King Chulalongkorn Memorial Hospital, Bangkok in August 2008. The scanner consists of 24,336 cerium-doped lutetium oxyorthosilicate (LSO) PET detector (circular full-ring system) with axial field of view (FOV) of 16.2 cm, and combined with 16-slices multi-detector CT. The LSO detector elements are subdivided in an array of 13 x 13 crystals with the dimension of each crystal of 4 x 4 x 20 mm (Li *et al*., 2007, Townsend, 2008). The operating console has been worked by using the *syngo* multimodality computer platform to fuse both PET and CT images

together (Erdi *et al*., 2004). For CT part, three tube voltage settings are available at 80, 120 and 140 kVp. Tube-current can be varied between 28 and 500 mA. In order to optimize the patient radiation dose, an automatic tube-current (mA) modulation or automatic exposure control (AEC) technique can be performed via CARE Dose4D acquisition protocol.

3.3.2 Phantom sets

The NEMA IEC/2001 anthropomorphic torso phantom with the hollow sphere inserts as illustrated in figure 3.3(a) is the phantom use for simulating the patient with tumors. This phantom is also used to evaluate the reconstructed image quality of whole-body PET imaging (Daube-Witherspoon *et al*., 2002; NEMA, 2007). It is designed in accordance with the recommendations by the International Electrotechnical Commission (IEC) and modified by the National Electrical Manufacturers Association (NEMA) (Jentzen *et al*., 2007). The cylindrical phantom with dimension of 24.1 x 30.5 x 24.1 cm (height x width x depth) consists of six hollow sphere inserts with inner diameters of 1.0, 1.3, 1.7, 2.2, 2.8 and 3.7 cm, and the wall thickness of 1 mm. The volume of the D shape torso phantom is 9,700 cc and the six spheres are 0.52, 1.15, 2.57, 5.58, 11.50 and 26.63 cc, respectively. A cylinder (5.0 ± 0.2 cm diameter) filled with low atomic number material was inserted at the center of body compartment representing lung attenuation (average density of 0.3 ± 0.1 g/cc). The other phantom made of plastic cylinder of 70 cm length, with density of 0.96 ± 0.01 g/cc as scatter phantom is shown in figure 3.3(b). It was used together to mimic an out-of-field radioactivity. This cylinder phantom was drilled from end to end by a hole parallel to the axis (radial offset of 45 ± 1 mm) to contain the plastic tube filling with radioactivity.

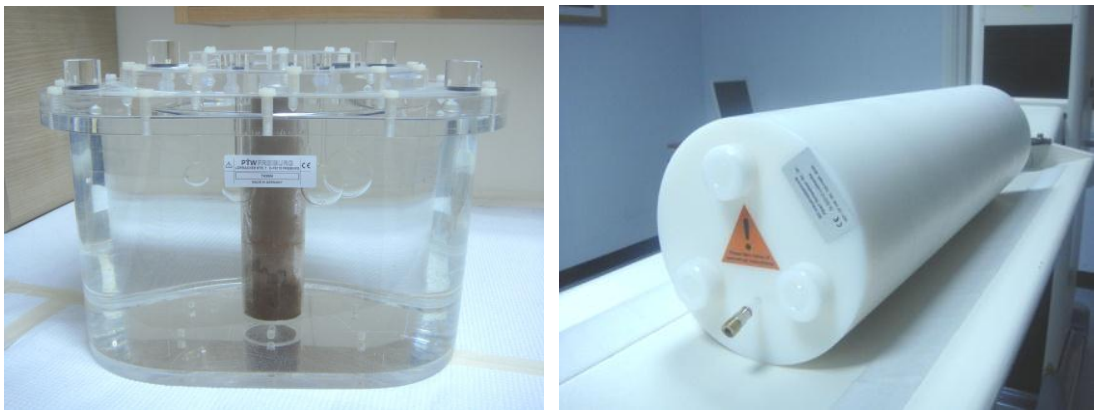

(a) (b)

Figure 3.3 Phantom sets (a) NEMA IEC/2001 anthropomorphic phantom with six hollow inserts and (b) scatter phantom with a plastic tube insert.

3.3.3 Fluorine-18 solution

The fluorine-18 (^{18}F) has usually been produced by the medical cyclotron. After the oxygen-18 (^{18}O)-enriched water has been bombarded by the proton, the ^{18}F is occurred (having a half-life of 109.77 minutes). A schematic illustration of the nuclear reaction using protons to produce ^{18}F isotope is shown as in figure 3.4.

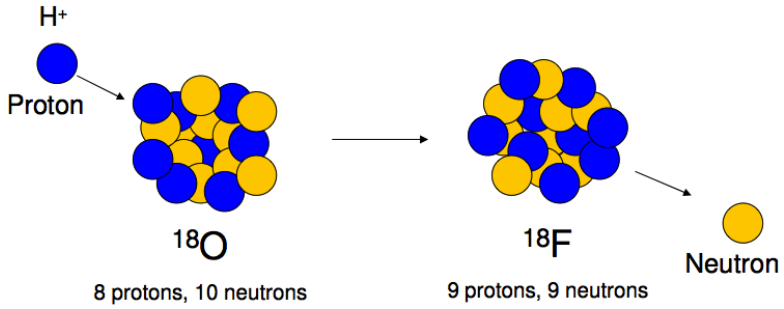

Figure 3.4 Fluorine-18 productions.

Fluorine-18 labeled with *2-deoxy-2-fluoro-D-glucose* (FDG) compound becomes ^{18}F-FDG, a glucose metabolism tracer, in order to differentiate between the malignant and normal tissue in oncology (Boellaard, 2009). As illustrated in figure 3.5, ^{18}F-FDG chemical structure, a glucose analog, is replaced for the normal hydroxyl group at the 2' position in the glucose molecule (Yu, 2006). For the mechanism, FDG-PET imaging in cancer is based on the property of increased

glucose uptake into malignant cell and undergoes glycolysis process within them. Then FDG is converted to FDG-6-phosphate and will be trapped within the intracellular. Therefore, its uptake depends on the proportional of glycolysis rate in the tissue (IAEA human health series no.1, 2009).

Usually, tumor cells use large amounts of glucose as an energy source due to its higher glucose metabolism compared to normal tissue (Abouzied *et al*., 2005). Hence, the metabolic tumor imaging in the patient's body has also been presented by the detection of two 511 keV photons that released from positron combined with electron and detected by the PET system.

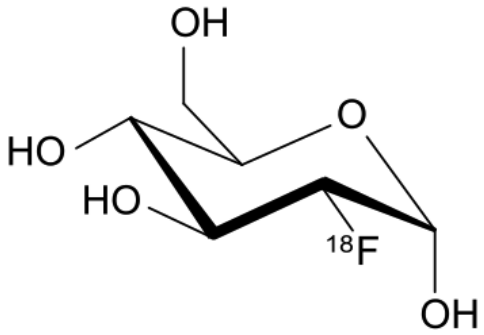

Figure 3.5 Chemical structure of ^{18}F-fluorodeoxyglucose (Yu, 2006)

3.3.4 Apparatus

3.3.4.1 MATLAB program

3.3.4.2 Laptop computer

- 2.3 GHz Intel dual-core i5 processor with a 4 GB RAM.

3.4 Methods

3.4.1 PET tumor boundary delineation

In order to trace the boundary of a tumor in PET image, an automatic algorithm based on the shifted-optimal thresholding coupled with region-based active contour is designed. The proposed algorithm is created via level set using MATLAB program on a 2.3 GHz Intel dual-core i5 processor with a 4 GB RAM.

3.4.1.1 Shifted-optimal thresholding method

The esophageal tumor in PET image is usually brighter than its surrounding tissue as a "hot lesion" as shown in figure 3.6. When the image is implemented with the Otsu's method (Otsu, 1979), the threshold is deviated from the intersection point to the background region with the variance larger than the tumor (Xu *et al.*, 2011). As the Otsu's threshold is lower than the correct tumor threshold in PET image in practical, the shifted-optimal thresholding method ($T_{Shifted}$) in this study is designed in order to obtain more suitable threshold level.

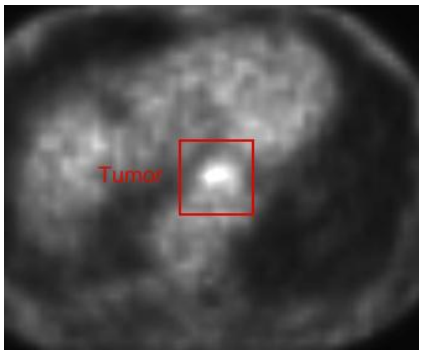

Figure 3.6 Cross-sectional slice of ^{18}F-FDG thoracic imaging with esophageal tumor in a red box.

The threshold according to the cluster-based Otsu's method is first derived automatically from the histogram of a given image. The method is iteratively calculated in order to find the threshold level that maximizes the inter-class variance of two pixel clusters. Once the optimal threshold in accordance with Otsu's scheme is obtained, the local minimum (lowest number of pixel) of the part of the histogram of only those pixels between the Otsu's threshold (T_{Otsu}) and the pixel with maximum intensity gray level, i.e., $T_{shifted} \in [T_{Otsu}, 255]$ should be found and used as the shifted-optimal threshold ($T_{shifted}$). The gray level in accordance with this scheme is finally chosen and embedded into a region-based active contour in order to achieve the smoother results of PET tumor delineation which is being described in the next part.

In addition, this threshold value corresponds to the highest overlapping part between the segmented area and ground truth area (figure 3.7). The pixel value at adjacent region between the tumor and the background in blurred edge area is also illustrated in figure 3.8.

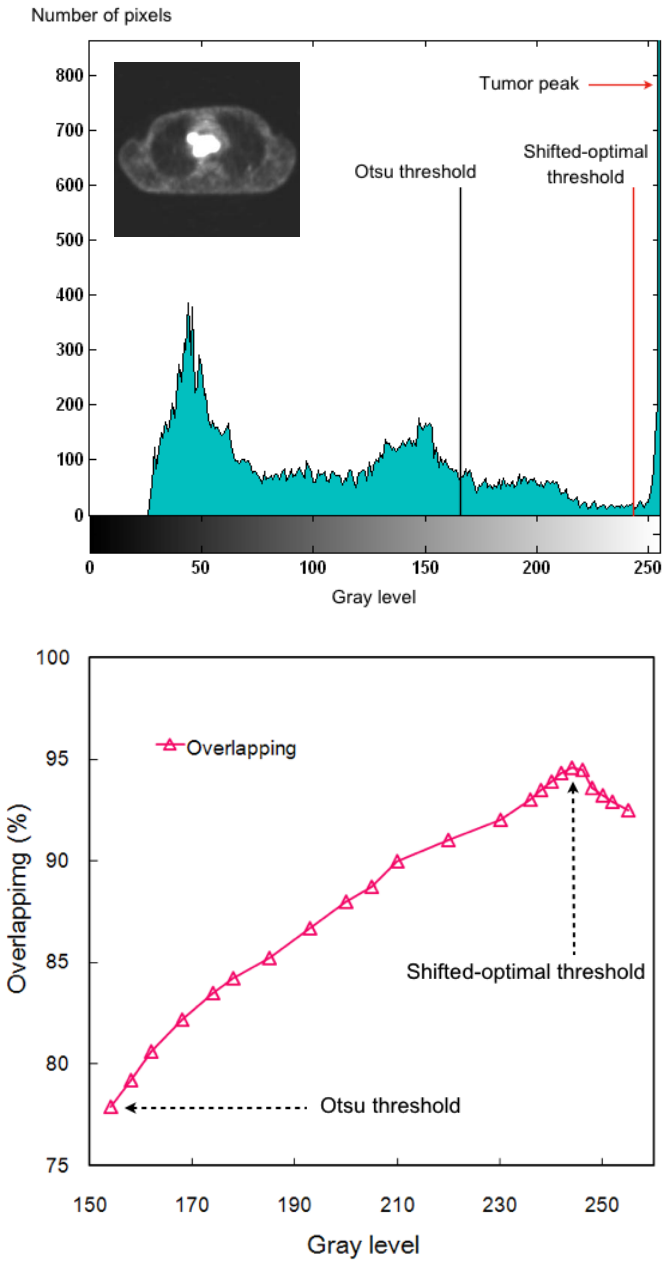

Figure 3.7 Optimal thresholding according to shifted-optimal thresholding method (upper) and overlapping part corresponds to the gray level (lower).

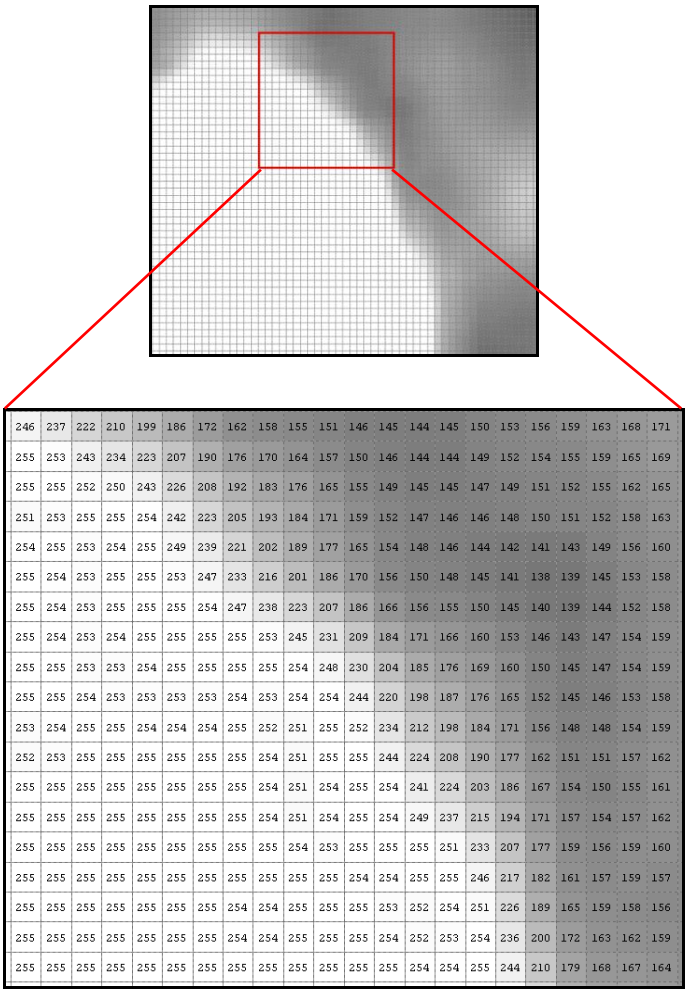

246	237	222	210	199	186	172	162	158	155	151	146	145	144	145	150	153	156	159	163	168	171
255	253	243	234	223	207	190	176	170	164	157	150	146	144	144	149	152	154	155	159	165	169
255	255	252	250	243	226	208	192	183	176	165	155	149	145	145	147	149	151	152	155	162	165
251	253	255	255	254	242	223	205	193	184	171	159	152	147	146	146	148	150	151	152	158	163
254	255	253	254	255	249	239	221	202	189	177	165	154	148	146	144	142	141	143	149	156	160
255	254	253	255	255	253	247	233	216	201	186	170	156	150	148	145	141	138	139	145	153	158
255	254	253	255	255	255	254	247	238	223	207	186	166	156	155	150	145	140	139	144	152	158
255	254	253	254	255	255	255	255	253	245	231	209	184	171	166	160	153	146	143	147	154	159
255	255	253	253	254	255	255	255	255	254	248	230	204	185	176	169	160	150	145	147	154	159
255	255	254	253	253	253	253	254	253	254	254	244	220	198	187	176	165	152	145	146	153	158
253	254	255	255	254	254	254	255	252	251	255	252	234	212	198	184	171	156	148	148	154	159
252	253	255	255	255	255	255	255	254	251	255	255	244	224	208	190	177	162	151	151	157	162
255	255	255	255	255	255	255	255	254	251	254	255	254	241	224	203	186	167	154	150	155	161
255	255	255	255	255	255	255	255	254	251	254	255	254	249	237	215	194	171	157	154	157	162
255	255	255	255	255	255	255	255	255	254	253	255	255	255	251	233	207	177	159	156	159	160
255	255	255	255	255	255	255	255	255	255	255	254	254	255	255	246	217	182	161	157	159	157
255	255	255	255	255	255	255	254	254	255	255	255	253	252	254	251	226	189	165	159	158	156
255	255	255	255	255	255	255	254	254	255	255	255	254	252	253	254	236	200	172	163	162	159
255	255	255	255	255	255	255	255	255	255	255	255	255	254	254	255	244	210	179	168	167	164

Figure 3.8 Pixel value corresponding to the blurred area between tumor and background in PET image.

3.4.1.2 Region-based active contour

The active contour is the main part of the algorithm to delineate the PET tumor. Normally, the external force based on the edge-based information may encounter the leakage problem of the contour and converges to the wrong segmentation if the target boundary is not well defined (Zhang *et al.*, 2008). As the indistinct boundary and the presence of noise play as the major problems in PET image, the region-based active contour has been chosen to overcome this situation.

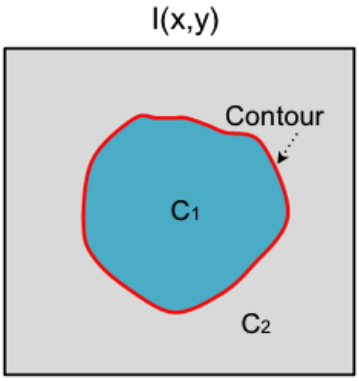

Figure 3.9 The scheme of the average intensity inside (c_1) and outside (c_2) contour in the input image *I(x,y)* according to ACWE method.

The "active contour without edges" (ACWE) or C-V model (Chan and Vese, 2001) designs its external force based on the global regional information of the image. The model can effectively extract an object with indistinct edges from a noisy background in a given image. In its design, the scheme calculates statistical information of the average intensity values of the whole pixel areas inside the contour and compares it to that residing entirely outside the contours (figure 3.9). The region of interest will be separated from background when an objective energy function is optimized according to the energy function (E) as in equation (3.1):

$$\begin{aligned} E(\phi) = \mu \int_{\Omega} \delta_{\varepsilon} |\nabla(\phi)| \, dxdy + \nu \int_{\Omega} H_{\varepsilon}(\phi) dxdy \\ + \lambda_1 \int_{inside(C)} H_{\varepsilon}(\phi)(I - c_1)^2 \, dxdy \\ + \lambda_2 \int_{outside(C)} (1 - H_{\varepsilon}(\phi))(I - c_2)^2 \, dxdy \end{aligned} \tag{3.1}$$

where λ_1 and λ_2 are positive weighting parameters according to ACWE scheme, μ and ν are the weighting parameters to control the curve length and area inside the active contour, respectively. I is the input gray scale image, Ω is the image spatial domain, ∇ is the gradient operator, c_1 and c_2 are the average intensity values of all the pixels inside and outside contours, respectively. By minimizing (3.1), c_1 and c_2 can be defined as in equation (3.2) and equation (3.3):

$$c_1 = \frac{\int_{\Omega} I \cdot H_{\varepsilon}(\phi) dxdy}{\int_{\Omega} H_{\varepsilon}(\phi) dxdy} \tag{3.2}$$

$$c_2 = \frac{\int_{\Omega} I \cdot (1 - H_{\varepsilon}(\phi)) dxdy}{\int_{\Omega} (1 - H_{\varepsilon}(\phi)) dxdy} \tag{3.3}$$

The regularized Heaviside function $H_{\varepsilon}(\phi)$ representing the pixels inside the contour can be defined as in equation (3.4) (Chan and Vese, 2001):

$$H_{\varepsilon}(z) = \frac{1}{2}\left[1 + \frac{2}{\pi}\arctan\left(\frac{z}{\varepsilon}\right)\right] \tag{3.4}$$

The smooth Delta function $\delta_{\varepsilon}(\phi)$ is the derivative of the smooth Heaviside function representing the pixels on (and in the neighborhood of) the contour and can be written as in equation (3.5) (Chan and Vese, 2001):

$$\delta_{\varepsilon}(\phi) = \frac{1}{\pi}\left(\frac{\varepsilon}{\varepsilon^2 + z^2}\right) \tag{3.5}$$

As shown in figure 3.10, a region-based active contour is embedded as the zero level set (Osher and Sethian, 1988) of signed distance function (SDF), $\phi(x, y)$, such that

$$C = \{(x, y) \in \Omega : \phi(x, y) = 0\} \tag{3.6}$$

where Ω is the spatial domain of an image as mentioned previously. The region inside the contour is defined to be positive ($\phi(x, y) > 0$) and region outside the contour is defined to be negative ($\phi(x, y) < 0$). The level set method (LSM) is a numerical technique for tracking interfaces and shapes. The advantage of the level set function is to maintain the propagation and stability of the active contour. This made it easy to handle any topological change during the deformation. Therefore, the contour that implemented via level set function can split and merge together (Osher and Sethian, 1988).

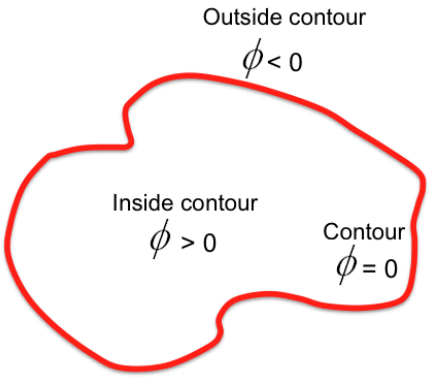

Figure 3.10 Level set function $\phi(x, y)$ of the contour.

In order to integrate the gray value obtained from shifted-optimal thresholding method into this region-based active contour, the weighting values (Chen *et al.*, 2010) for average intensity of pixels inside and outside contours are incorporated as written in equation (3.7) and equation (3.8):

$$w_{in} = \frac{(I - T_{shifted})}{(I_{\max} - I_{\min})} \tag{3.7}$$

$$w_{out} = 1 - w_{in} \tag{3.8}$$

where w_{in} and w_{out} are the weights for the pixels inside and outside the contours, I is the pixel intensity of the input image that is on the contour, I_{max} is the maximum intensity value of image, I_{min} is the minimum intensity value of image, and $T_{shifted}$ is the gray value according to shifted-optimal thresholding method. The weights as calculated in (3.7) and (3.8) are then embedded into the external energy function of the active contour; as a result, we have total energy as in equation (3.9):

$$\begin{aligned} E_{total}(\phi) = \mu \int_{\Omega} \delta_{\varepsilon} |\nabla(\phi)| \, dxdy + \nu \int_{\Omega} H_{\varepsilon}(\phi) dxdy \\ + \lambda_1 \int_{inside(C)} w_{in} H_{\varepsilon}(\phi)(I - c_{in})^2 \, dxdy \\ + \lambda_2 \int_{outside(C)} w_{out}(1 - H_{\varepsilon}(\phi))(I - c_{out})^2 \, dxdy \end{aligned} \tag{3.9}$$

where c_{in} and c_{out} are the average pixel intensity for the external force inside and outside the contours then embedded with weight values, which can be obtained using

equation (3.10) and equation (3.11) as follows:

$$c_{in} = \frac{\int_{\Omega} w_{in} \cdot I \cdot H_{\varepsilon}(\phi) dxdy}{\int_{\Omega} w_{in} \cdot H_{\varepsilon}(\phi) dxdy} \tag{3.10}$$

$$c_{out} = \frac{\int_{\Omega} w_{out} \cdot I \cdot (1 - H_{\varepsilon}(\phi)) dxdy}{\int_{\Omega} w_{out} \cdot (1 - H_{\varepsilon}(\phi)) dxdy} \tag{3.11}$$

These weight matrices are used to emphasize the high intensity area inside the contour in PET image. As the weight values are added to external energy function of the contour, both region-based active contour and shifted-optimal thresholding methods are performed consecutively. Positive weighting parameters λ_1 and λ_2 = 1 are usually determined to balance the external force inside and outside contours. In this study, we set $\lambda_1 > \lambda_2$ approximately 15-20 times in order to increase the force inside the contour and to attract the contour deformation beyond the blurred edge into the inner part of the tumor boundary. These parameters are chosen to minimize segmentation error in all SBR and all spherical diameters.

Obtaining of region-based force

The region-based force of the combined method can be obtained by minimizing the total energy function in equation (3.9). In order to obtain the evolution equation to evolve the contour, we take the derivative of equation (3.9) with respect to ϕ and equate it to zero, then solve for ϕ in $\frac{\partial E}{\partial \phi} - \frac{d}{dx}\left(\frac{\partial E}{\partial \phi_x}\right) - \frac{d}{dy}\left(\frac{\partial E}{\partial \phi_y}\right)$ = 0. However, this equation is usually solved implicitly (Chan and Vese, 2001) by letting ϕ be a function of time *t* and substituting the zero on the right by $\frac{\partial \phi}{\partial t}$, then ϕ can be calculated iteratively until the function converges, which implies that $\frac{\partial \phi}{\partial t}$ = 0. Consequently, the level set evolution is obtained as written in equation (3.12):

$$\frac{\partial \phi}{\partial t} = \delta_{\varepsilon}(\phi)\left(\mu div\left(\frac{\nabla \phi}{|\nabla \phi|} \right) - \lambda_1 w_{in}(I - c_{in})^2 + \lambda_2 w_{out}(I - c_{out})^2 \right) \qquad (3.12)$$

To gain more insight, the overview of our algorithm is summarized as below.

Step1: Obtain the histogram of the input image and determine the gray level according to the Otsu's threshold (T_{Otsu}).

Step2: For the range between T_{Otsu} and the maximum intensity value [255] of the histogram, locate the pixel intensity with local minimum ($T_{shifted}$) and use it as the shifted-threshold.

Step3: Place an initial contour onto the image.

Step4: Calculate the weighting value (w_{in} and w_{out}) according to equation (3.7) and (3.8).

Step5: Evolve the contour front using equation (3.12) until it reach the object's boundary.

3.4.2 Phantom study

3.4.2.1 Phantom preparation

The phantom study is the first part for validating the performance of the proposed method. Six hollow spheres with inner diameter ranged from 1.0 to 3.7 cm were inserted in the NEMA IEC/2001 body cylindrical phantom (NEMA, 2007). Each sphere was filled with the ^{18}F solution to simulate the target tumors. The activity concentration of ^{18}F solution of 20.7, 41.4, 62.16 and 82.9 kBq/cc (0.56, 1.12, 1.68, 2.24 µCi/cc) were filled within the spherical tumors in order to obtain four different source-to-background ratio (SBR) of 4, 8, 12, and 16 respectively. These SBR are typically observed in esophageal tumor investigation (Bruzzi *et al.*, 2007; Hyun *et al.*, 2010; Zhong *et al.*, 2009). The torso cavity of IEC phantom (background) was filled with 5.2 kBq/cc (0.14 µCi/cc) ^{18}F solution according to the NEMA NU 2-2007 (NEMA, 2007) recommendation. The background activity concentration corresponds to a typical injected radioactivity for whole-body PET studies; representing the activity distribution in normal tissues (Erdi *et al.*, 2004).

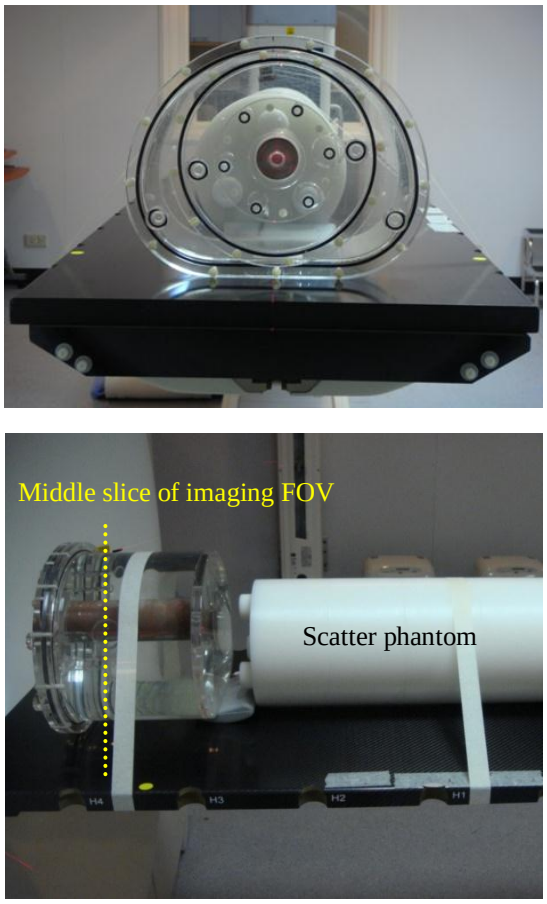

Figure 3.11 Setup for IEC/2001 body phantom for PET acquisition. Front view (upper) and lateral view (lower).

3.4.2.2 PET data acquisition and image reconstruction

The IEC/2001 body phantom was placed on the couch at the center of the field of view (FOV) together with a 70-cm-scatter phantom arranged at the end of the IEC body phantom to mimic an out-of-field radioactivity as in clinical situation (figure 3.11). Ten-minute emission scan for PET images was acquired by the Biograph 16 HI-REZ PET/CT system (CTI/Siemens Medical Solutions) with 3-dimensional (without septa) acquisition mode. The middle slice of FOV was determined at the central part of the spherical tumors of the phantom. Ordered subset expectation maximization (OSEM) algorithm with 4 iterations and 8 subsets, matrix size of 256 x 256 pixels and 4 mm slice thickness were used for image reconstruction. The convolution kernel with *x-y-z* Gaussian full width at half maximum (FWHM) of 5 mm was used as a

smoothing filter to reduce noise. Energy window from 425 to 650 keV was set for the lower and upper level discriminators with the coincidence window of 4.5 nsec. The scatter correction and the normalization were applied. The CT transmission data were then used to calculate the attenuation correction of the PET images. The summarized of the data acquisition and image reconstruction in this study is shown as in table 3.1.

Table 3.1 PET data acquisition and image reconstruction.

Description	Scanning parameters
Slice thickness	4 mm
Matrix size	256 x 256
Convolution kernel	*x-y-z* Gaussian FWHM 5 mm
Energy window	425-650 keV
Coincidence window	4.5 nsec
Scanning type	Whole-body
Reconstruction method	OSEM2D 4i8s
Scatter correction method	Model-based
Attenuation correction method	CT-derived mu-map
Random correction method	DLYD
Voxel size	2.67 x 2.67 x 4 mm
Acquisition time	10 minutes

DLYD – delayed reconstruction, nsec - nanosecond

3.4.3 Patient study

The automatic algorithm was then implemented to 10 male patients (mean age ± SD, 56.6 ± 6.8 age range 43-70 years) with histological proven of esophageal carcinoma. The whole-body ^{18}F-FDG PET/CT imaging was performed at PET/CT center, King Chulalongkorn Memorial Hospital, Bangkok, Thailand during January 2010 – July 2011. All patients had fasted for at least 6 hours and gave the written informed consent before PET/CT examination. After passing the criterion blood glucose level of 120 mg/dL, each patient was injected 5.55 MBq/kg (0.15 mCi/kg) ^{18}F-FDG and rested in the isolation room. Whole-body transmission/emission scan

was started at 45-60 min after ^{18}F-FDG administration. The CT scan was firstly acquired with tube voltage of 120 kVp, collimation of 16 x 1.5 mm, and rotating time of 0.75 sec, respectively. An automatic mA modulation technique was also used in order to reduce the radiation dose to patients. After the CT scan, the couch was moved automatically to the PET detectors and emission scanning was started. A segmented PET imaging was consecutively acquired in the caudocranial direction for 3 minutes per bed position from the upper thigh to the base of skull in the supine position (5-7 beds/patient). All images are then saved in digital imaging and communications in medicine (DICOM) format and have been sent to store in PACS system. Then the PET tumor volume in esophageal cancer obtained from our automatic tumor tracing method was compared with manual contouring by experienced radiation oncologist.

3.4.4 Validation

The segmentation results were then quantitatively analyzed in terms of volume detection error (DE_{vol}) and mutual overlapping part (MOP) to demonstrate the efficiency of an automatic method. These efficiency results were also explored the dependence of SBR and tumor sizes (sphere diameter) in IEC body phantom. The DE_{vol} is calculated as in equation (3.13):

$$DE_{vol} = \frac{(V_{\det} - V_{true})}{V_{true}} \times 100\ \% \tag{3.13}$$

where V_{det} is the detected volume, V_{true} is the true spherical volume. The ground truth is calculated based on the formula $V = (4/3)\pi r^3$ for the spherical volume by using inner diameter. Inaccuracy of detected volume due to the glass wall thickness of 1 mm of spheres may be occurred, even though there is no FDG uptake in the glass wall (Hofheinz *et al.,* 2010; van Dalen *et al.,* 2007). In order to evaluate the similarity on spatial relationship between the ground truth and segmented regions, the quantification measurement of mutual overlapping part is also calculated as in equation (3.14):

$$MOP = \frac{2 \cdot n(A_{\det} \cap A_{true})}{n(A_{\det}) + n(A_{true})} \tag{3.14}$$

where $\cap$ is the set intersection operator, $n(A_{det} \cap A_{true})$ is the number of pixels inside both A_{det} and A_{true}, $n(A_{det})$ is the number of pixels inside the segmented area, $n(A_{true})$ is the number of pixels inside the ground truth area. As seen in figure 3.12, the *MOP* is based on computing the area of overlap between the ground truth and a segmented region. The *MOP* has a value between 0 (no overlapping pixels between two areas), and 1 (two areas are completely overlapped), i.e., $MOP \in [0,1]$.

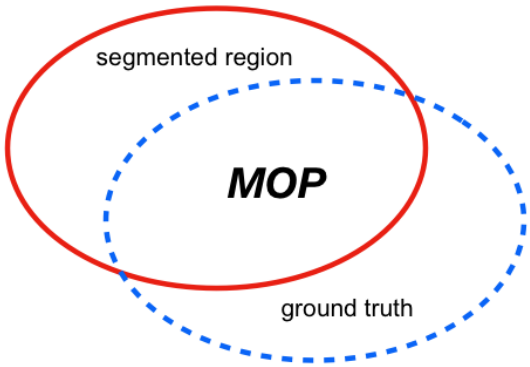

Figure 3.12 *MOP*: segmented region (solid) and ground truth region (dash).

3.4.5 Statistical analysis

A Bland-Altman analysis (Bland and Altman, 1986) was used to assess the agreement level between the two measurement methods: manual tracing method by radiation oncologist and automatic method. The agreement of tumor volume between the ground truth from spherical tumor and automatic tracing was also analyzed.

3.6 Ethical consideration

This dissertation is designed to test with both *in-vitro* and *in-vivo* studies. For the clinical implementation, even though the study is not directly tested in patients, the PET images including information of patient suffering from esophageal cancer underwent PET/CT at King Chulalongkorn Memorial Hospital were used in order to achieve the goal of tumor boundary determination. According to the ethical consideration of research in the human, the study has already been approved by the institutional review board (IRB) of Faculty of Medicine, Chulalongkorn University.

CHAPTER IV

RESULTS

4.1 Segmentation results of phantom study

In this part, the validation results of the automatic method on the IEC/2001 body phantom are first described. The representative PET image reconstruction of the body phantom is shown in figure 4.1. The results of the spherical tumor volume tracing by the proposed method were compared to the known sphere volume at SBR of 4, 8, 12 and 16 as shown in table 4.1 and table 4.2 respectively. The volume detection error (DE_{vol}) in terms of the percentage is also presented in the parentheses.

The delineation result is more accurate with higher SBR and larger spheres. The results show that the best segmentation was obtained with the largest sphere of SBR 16 with the DE_{vol} of 1.51 %, whereas the worse DE_{vol} of 36.53 % was observed with the smallest sphere at SBR 4. The lowest overall of average DE_{vol} and standard deviation (SD) in all sphere diameters was obtained at SBR 16 of 7.47 ± 4.41 %, as well as the lowest overall of average DE_{vol} and SD in all SBR was obtained with sphere diameter of 3.7 cm of 4.07 ± 2.67 %. The largest value of the overall average DE_{vol} and SD was at the smallest sphere diameter of 24.51 ± 9.73 % and at the lowest SBR of 23.10 ± 11.06 %, respectively.

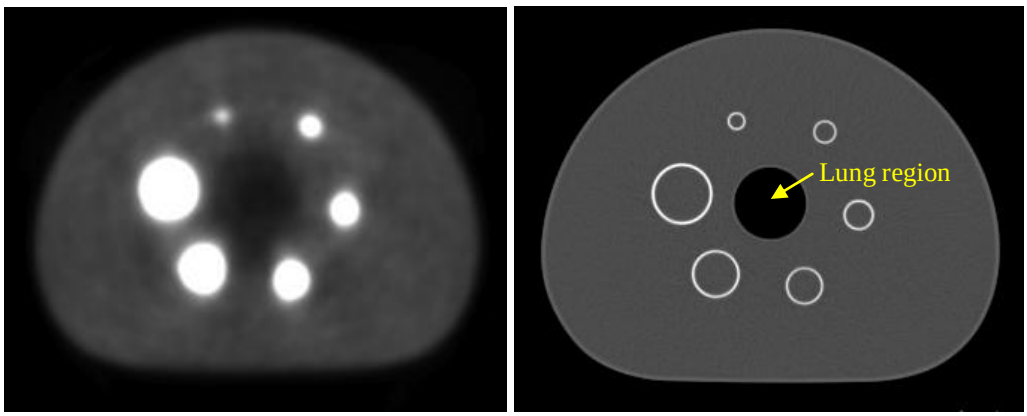

Figure 4.1 (left) PET image of the IEC/2001 phantom showing the six hot spheres simulate the tumor for delineation and (right) CT image of IEC/2001 phantom.

Table 4.1 The results of tumor volume detection at SBR 4 and 8.

Sphere diameter (cm)	True volume (cc)*	Detected volume, cc (Volume detection error, %)	
		SBR 4	SBR 8
1.0	0.52	0.71 (36.53)	0.66 (26.92)
1.3	1.15	1.53 (33.04)	1.44 (25.21)
1.7	2.57	3.23 (25.68)	3.09 (20.23)
2.2	5.58	6.80 (21.86)	6.36 (13.98)
2.8	11.50	13.10 (13.91)	12.63 (9.82)
3.7	26.53	28.55 (7.61)	27.73 (4.52)

* Calculated from spherical inner diameter, SBR – source-to-background ratio.

Table 4.2 The results of tumor volume detection at SBR 12 and 16.

Sphere diameter (cm)	True volume (cc)*	Detected volume, cc (Volume detection error, %)	
		SBR 12	SBR 16
1.0	0.52	0.63 (21.15)	0.59 (13.46)
1.3	1.15	1.35 (17.39)	1.27 (10.43)
1.7	2.57	2.88 (12.06)	2.80 (8.95)
2.2	5.58	6.09 (9.14)	5.96 (6.81)
2.8	11.50	12.26 (6.61)	11.92 (3.65)
3.7	26.53	27.23 (2.63)	26.93 (1.51)

* Calculated from spherical inner diameter, SBR – source-to-background ratio.

To gain more insight, the correlation between the true volume and detected volume is shown as in figure 4.2. The detected volume deviates from the true volume (dash line) when the SBR was decreased. Figure 4.3 illustrated the DE_{vol} at different SBR corresponds to sphere diameter. The DE_{vol} tends to decrease with increasing the sphere diameter and SBR. Inversely, when the difference of tumor volume mismatch in terms of cubic centimeter (cc) is considered, graphs tend to increase with increasing the sphere diameter in all SBRs as seen in figure 4.4.

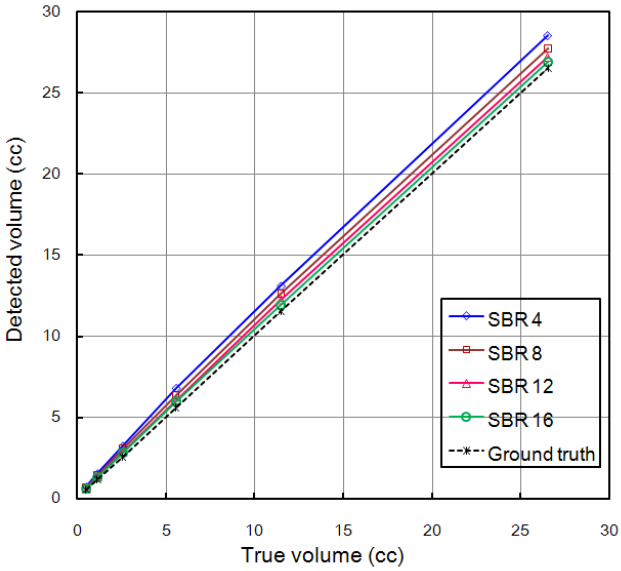

Figure 4.2 Correlation between the true volume and detected volume.

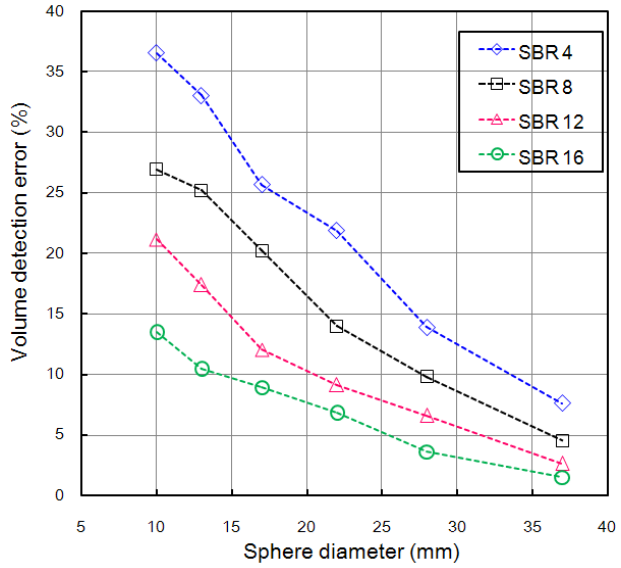

Figure 4.3 Volume detection errors (%) at various sphere diameters and SBRs.

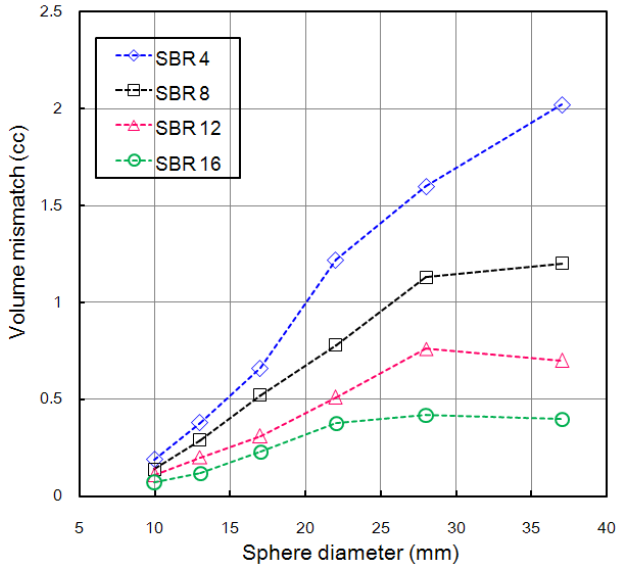

Figure 4.4 Tumor volume mismatch (cc) at various sphere diameters and SBRs.

A Bland-Altman analysis of volume mismatch between the ground truth and automatic method at various SBRs is shown as in figure 4.5. Mean deviation of 0.6 cc was seen with 95% confidence interval (CI) ranged from -0.17 to 1.36 cc. Most of the tumor volume delineation by automatic method is in agreement with the ground truth. However, out of the range of the agreement was observed with the two largest sphere diameters at SBR of 4 (the detail will be discussed in chapter 5).

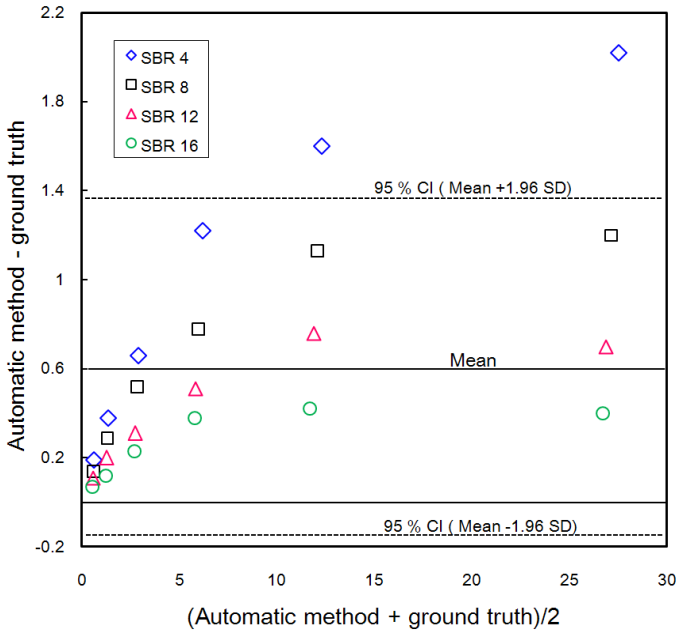

Figure 4.5 Bland-Altman plot between the ground truth and automatic methods (the data are presented in terms of cubic centimeter).

Normally, a Bland–Altman plot or difference plot refers to an effective method that widely used to assess the agreement of two measurements techniques (Ammar *et al.*, 2011). Based on the graphical method, the differences between the two techniques are plotted against the averages of the two techniques. Mean difference and the limits of the upper and lower agreement (95 % CI, mean difference ± 1.96SD) are drawn at the horizontal lines (Bland and Altman, 1986).

Table 4.3 The results of mutual overlapping part based on shifted-optimal thresholding embedded into a region-based active contour.

Sphere diameter (cm)	SBR 4	SBR 8	SBR 12	SBR 16
1.0	0.90	0.94	0.96	0.97
1.3	0.94	0.95	0.96	0.97
1.7	0.96	0.96	0.97	0.98
2.2	0.96	0.97	0.98	0.98
2.8	0.96	0.98	0.98	0.99
3.7	0.98	0.98	0.99	0.99

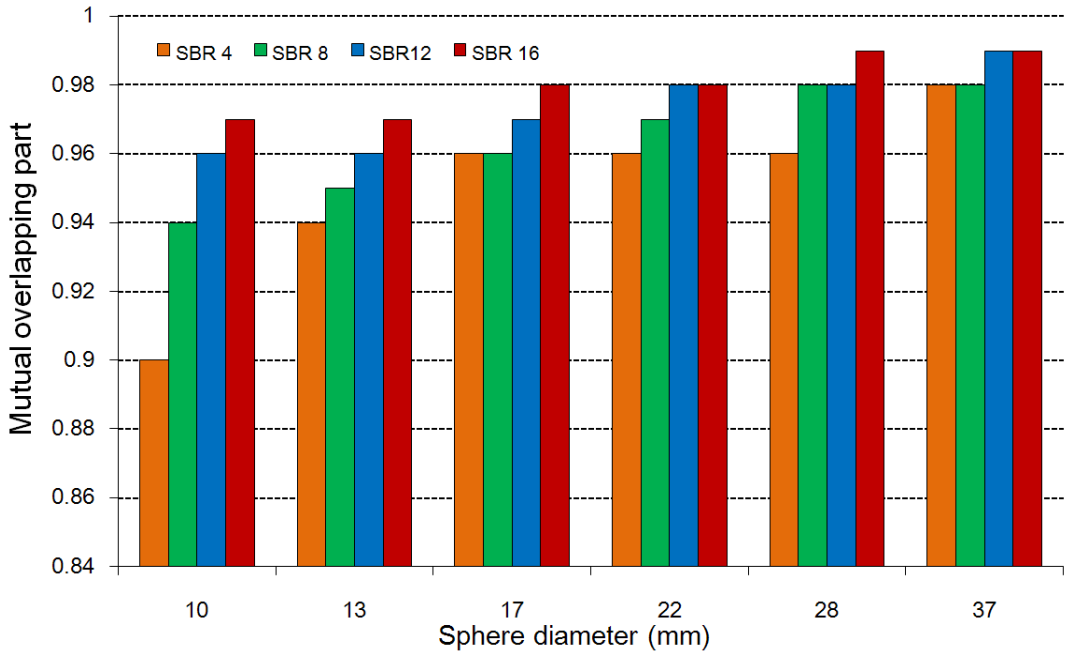

Figure 4.6 *MOP* results by our method at various SBRs and sphere diameters.

Table 4.3 shows the results for mutual overlapping part (*MOP*) by using our automatic method. The best *MOP* results of 99 % were obtained with the largest sphere at SBR 12 and 16. However, the best average and standard deviation of *MOP* was observed at SBR 16. The graphical data of *MOP* at various sphere diameter and different SBR in figure 4.6 illustrated that the *MOP* increase with increasing both of sphere diameter and SBR.

Comparison with other methods

The results of tumor volume detection by Otsu's method (Otsu, 1979) and ACWE method (Chan and Vese, 2001) are illustrated as in table 4.4 and 4.5, respectively. To gain more insight, the tumor volume delineation by our automatic method at various SBR was compared with the Otsu's method and ACWE as shown in figure 4.7-4.10. Each segmentation method were also compared the volume deviation with the ground truth at SBR of 4, 8, 12 and 16 respectively. We can see that our method provides the delineation results better than other two segmentation methods. While the SBR increased, the tumor volume deviation decreased and to near the ground truth values at SBR of 16. In addition, when compared to Otsu and ACWE in terms of the average volume detection error for all sphere diameters and all SBRs, our method is still provided the deviation lower than the other two segmentation methods. These results are illustrated as in figure 4.11 and 4.12 respectively.

Table 4.4 The results of tumor volume detection based on Otsu's method.

Sphere diameter (cm)	**True volume (cc)**	**Detected volume (cc)**			
		SBR 4	**SBR 8**	**SBR 12**	**SBR 16**
1.0	0.52	2.16	1.84	1.74	1.64
1.3	1.15	3.92	3.33	3.24	3.10
1.7	2.57	7.35	5.76	5.51	5.19
2.2	5.58	12.38	11.44	11.33	10.14
2.8	11.50	21.65	19.29	18.72	18.14
3.7	26.53	42.16	39.07	38.36	36.62

Table 4.5 The results of tumor volume detection based on ACWE method.

Sphere diameter (cm)	True volume (cc)	Detected volume (cc)			
		SBR 4	SBR 8	SBR 12	SBR 16
1.0	0.52	1.85	1.71	1.52	1.47
1.3	1.15	3.30	3.04	2.71	2.61
1.7	2.57	6.25	5.36	5.09	4.88
2.2	5.58	11.00	9.67	8.99	8.46
2.8	11.50	17.35	16.82	15.70	14.16
3.7	26.53	37.63	35.60	34.35	32.45

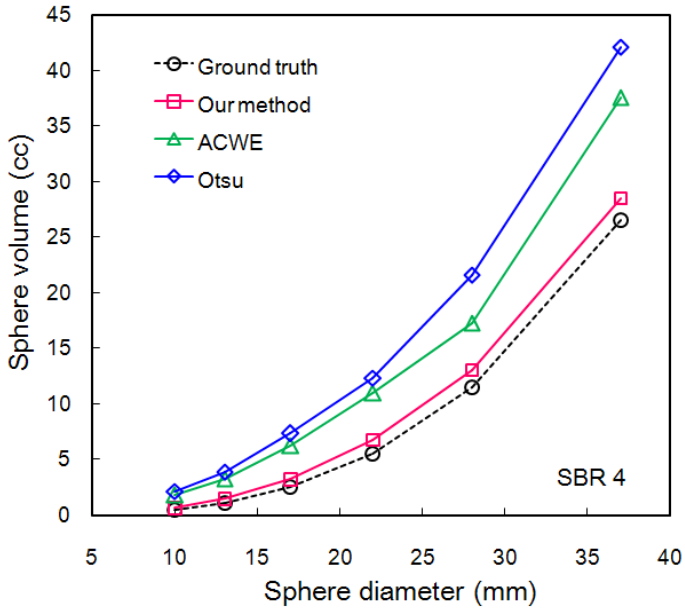

Figure 4.7 Comparison of segmentation results between the ground-truth, Otsu, ACWE and our automatic method at SBR 4.

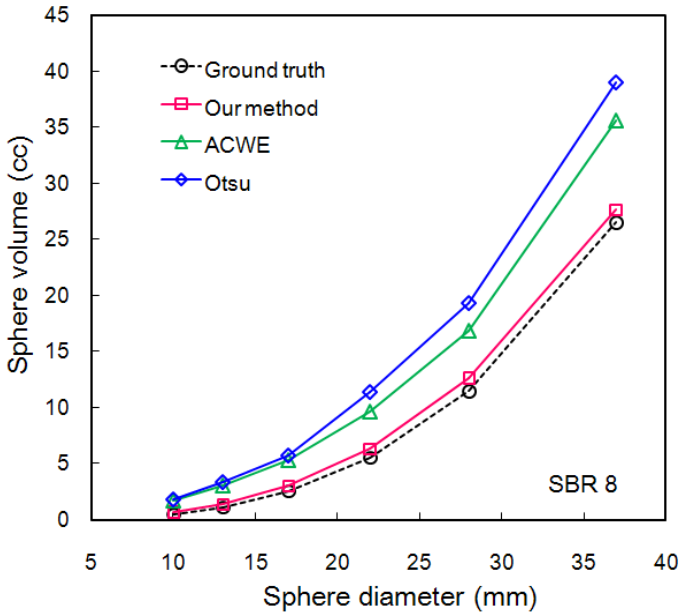

Figure 4.8 Comparison of segmentation results between the ground-truth, Otsu, ACWE and our automatic method at SBR 8.

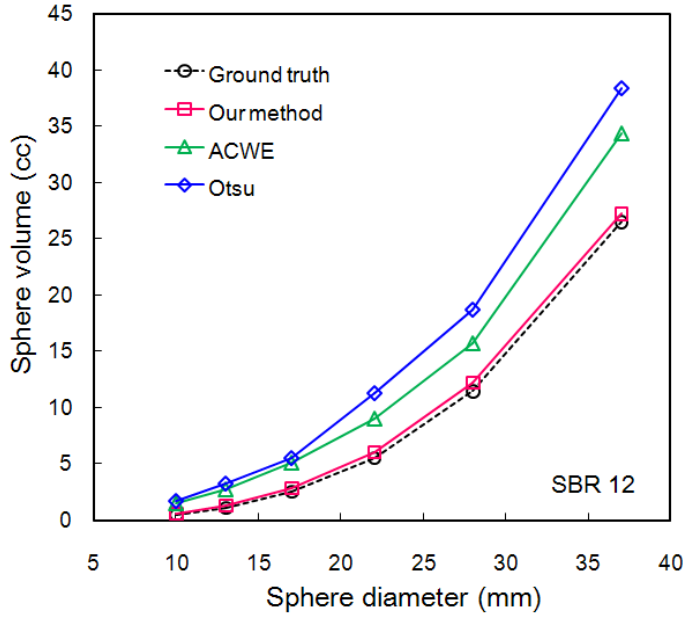

Figure 4.9 Comparison of segmentation results between the ground-truth, Otsu, ACWE and our automatic method at SBR 12.

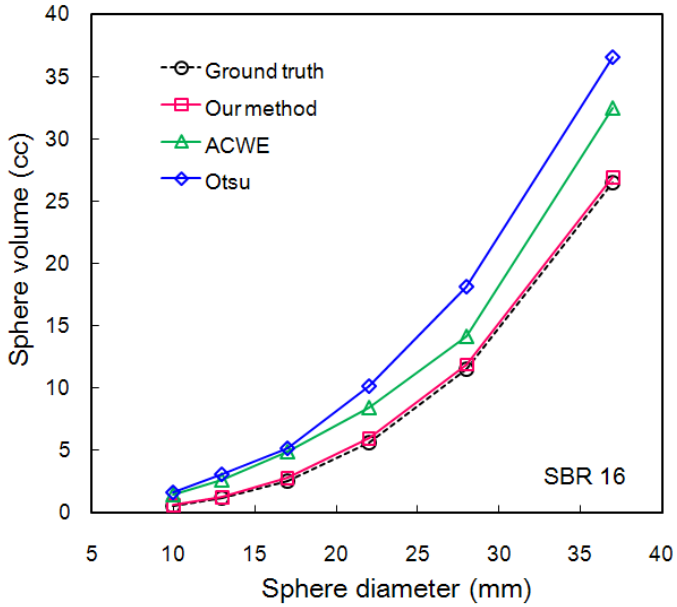

Figure 4.10 Comparison of segmentation results between the ground-truth, Otsu, ACWE and our automatic method at SBR 16.

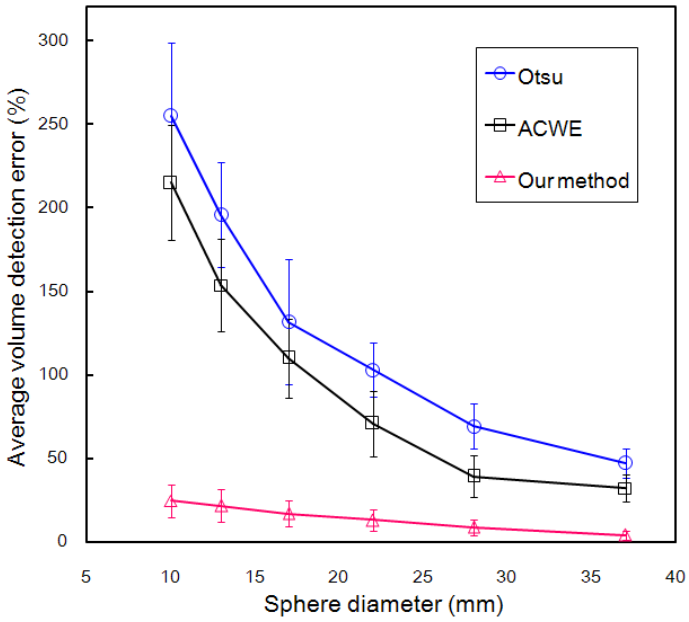

Figure 4.11 Comparison of average volume detection error for all SBR at various sphere diameters.

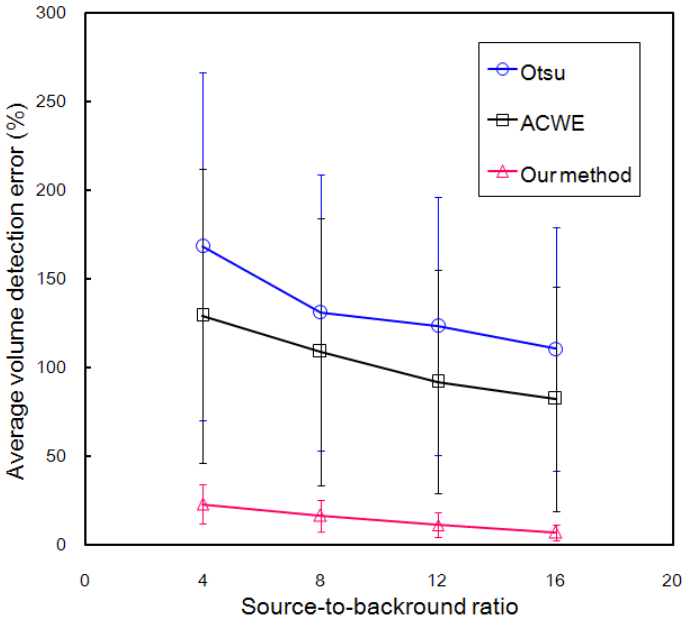

Figure 4.12 Comparison of average volume detection error for all sphere diameters at various SBR.

Table 4.6 and table 4.7 illustrate the *MOP* results by using Otsu's method and traditional ACWE method at various SBR and different sphere diameter. As expected, both methods obtained similarity results. The best *MOPs* were found with larger sphere and larger SBR for both segmentation techniques.

Table 4.6 The results of mutual overlapping part based on Otsu's method.

Sphere diameter (cm)	SBR 4	SBR 8	SBR 12	SBR 16
1.0	0.62	0.64	0.65	0.71
1.3	0.69	0.73	0.73	0.79
1.7	0.77	0.77	0.77	0.81
2.2	0.82	0.82	0.83	0.84
2.8	0.84	0.85	0.85	0.86
3.7	0.88	0.91	0.91	0.92

Table 4.7 The results of mutual overlapping part based on ACWE method.

Sphere diameter (cm)	SBR 4	SBR 8	SBR 12	SBR 16
1.0	0.61	0.62	0.66	0.70
1.3	0.70	0.72	0.73	0.78
1.7	0.77	0.78	0.78	0.82
2.2	0.79	0.83	0.83	0.85
2.8	0.85	0.86	0.87	0.87
3.7	0.89	0.92	0.92	0.92

The descriptive statistics of *MOP* in the IEC/2001 body phantom for the three methods is also summarized in table 4.8. Our method shows the best average and standard deviation *MOP* results of 97 ± 0.02 (90-99) %, while the Otsu's method and ACWE obtained average *MOP* of 79 ± 0.09 (62-92) % and 79 ± 0.09 (61-92) %, respectively. The 3rd quartile for three each segmentation methods were 98 %, 85 % and 86 %, respectively.

In figure 4.13-4.16 illustrate that our method is still provided better results for *MOP* compared to Otsu's method and ACWE method at SBR 4, 8, 12 and 16 respectively.

Table 4.8 Statistics description of *MOP* for Otsu, ACWE and our method.

Method	Maximum	Minimum	Median	3rd Quartile	Mean	SD
Otsu	0.92	0.62	0.82	0.85	0.79	0.09
ACWE	0.92	0.61	0.80	0.86	0.79	0.09
Our method	0.99	0.90	0.97	0.98	0.97	0.02

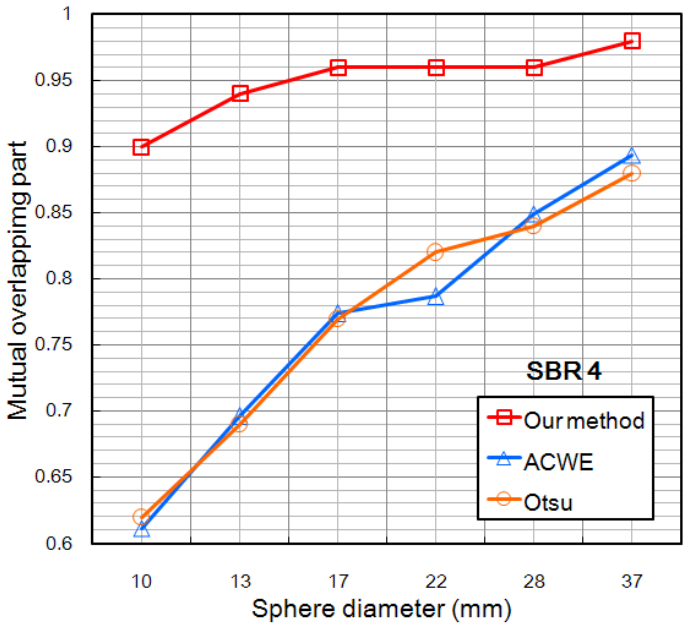

Figure 4.13 *MOP* for Otsu's method, ACWE and our method at SBR 4.

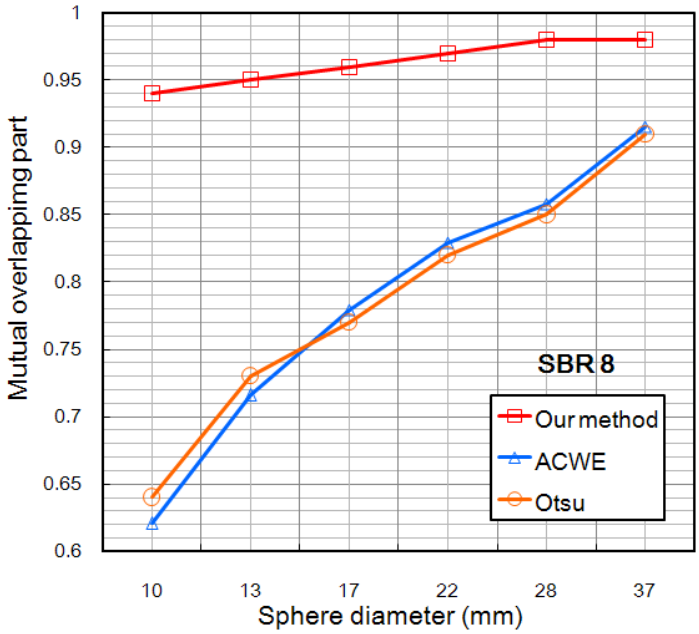

Figure 4.14 *MOP* for Otsu's method, ACWE and our method at SBR 8.

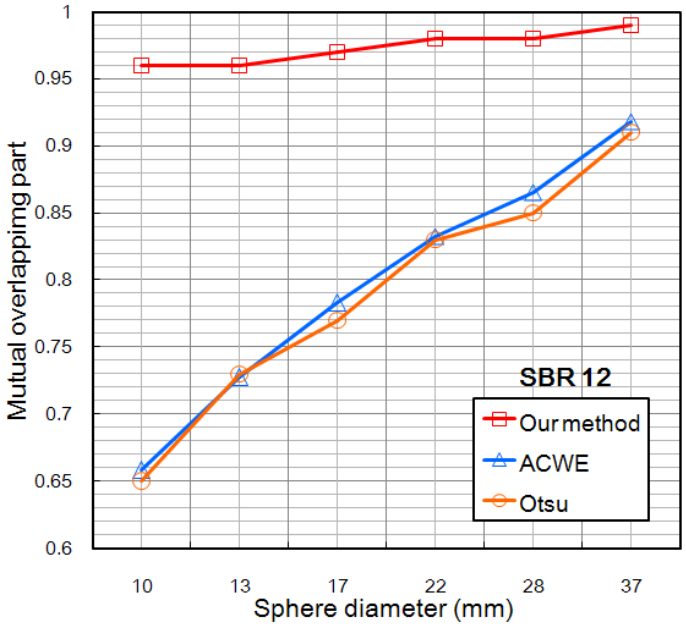

Figure 4.15 *MOP* for Otsu's method, ACWE and our method at SBR 12.

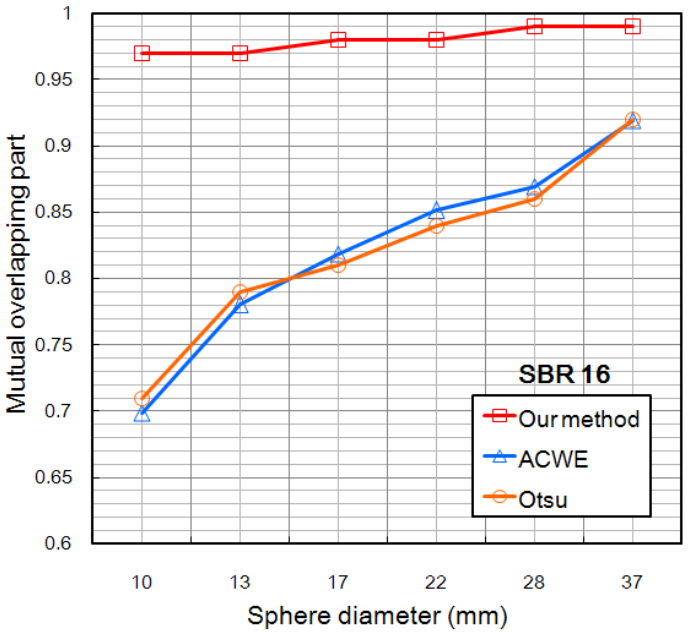

Figure 4.16 *MOP* for Otsu's method, ACWE and our method at SBR 16.

To demonstrate the efficiency of our automatic method, the active contour based on the combination with shifted-optimal threshold was compared with the traditional active contour, ACWE, as illustrated in figure 4.17 (sphere diameter of 1.3 cm, SBR 8). As we can see from the image, the tumor also contains the spillover effect resulting to be smeared from the activity contamination surrounding the tumor.

Our contour can evolve through the blurred edge into the inner part of PET tumor, while the contour cannot successfully segment the boundary of this tumor when we apply with the ACWE. Due to its external force of the contour is not enough, the contour is stopped at the indistinct area when its energy is optimized. As a result, our contour provides the delineation results more accurately than ACWE.

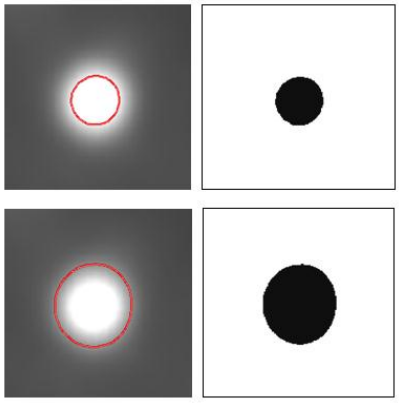

Figure 4.17 The efficiency of active contour by using (upper left) our combined method and (lower left) active contour without edges.

4.2 Segmentation results of patient study

The overview of 10 male patients suffering from esophageal cancer and underwent the PET/CT imaging are illustrated as in table 4.9. The average and standard deviation of patient body weight was 56.3 ± 7.9 (43-72) kg. The average and standard deviation of ^{18}F-FDG activity per patient was 352.8 ± 51.4 (282-443) MBq.

The delineation results of esophageal tumors by both manual and automatic methods are then shown as in table 4.10. The average esophageal tumor volume of 92.78 ± 61.6 (5.91-178.30) cc was manually delineated by radiation oncologist, while the average segmentation result of esophageal tumor volume by automatic method was 88.11 ± 58.8 (6.41-169.24) cc. The average tumor-to-background ratio (TBR) measured in PET esophageal cancer patients was 9.48 ± 2.3 (6.36-13.65). The scatter chart of statistical relation of the tumor volume tracing by both methods for 10 patients are also presented as in figure 4.18 (R^2= *0.993*). According to the results, most of the tumor volume detected by our automatic method is consistently lower than the manual contours outline with an overall average DE_{vol} of -4.06 ± 6.35 %.

Table 4.9 The characteristics of 10 esophageal cancer patients underwent ^{18}F-FDG whole-body PET/CT imaging.

Patient no.	Gender	Age (years)	Body weight (kg)	^{18}F-FDG activity (MBq)
1	Male	64	56.5	377
2	Male	68	60.2	349
3	Male	50	50	282
4	Male	53	43	278
5	Male	45	50	346
6	Male	60	62	413
7	Male	53	58.8	329
8	Male	55	56.2	345
9	Male	59	54	443
10	Male	59	72	366
Average±SD		56.6±6.8	56.3±7.9	352.8±51.4

Table 4.10 The results of tumor delineation in 10 esophageal cancer patients.

Patient no.	Manual method (cc)	Automatic method (cc)	DE_{vol} (%)	TBR
1	5.91	6.41	8.46	7.46
2	33.16	31.86	-3.92	8.30
3	40.53	37.20	-8.22	9.68
4	55.81	48.79	-12.58	6.36
5	66.15	64.15	-3.02	7.19
6	93.86	96.01	2.29	9.21
7	136.84	119.68	-12.54	10.78
8	145.51	140.92	-3.15	10.24
9	171.74	166.80	-2.88	11.96
10	178.30	169.24	-5.08	13.65
Average±SD			-4.06 ± 6.35	9.48±2.3

TBR represents tumor-background ratio in esophageal cancer patients.

Note that these value can be negative and positive, indicating an under/over segmentation of the tumor volume compared with the manual tracing.

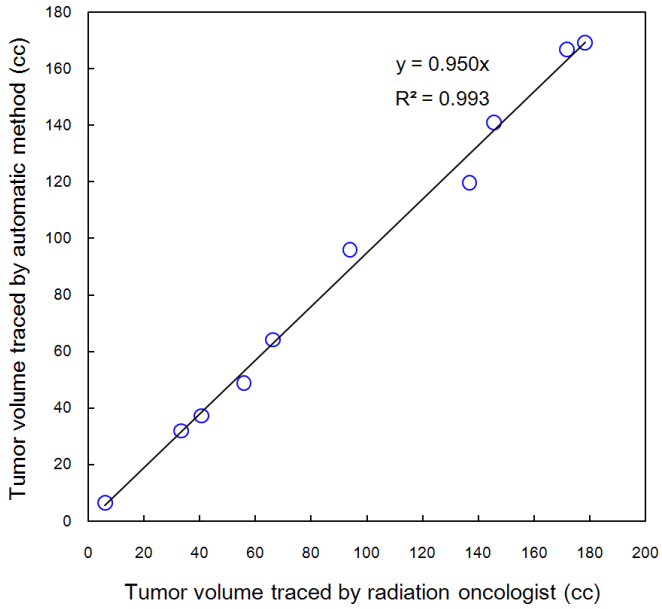

Figure 4.18 The statistical relation between radiation oncologist manual tracing and automatic method for 10 esophageal cancer patients.

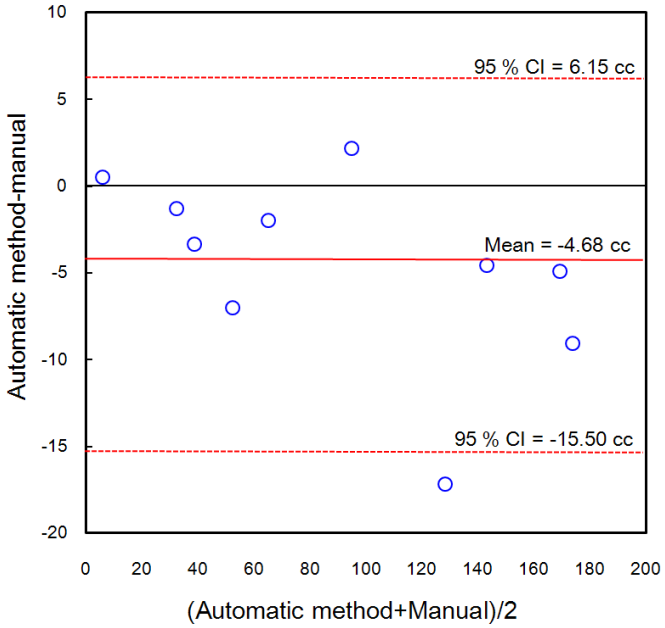

Figure 4.19 Bland-Altman plot between the manual and automatic method (n = 10).

To gain more insight for patient data interpretation, the Bland-Altman analysis between both methods is shown as in figure 4.19. Mean deviation of -4.68 cc was seen with 95% confidence interval (CI) ranged from -15.50 to 6.15 cc. Most of the tumor volume delineation by automatic method is in agreement with manually drawn by radiation oncologist.

Table 4.11 The difference of diameter equivalent of esophageal tumor between manual and automatic methods.

Patient no.	D_1 (cm)	D_2 (cm)	D_1- D_2 (cm)
1	2.24	2.30	-0.06
2	3.99	3.93	0.05
3	4.26	4.14	0.12
4	4.74	4.53	0.21
5	5.02	4.97	0.05
6	5.64	5.68	-0.04
7	6.39	6.11	0.28
8	6.52	6.46	0.07
9	6.90	6.83	0.07
10	6.98	6.86	0.12
Average±SD	5.62±1.52	5.52±1.48	0.1±0.1

D_1 represents diameter equivalent from manual method.

D_2 represents diameter equivalent from automatic method.

An example of the cross-sectional slice of abdomen with ^{18}F-FDG esophageal tumor of whole-body PET/CT imaging is shown in figure 4.20(a). To compare the efficiency of segmentation results, the initial contour (circle) is placed within the PET esophageal tumor region as shown in figure 4.20(b). As the global energy of ACWE finds only the brightest region of the image, the contour cannot successfully segment this tumor when we apply this model as shown in figure 4.20(c). A more satisfactory result is provided by our combined method as illustrated in figure 4.20(d). We can clearly see that the contour can evolve to the desired boundary of a tumor correctly yielding perfect delineation result.

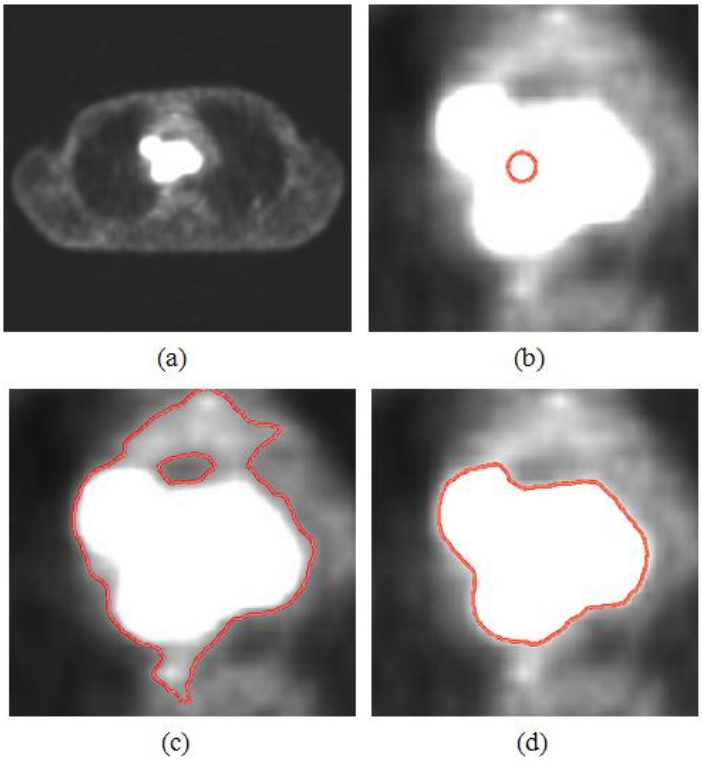

Figure 4.20 (a) The esophageal tumor of whole-body PET image (b) the initial contour within the tumor region (c) the result by active contour without edges (d) our method.

The efficiency of our method is also demonstrated with the small tumor structure as shown in figure 4.21. As we can see from the image, the tumor appears to be smeared at its surrounding area from spillover effect that usually occurs in small structure in PET image. The contrast between the tumor and the surrounding tissue is low. The segmentation result by ACWE is still not successfully segment the tumor, while the contour can evolve to the boundary of a tumor correctly yielding the delineation result by our method has been succeeded.

The segmentation results of the esophageal tumor by using only the thresholding method based on Otsu and shifted-optimal thresholding are shown as in figure 4.22. As both of threshold-based segmentation method is based on the separation light and dark region of the image, lead to incorrect segmentation and some parts containing in the background was also segmented.

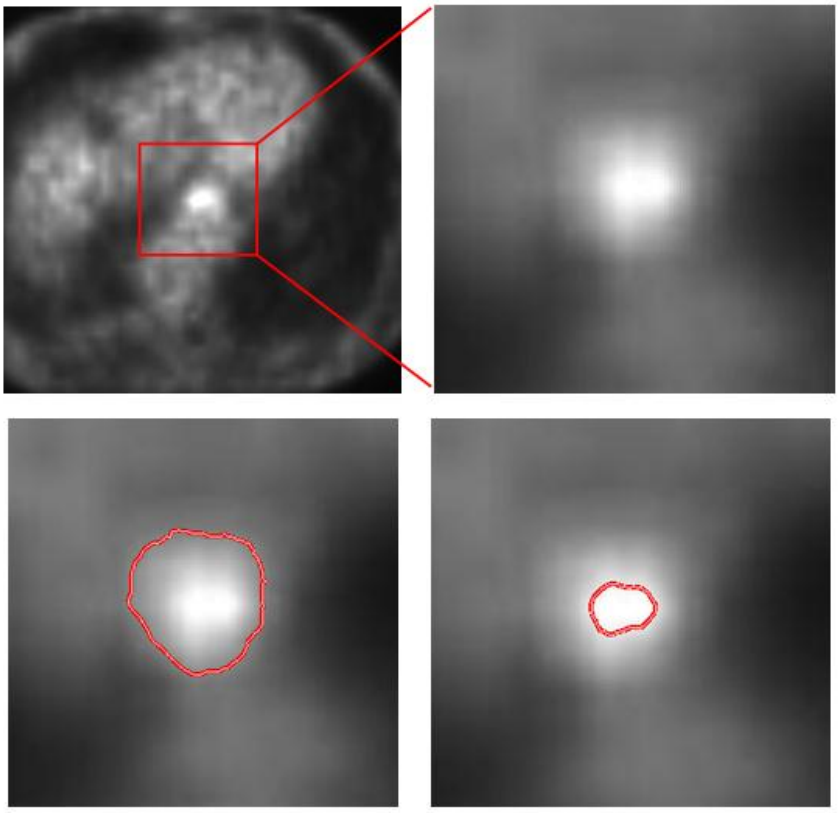

Figure 4.21 The efficiency of the active contour in esophageal tumor with small structure (left lower) segmentation result by ACWE and (right lower) by our method.

Figure 4.22 The segmentation results based on threshold method (left) cross-sectional slice of esophageal cancer tumor (middle) by Otsu's method and (right) by shifted-optimal thresholding method.

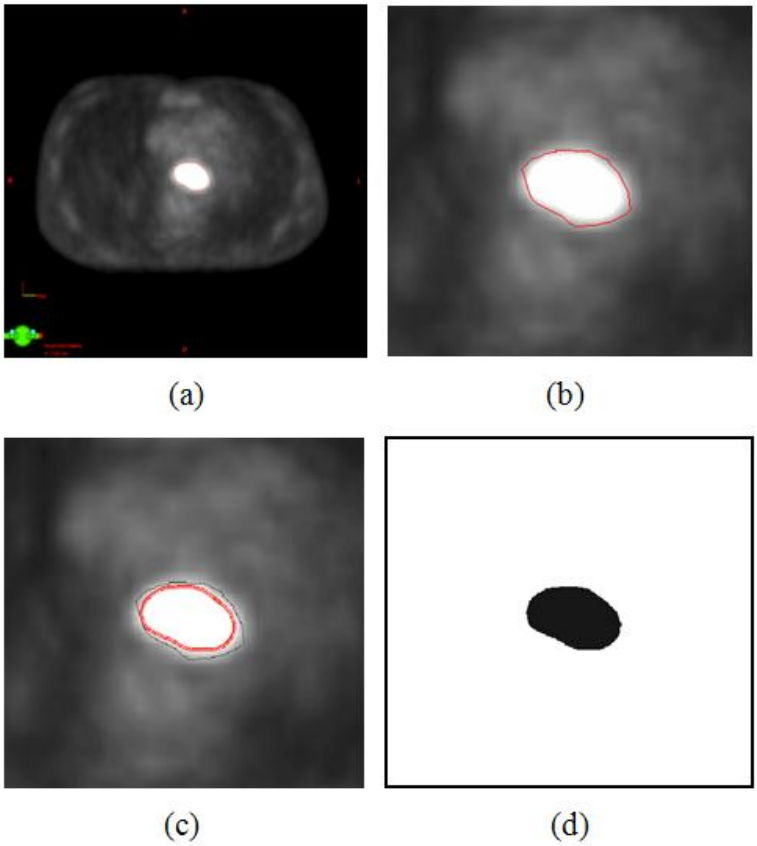

Figure 4.23 Comparison of esophageal tumor tracing with round shape. (a) Cross-sectional slice of PET thoracic image. (b) Tumor traced by radiation oncologist. (c) Tumor traced by automatic method and (d) binary image of a tumor.

An example of the tumor delineation with round shape in 45-year-old man (body weight 50 kg, ^{18}F-FDG activity 346 MBq) suffering from esophageal cancer is shown as in figure 4.23. The tumor volume of 66.15 cc was obtained by manual method, while the tumor volume detected by automatic method was 64.15 cc. We can see that the tumor area of the final contour traced by automatic method was slightly different from manual method of -3.02 %.

The delineation result of the esophageal tumor with irregular shape in 53-year-old man (body weight 58.8 kg, ^{18}F-FDG activity 329 MBq) is also illustrated in figure 4.24. We can observe that the contour can evolve to the concavity area of a tumor. This result leading to the tumor volume traced by manual method (136.84 cc) was slightly greater than the automatic method (119.68 cc). The variability of tumor volume of -12.54 % was obtained between each two methods.

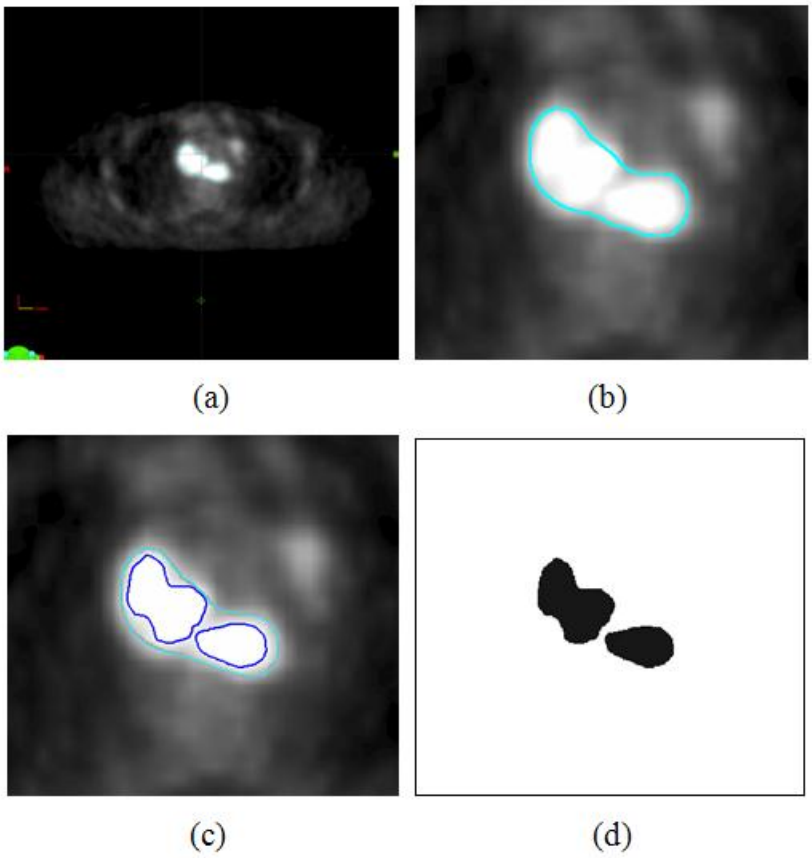

Figure 4.24 Comparison of esophageal tumor tracing with irregular shape. (a) Cross-sectional slice of PET thoracic image. (b) Tumor traced by radiation oncologist. (c) Tumor traced by automatic method and (d) binary image of a tumor.

CHAPTER V

DISCUSSION AND CONCLUSIONS

5.1 Discussion

The accuracy and consistency of the tumor delineation in PET image plays an important role in radiation treatment planning process and patient follow-up evaluation (Geets *et al*., 2007; Lee, 2010). Functional imaging such as PET is growing up to define subclinical region of the metabolic tumor (Boellaard, 2009; Cheebsumon *et al.*, 2011). Manual contouring, subjective task, has been shown large variation with different operator, and time consuming due to delineate the tumor boundary slice-by-slice (Li *et al*., 2008). In this study, an automatic algorithm to trace the tumor boundary in PET image is proposed and evaluated. The algorithm is aimed to reduce the variability for delineating PET tumor boundary.

Thresholding is one of the simplest methods for image segmentation to separate object from the background region. However, to achieve smoother results for segmenting the tumor, each optimal threshold value has been used to embed into external force of a region-based active contour energy function instead. This could be allowed both algorithms to perform consecutively. The image segmentation utilizing active contour and thresholding value method is recently presented by Chen *et al.* (Chen *et al*., 2010). However, their studies performed in other imaging modalities, the accuracy of metabolic tumor volume in clinical situation is neglected. Moreover, there was no limitation on spatial resolution, partial volume effect and indistinct boundary as the PET image.

The shifted-optimal thresholding is derived based on the contrast between the tumor and background in each slice (Drever *et al.*, 2007). Therefore, the different threshold level can be obtained automatically from the histogram distribution by this method. The appropriate tumor threshold in PET image based on shifted-optimal threshold method corresponds to the recently studied the property of Otsu's threshold by Xu *et al.* (Xu *et al*., 2011).

As seen in figure 5.1, in theory, the ideal threshold to separate two regions in histogram distribution is located at the intersection point. Due to this point is far away

from the mean level of the region with large variance, a part of pixels from each cluster will be split into the smaller variance region in order to obtain the equality. Therefore, the optimal threshold according to Otsu's method will be biased from the intersection point toward the center of the cluster with larger variance if there is a significant difference of the variance between the object and background.

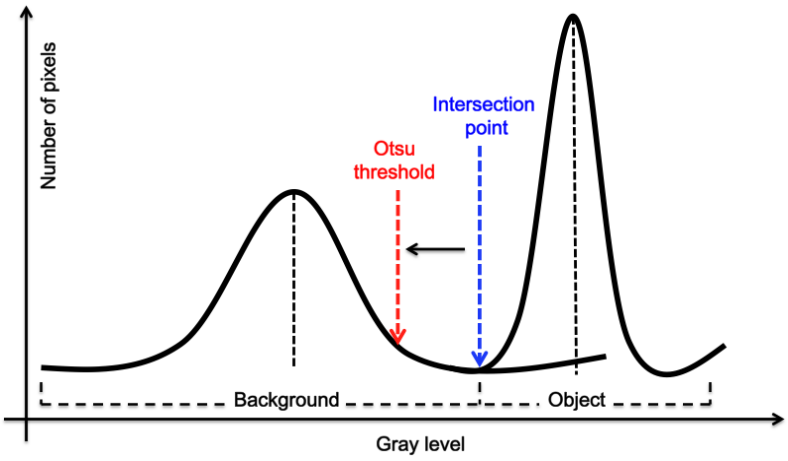

Figure 5.1 Otsu's threshold with significantly different variances of two clusters.

In PET image, as the Otsu's threshold is deviated to the background region with the variance larger than the tumor, the threshold suitable for the PET tumor should be shifted toward higher gray value.

Since the influence of partial volume effect and lack of clear boundary (blurring effect) usually occur in PET image (Jentzen *et al.*, 2007), the active contour utilizing the region-based information will be stopped at blurred edge area of PET tumor when an objective energy function is optimized (figure 4.17). For our study, the imbalance of positive weighting parameters is one factor to attract the contour to the PET tumor boundary. Moreover, since the active contour is dominated by the appropriate tumor threshold, the significant region of an image is detected while excluding the weak part or the background. This effect can be demonstrated by our experimental results with patient studies (figure 4.20 and figure 4.21). Furthermore, even though all tested images in this study did not use de-blurring or de-noising filters, our contour can evolve to PET tumor boundary correctly.

Phantom study

The high accurate detected volume in IEC/2001 torso phantom is obtained with higher SBR and large spheres (1.51 %, SBR 16). In contrast, the accurate detected volume is reduced in smaller sphere (36.53 %) with low SBR due to the partial volume effect, and contrast (signal) between sphere and background is lower (Jentzen *et al.,* 2007, Li *et al.,* 2008, van Dalen *et al.,* 2007). However, when the difference of tumor volume (cc) is considered as in figure 4.4, the volume mismatch tends to increase with increasing the sphere diameter. This discrepancy results can be reasonably explained that the smallest sphere containing only a few voxels in the images; therefore, the volume detection error (DE_{vol}) is higher even though only a few voxels mismatch is found. Hence, the large error in smallest sphere at SBR 4 of 36.53 % can be obtained, although its different volume detection is only 0.19 cc.

This phenomenon can be seen obviously according to the Bland-Altman analysis as illustrated in figure 4.5. Out of range of the agreement are seen with the two largest sphere diameters of 1.6 cc and 2.02 cc at SBR 4, while the DE_{vol} of these two spheres are found only 13.91 % and 7.61%. Due to the increasing number of slices corresponds to the large spherical volume, this result in the increasing the difference of tumor volume especially at low SBR.

According to the PET tumor tracing in this study is based on the combination between active contour and thresholding method, our results is comparable to Li *et al.* (Li *et al.*, 2008) study. They presented a PET tumor delineation utilizing a dual-front active contour and adaptive region-growing. Their best segmentation results in anthropomorphic phantom are obtained with average *MOP* of 96.95 %, and average DE_{vol} of -6.2 % at SBR 15 in actual tumor volume of 20 cc, while our results in the average *MOP* of 98 % and the average DE_{vol} of 1.51 % at SBR 16 are provided with the actual tumor volume of 26.53 cc.

Unlike the threshold-based method (Brambilla *et al.,* 2008; Daisne *et al.,* 2003; Drever *et al.,* 2007; Jentzen *et al.,* 2007; van Dalen *et al.,* 2007), our automatic method is independent of the SBR threshold-volume curves, fitting model, sphere diameter or FWHM measurement. These parameters are usually derived for a specific PET scanner (Day *et al.,* 2009; Li *et al.,* 2008). While the relative threshold level

(RTL) studied by van Dalen *et al.* (van Dalen *et al*., 2007), the point spread function (PSF) is prior required.

Patient study

Most of the tumor in ^{18}F-FDG PET images of esophageal cancer show high uptake of positron-emitting radiotracer (Bruzzi *et al.,* 2007; Hyun *et al.,* 2010; Zhong *et al.,* 2009). This evidence could be confirmed on our clinical TBR with the average of 9.48 ± 2.3 in PET/CT imaging of esophageal cancer patients. Due to the complex shape of the tumor, the large volume mismatch of -12.54 % was seen in patient no.7 (see the figure in Appendix A). The segmentation error may reduce when the PET tumor size was approximately 5.6 cm. This value was determined according to the formula $D = (v \times 6/\pi)^{1/3}$ of diameter equivalent of the correlation between manual and automatic methods.

Since the esophagus is a part of digestive tract containing in the thoracic, the uncertainties of tumor boundary tracing by both automatic and manual methods in PET image might be influenced due to the patient respiratory motion, internal organ movement and swallowing. These effects are also influenced the visualization and interpretation of freehand tumor boundary contouring by radiation oncologist. While in the phantom study, the PET data have been acquired in a static situation, lacking in movement of the tumor location. However, we found that most of the detected volume and the *MOP* in our study shows good agreement with the true volume; furthermore, the clinically implementation in oncology patient suffering from esophageal cancer is also provided satisfactory results with arbitrary shape of the PET tumor.

According to the segmentation results of patient data, we can see that the contour could be deformed through indistinct boundary of PET image even though in the concavity areas of the tumor. The delineation results had not been compared to the pathologic report, the gold standard to validate tumor volume (Hyun *et al*., 2010; Zhong *et al.,* 2009), it is a limitation of this study. However, our study could be contributed a knowledge of tumor delineation in PET image, and demonstrated that the combined method can improve the accuracy and consistency of PET tumor tracing as well. This leading to better delineation results when compared to either threshold-based or traditional active contour based.

5.2 Conclusions

An automatic method to delineate the boundary of tumor in PET image has been designed in this study. The method had been tried with patients suffering from esophageal cancer underwent whole-body ^{18}F-FDG PET/CT imaging. In IEC/2001 body phantom, our method provides high average area similarity and accurate PET tumor delineation. The least volume detection error is found in largest spherical tumor (3.7 cm) of 1.51 % at SBR 16. The average volume detection error between our automatic method and manual tracing of -4.06±6.35 % is obtained. Since the method is robust to noise, independent SBR threshold-volume curve, sphere diameter or lesion size measurement yielding better PET volume segmentation results when compared to other published methods. Most agreement between both automatic and manual methods in a Bland-Atman analysis within 95% CI is also seen. The advantages of this study are the promising improvement of the accuracy and consistency for PET tumor contouring in esophageal cancer patients. Furthermore, the method will have positive contribution to clinical PET image analysis.

5.3 Recommendations

As the automatic method provides high accuracy and consistency for tracing PET tumor boundary, the algorithm can be used as a second opinion guideline for radiation oncologist or operator when performing PET tumor delineation to improve the inter-observer and intra-observer reliability and to produce more consistent results. In addition, in order to implement the algorithm into radiation treatment planning process in the future, the algorithm is necessary to verify with other constraints of cancer to improve the confidence of automatic program.

Since the algorithm is based on the combination between two segmentation methods to improve smoother results, the algorithm could be further developed either threshold or active contour that suitable for those key image feature. Especially the threshold that used to combine into active contour energy function, it could be adopted in accordance with the desired applications.

REFERENCES

Abouzied, M. M., Crawford, E. S., and Nabi, H. A. ^{18}F-FDG imaging: pitfalls and artifacts. Journal of Nuclear Medicine Technology 33 (2005): 145-155.

Ammar, M., Mahmoudi, M., Chikh, M. A., and Abbou, A. Endocardial border detection in cardiac magnetic resonance images using level set method. Journal of Digital Imaging 25 (2012): 294-306.

Bland, J. M., Altman, D. G., Statistical methods for assessing agreement between two methods of clinical measurement. Lancet 1 (1986): 307-310.

Boellaard, R. Standards for PET image acquisition and quantitative data analysis. Journal of Nuclear Medicine 50 (2009): 11S-20S.

Boellaard, R., et al. FDG PET and PET/CT: EANM procedure guidelines for tumor PET imaging: version 1.0. European Journal of Nuclear Medicine and Molecular Imaging 37 (2010): 181-200.

Boscolo, R., Brown, M. S., and McNitt-Gray, M. F. Medical image segmentation with knowledge-guided robust active contours. Radiographics 22 (2002): 437-448.

Brambilla, M., Matheoud, R., Secco, C., Loi, G., Krengli, M., and Inglese, E., Thresholding segmentation for PET target volume delineation in radiation treatment planning: the role of target-to-background ratio and target size. Medical Physics 35 (2008): 1207-1213.

Bruzzi, J. F., et al. PET/CT of esophageal cancer: its role in clinical management. Radiographics 27 (2007): 1635-1652.

Caselles, V., Kimmel, R., and Sapiro, G. Geodesic active contour. International Journal of Computer Vision 22 (1997): 61-79.

Chan, T., and Vese, L. Active contours without edges. IEEE Transactions on Image Processing 10 (2001): 266-277.

Cheebsumon, P., et al. Effect of images characteristics on performance of tumor delineation methods: a test-retest assessment. Journal of Nuclear Medicine 52 (2011): 1550-1558.

Cheebsumon, P., et al. Measurement of metabolic tumor volume: static versus dynamic FDG scans. EJNMMI Research 1 (2011): 35.

Cheebsumon, P., Yaqub, M., van Velden, F. H. P., Hoekstra, O. S., Lammertsma, A. A., and Boellaard, R. Impact of ^{18}F-FDG PET imaging parameters on automatic tumor delineation: need for improved tumor delineation methodology. European Journal of Nuclear Medicine and Molecular Imaging 38 (2011): 2136-2144.

Chen, G., Zhang, H., Chen, I., and Yang, W. Active contours with thresholding value for image segmentation. The 20th IEEE International Conference on Pattern Recognition (2010): 2266-2269.

Cheng-Liao, J., and Qi, J. PET image reconstruction with anatomical edge guided level set prior. Physics in Medicine and Biology 56 (2011): 6899–6918.

Cheng-Liao, J., and Qi, J. Segmentation of mouse dynamic PET image using a multiphase level set method. Physics in Medicine and Biology 55 (2011): 6549–6569.

Clas, P., Groeschel, S., and Wilke, M. A semi-automatic algorithm for determining the demyelination load in metachromatic leukodystropy. Academic Radiology 19 (2012): 26-34.

Cremers, D., Rousson, M., and Deriche, R. A review of statistical approach to level set segmentation: integrating color, texture, motion and shape. International Journal of Computer Vision 72 (2007): 195-215.

Daisne, J. F., Sibomana, M., Bol, A., Doumont, T., Lonneux, M., and Gregoire, V. Tri-dimensional automatic segmentation of PET volumes based on measured signal-to-noise ratios: influence of reconstruction algorithms. Radiotherapy and Oncology 69 (2003): 247-250.

Daube-Witherspoon, M. E., et al. PET performance measurements using the NEMA NU 2-2001 standard. Journal of Nuclear Medicine 43 (2002): 1398-1409.

Day, E., et al. A region growing method for tumor volume segmentation on PET images for rectal and anal cancer patients. Medical Physics 36 (2009): 4339-4358.

Dewalle-Vignion, A. S., Betrouni, N., Lopez, R., Hugo, D., Stute, S., and Vermandel, M. A new method for volume segmentation of PET images based on possibility theory. IEEE Transactions on Medical Imaging 30 (2011): 409-423.

Drever, L., Roa, W., McEwan, A., and Robinson, D. Iterative threshold segmentation for PET target volume delineation. Medical Physics 34 (2007): 1253-1265.

Enzinger, P. C., and Mayer, R. J. Esophageal cancer. New England Journal of Medicine 349 (2003): 2241-2252.

Erdi, Y. E., Nehmeh, S. A., Mulnix, T., Humm, J. L., and Watson, C. C. PET performance measurements for an LSO-based combined PET/CT scanner using the national electrical manufacturers association NU 2-2001 standard. Journal of Nuclear Medicine 45 (2004): 813-821.

Fahey, F. H. Data acquisition in PET imaging. Journal of Nuclear Medicine Technology 30 (2002): 39-49.

Ford, E. C., et al. Tumor delineation using PET in head and neck cancers: threshold contouring and lesion volumes. Medical Physics 33 (2006): 4280-4288.

Geets, X., Lee, J. A., Bol, A., Lonneux, M., and Gregoire, V. A gradient-based method for segmenting FDG-PET images: methodology and validation. European Journal of Nuclear Medicine and Molecular Imaging 34 (2007): 1427-1438.

Hatt, M., Rest, C. C., van Baardwijk, A., Lambin, P., Pradier, O., and Visvikis, D. Impact of tumor size and tracer uptake heterogeneity in ^{18}F-FDG PET and CT non-small cell lung cancer tumor delineation. Journal of Nuclear Medicine 52 (2011): 1690-1697.

Hofheinz, F., Dittrich, S., Potzsch, C., and van den Hoff, J. Effects of cold sphere walls in PET phantom measurements on the volume reproducing threshold. Physics in Medicine and Biology 55 (2010): 1099-1113.

Hyun, S. H., et al. Prognostic value of metabolic tumor volume measured by ^{18}F-fluorodeoxyglucose positron emission tomography in patients with esophageal carcinoma. Annals of Surgical Oncolology 17 (2010): 115-122.

International Atomic Energy Agency. The role of PET/CT in radiation treatment planning for cancer patient treatment. Vienna, Austria: IAEA, (2008).

International Atomic Energy Agency. Quality assurance for PET and PET/CT systems. Vienna, Austria: IAEA, (2009).

Jentzen, W., Freudenberg, L., Eising, E. G., Heinze, M., Brandau, W., and Bockisch, A. Segmentation of PET volumes by iterative image thresholding. Journal of Nuclear Medicine 48 (2007): 108-114.

Kass, M., Witkin, A., and Terzopoulos, D. Snakes: active contour models. International Journal of Computer Vision 1 (1988): 321–331.

Khamwan, K., Krisanachinda, A., and Pluempitiwiriyawej, C. Determination of tumor boundary on PET images using active contour coupled with optimal thresholding: a phantom study. The 11th Asia-Oceania Congress of Medical Physics (2011).

Krause, B. J., Herrmann, K., Wieder, H., and Buschenfelde, C. M. ^{18}F-FDG PET and ^{18}F-FDG PET/CT for assessing response to therapy in esophageal cancer. Journal of Nuclear Medicine 50 (2009): 89S-96S.

Krug, R., Boese, J. M., and Schad, L. R. Determination of aortic compliance from magnetic resonance imaging using an automatic active contour model. Physics in Medicine and Biology 48 (2003): 2391-2404.

Lankton, S., and Tannenbaum, A. Localizing region-based active contours. IEEE Transactions on Image Processing 17 (2008): 2029-2039.

Lee, J. A. Segmentation of positron emission tomography images: some recommendations for target delineation in radiation oncology. Radiotherapy and Oncology 96 (2010): 302-307.

Lewellen, T. K. Recent developments in PET detector technology. Physics in Medicine and Biology 53 (2008): R287-R317.

Li, H., et al. A novel PET tumor delineation method based on adaptive region-growing and dual-front active contours. Medical Physics 35 (2008): 3711-3721.

Ly, J., et al. Semi-automatic analysis of standardized uptake values in serial PET/CT studies in patients with lung cancer and lymphoma. BMC Medical Imaging (2012): 12-6.

Lyer, R. B., Silverman, P. M., Tamm, E. P., Dunnington, J. S., and Dubrow, R. A. Diagnostic, staging, and follow-up of esophageal cancer. American Journal of Roentgenology 181 (2003): 785-793.

Macmanus, M., and Leoung, T. Incorporating PET information in radiation theraphy treatment planning. Biomedical Imaging and Intervention Journal 3(1) (2007): e4.

Mittra, E., and Quon, A. Positron emission tomography/computed tomography: the current technology and applications. Radiologic Clinics of North America 47 (2009): 147-160.

Mumford, D., and Shah, J. Optimal approximations by piecewise smooth functions and associated variational problems. Communications on Pure and Applied Mathematics 42 (1989): 577-685.

National Electrical Manufacturers Association. NEMA NU 2-2007: Performance Measurements of Positron Emission Tomographs. Rosslyn, VA: NEMA, (2007).

Nehmah, S. A., et al. An iterative technique to segment PET lesions using a Monte Carlo based mathematical model. Medical Physics 36 (2009): 4803-4809.

Osher, S., and Sethian, J. A. Fronts propagating with curvature-dependent speed: algorithms based on Hamilton–Jacobi formulation. Journal of Computational Physics 79 (1988): 12–49.

Otsu, N. A threshold selection method from gray-level histograms. IEEE Transactions on System, Man, and Cybernetics 9 (1979): 62-66.

Pan, T., and Mawlawi, O. PET/CT in radiation oncology. Medical Physics 35 (2008): 4955-4966.

Pasawang, P., Krisanachinda, A., Sontrapornpol, T., and Navikacheevin, C. Performance evaluation of a Biograph 16 Hi-Rez PET scanner at King Chulalongkorn Memorial Hospital. Thai Journal of Radiological Technology 31 (2006): 9-14.

Phumeechanya, S., Pluempitiwiriyawej, C., and Thongvigitmanee, S. Active contour using local regional information on extendable search line (LRES) for image segmentation. IEICE Transactions on Information and Systems E93-D (2010): 1625-1635.

Pichler, B. J., Wehrl, H. F., and Judenhofer, M. S. Latest advances in molecular imaging instrumentation. Journal of Nuclear Medicine 49 (2008): 5S-23S.

Pogam, A., et al. Evaluation of a 3D local multi-resolution algorithm for the correction of partial volume effects in positron emission tomography. Medical Physics 38 (2011): 4920-4933.

Prieto, E., et al. Voxel-based analysis of dual-time point ^{18}F-FDG PET images for brain tumor identification and delineation. Journal of Nuclear Medicine 52 (2011): 865-872.

Saha, G. B. Basics of PET imaging: physics, chemistry, and regulations. New York: Springer, (2005).

Sanni, K., Dewal, M. L., and Rohit, M. A fast region-based active contour model for boundary detection of echocardiographic image. Journal of Digital Imaging 25 (2012): 271-278.

Sonka, M., Hlavac, V., and Boyle, R. Image processing, analysis, and machine vision. Toronto, Ontario: Thomson Learning, (2008).

Soret, M., Bacharach, S. L., and Buvat, I. Partial volume effect in PET tumor imaging. Journal of Nuclear Medicine 48 (2007): 932-945.

Timmerman, R., and Xing, L. Image-guided and adaptive radiation therapy. Philadelphia: Lippincott Williams & Wilkins, (2009).

Townsend, D. W. Dual-modality imaging: combining anatomy and function. Journal of Nuclear Medicine 49 (2008): 938–955.

Townsend, D. W., Carney, J., Yap, J. T., and Hall, N. C. PET/CT today and tomorrow. Journal of Nuclear Medicine 45 (2004): 4S–14S.

Tylski, P., et al. ^{18}F-FDG PET images segmentation using morphological watershed: a phantom study. IEEE Nuclear Science Symposium Conference Record 4 (2006): 2063-2067.

van Dalen, J. A., et al. A novel iterative method for lesion delineation and volumetric quantification with FDG PET. Nuclear Medicine Communications 28 (2007): 485-493.

Vauclin, S., Doyeux, K., Hapdey, S., Edet-Sanson, A., Vera, P., and Gardin, I. Development of generic thresholding algorithm for the delineation of F-FDG PET-positive tissue: application to the comparison of three thresholding models. Physics in Medicine and Biology 54 (2009): 6901-6916.

Verel, I., Visser, G. W. M., and van Dongen, G. A. The promise of immune-PET in radioimmunotherapy. Journal of Nuclear Medicine 46 (2005): 164S-171S.

Way, T. W., et al. Effect of CT scanning parameters on volumetric measurements of pulmonary nodules by 3D active contour segmentation: a phantom study. Physic in Medicine and Biology 53 (2008): 1295-1312.

Westerterp, M., et al. Quantification of FDG PET studies using standardized uptake values in multi-centre trials: effects of image reconstruction, resolution and ROI definition parameters. European Journal of Nuclear Medicine and Molecular Imaging 34 (2007): 392-404.

Wieder, H. A., Stahl, A., Lordicks, F., and Ott, K. PET in Oncology. New York: Springer, (2008).

Xu, X., Xu, S., Jin, L., and Song, E. Characteristic analysis of Otsu threshold and its applications. Pattern Recognition Letters 32 (2011): 956-961.

Yu, S. Review of ^{18}F-FDG synthesis and quality control. Biomedical Imaging and Intervention Journal 2(4) (2006): e57.

Zhang, H., Liu, J., Zhu, Z., and Li, H. An automated and simple method for brain MR image extraction. Biomedical Engineering Online 10 (2011): 81.

Zhang, K., Zhang, L., Song, H., and Zhou, W. Active contours with selective local or global segmentation: a new formulation and level set method. Image and Vision Computing 28 (2010): 668-678.

Zhang, Y., Matuszewki, B. J., Shark, L. K., and Moore, C. J. Medical image segmentation using new hybrid level-set method. IEEE The 5th International Conference Biomedical Visualization (2008): 71-76.

Zhong, X., et al. Using ^{18}F-fluorodeoxyglucose positron emission tomography to estimate the length of gross tumor in patients with squamous cell carcinoma of the esophagus. International Journal of Radiation Oncology, Biology, Physics 73 (2009): 136-141.

APPENDICES

Appendix A

Example of tumor in PET/CT imaging traced by automated algorithm in 10 esophageal cancer patients.

Patient no.	1
Gender	male
Age (years)	64
Patient weight (kg)	56.5
^{18}F-FDG injected activity (MBq)	377
Tumor volume traced by radiation oncologist (cc)	5.91
Tumor volume traced by automated algorithm (cc)	6.41
Volume mismatch (%)	8.46

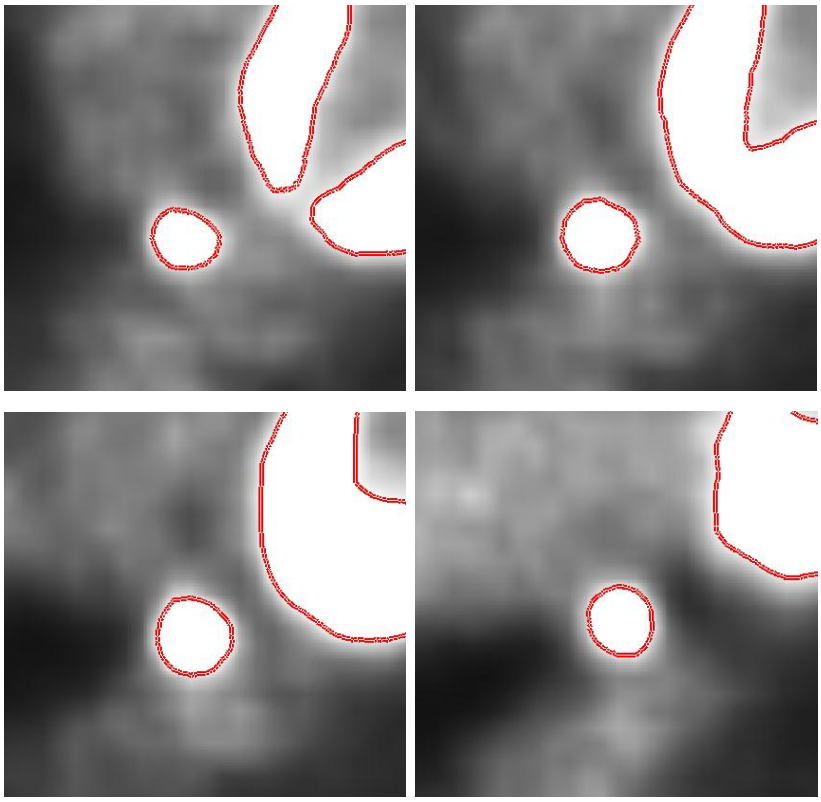

Patient no.	2
Gender	male
Age (years)	68
Patient weight (kg)	60.2
^{18}F-FDG injected activity (MBq)	349
Tumor volume traced by radiation oncologist (cc)	33.16
Tumor volume traced by automated algorithm (cc)	31.86
Volume mismatch (%)	3.92

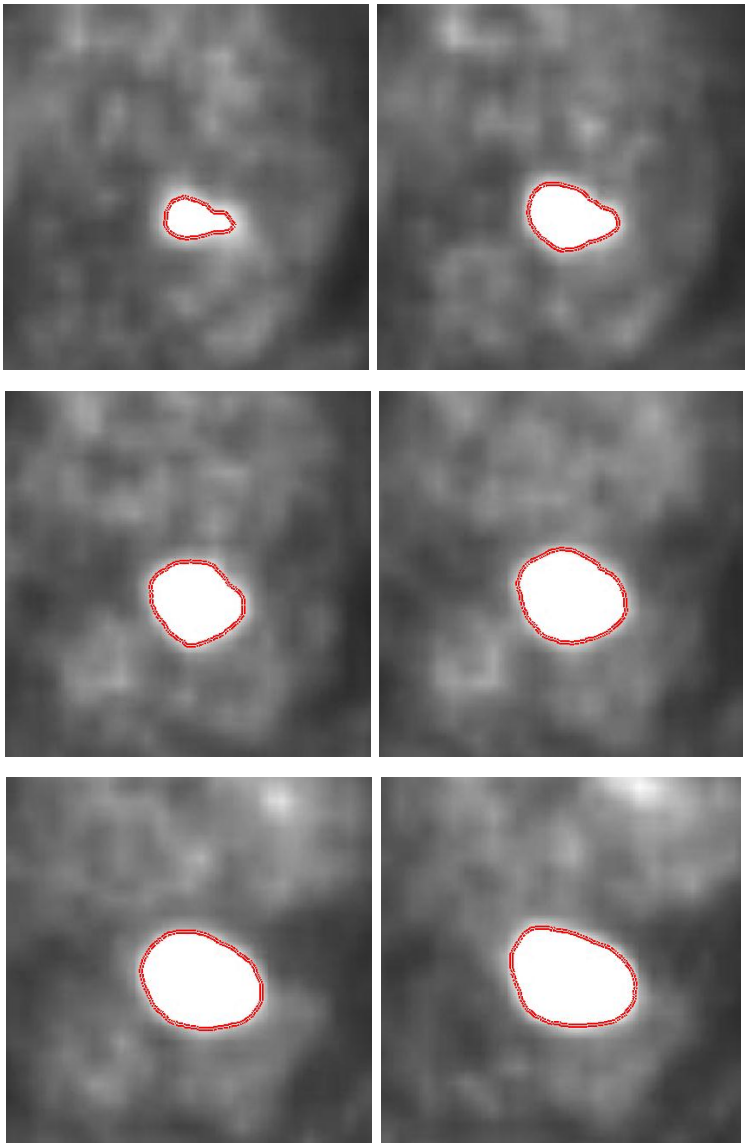

Patient	3
Gender	male
Age (years)	53
Patient weight (kg)	43
^{18}F-FDG injected activity (MBq)	278
Tumor volume traced by radiation oncologist (cc)	40.53
Tumor volume traced by automated algorithm (cc)	37.20
Volume mismatch	8.22

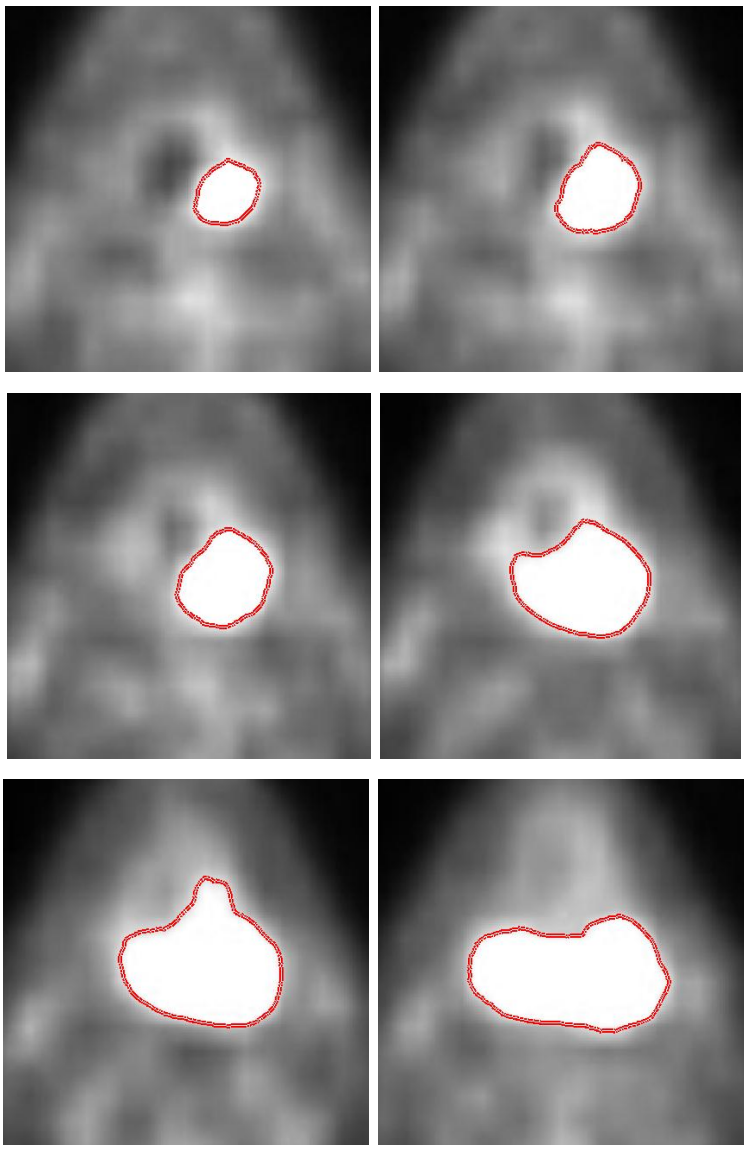

Patient no.	4
Gender	male
Age (years)	45
Patient weight (kg)	50
^{18}F-FDG injected activity (MBq)	346
Tumor volume traced by radiation oncologist (cc)	55.81
Tumor volume traced by automated algorithm (cc)	48.79
Volume mismatch (%)	12.58

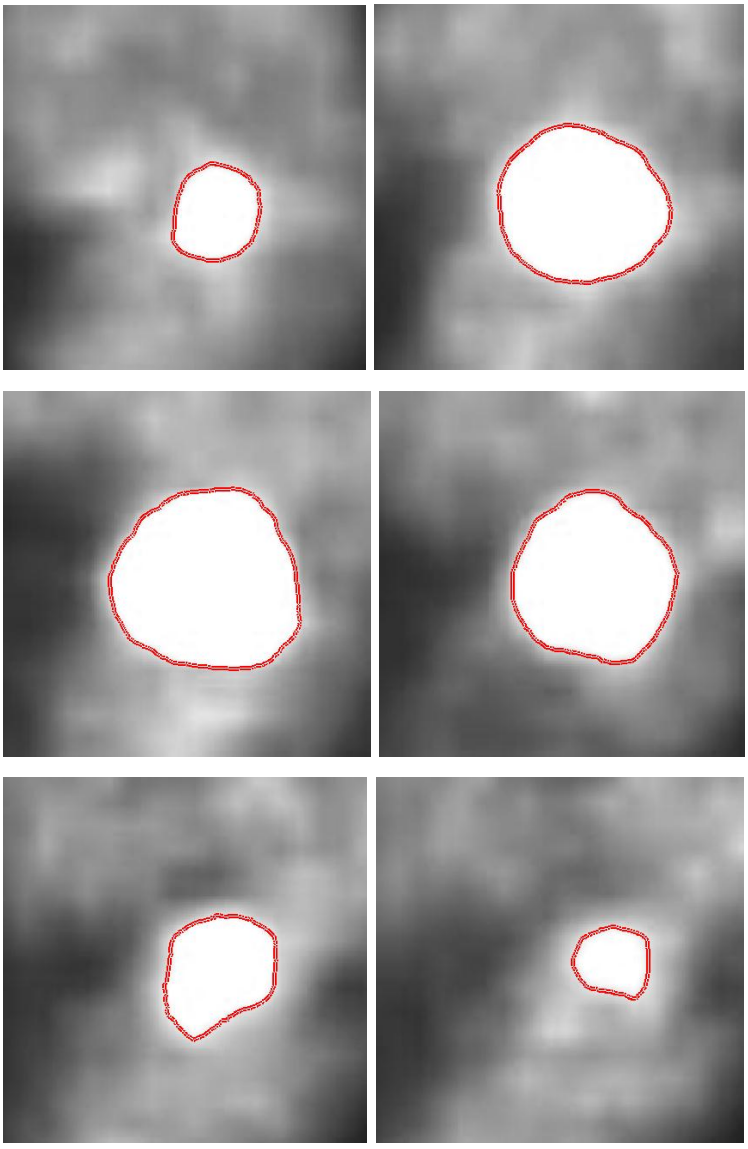

Patient no.	5
Gender	male
Age (years)	59
Patient weight (kg)	72
^{18}F-FDG injected activity (MBq)	366
Tumor volume traced by radiation oncologist (cc)	66.15
Tumor volume traced by automated algorithm (cc)	64.15
Volume mismatch (%)	3.02

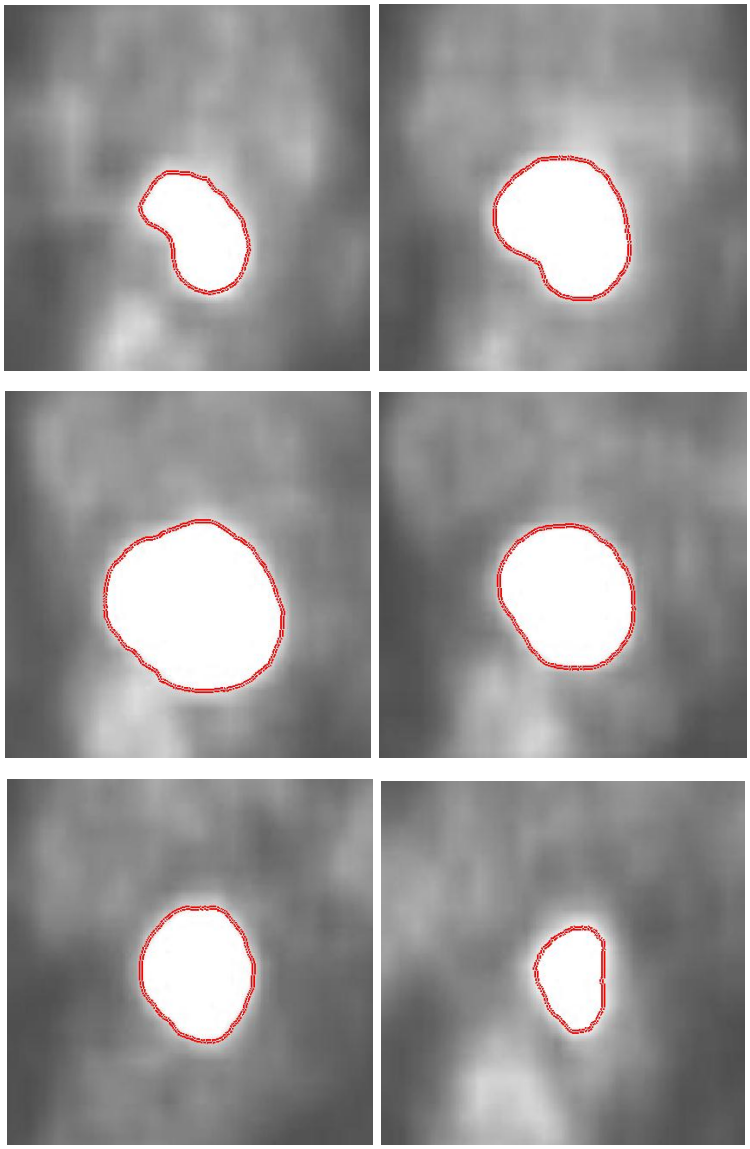

Patient no.	6
Gender	male
Age (years)	60
Patient weight (kg)	62
^{18}F-FDG injected activity (MBq)	413
Tumor volume traced by radiation oncologist (cc)	93.86
Tumor volume traced by automated algorithm (cc)	96.01
Volume mismatch (%)	2.29

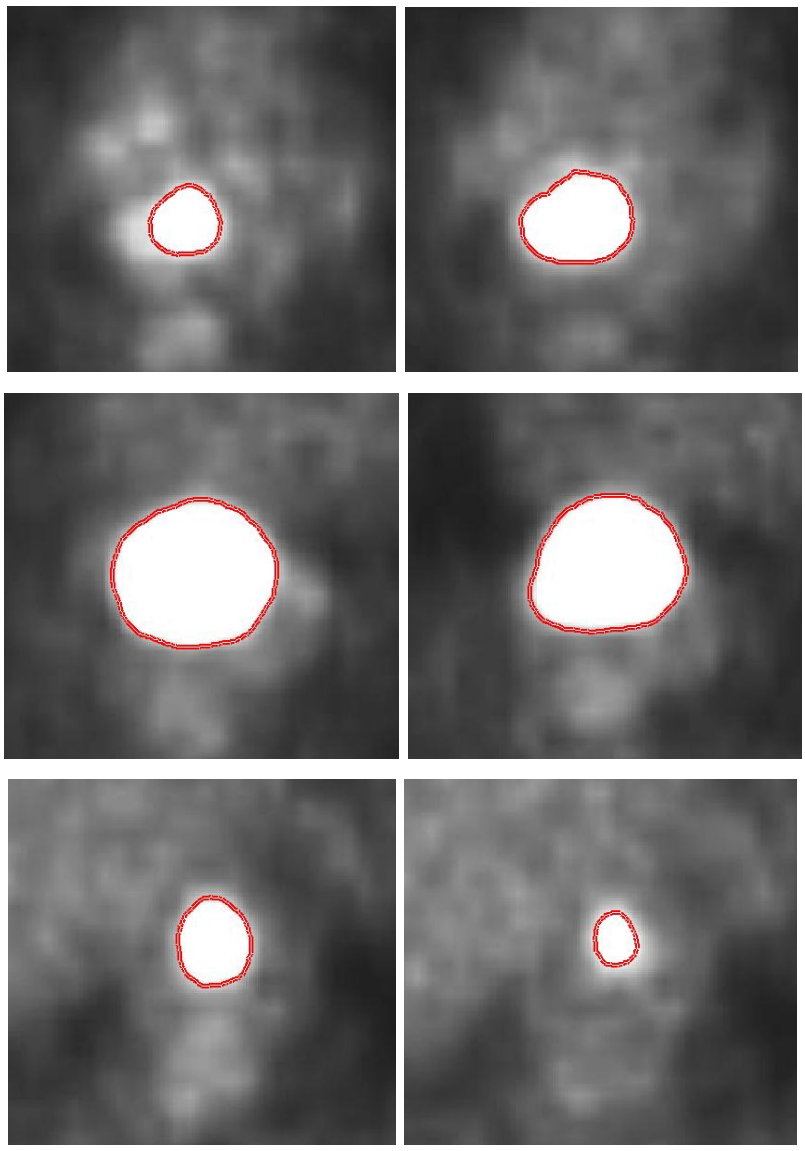

Patient no.	7
Gender	male
Age (years)	53
Patient weight (kg)	58.8
^{18}F-FDG injected activity (MBq)	329
Tumor volume traced by radiation oncologist (cc)	136.84
Tumor volume traced by automated algorithm (cc)	119.68
Volume mismatch (%)	12.54

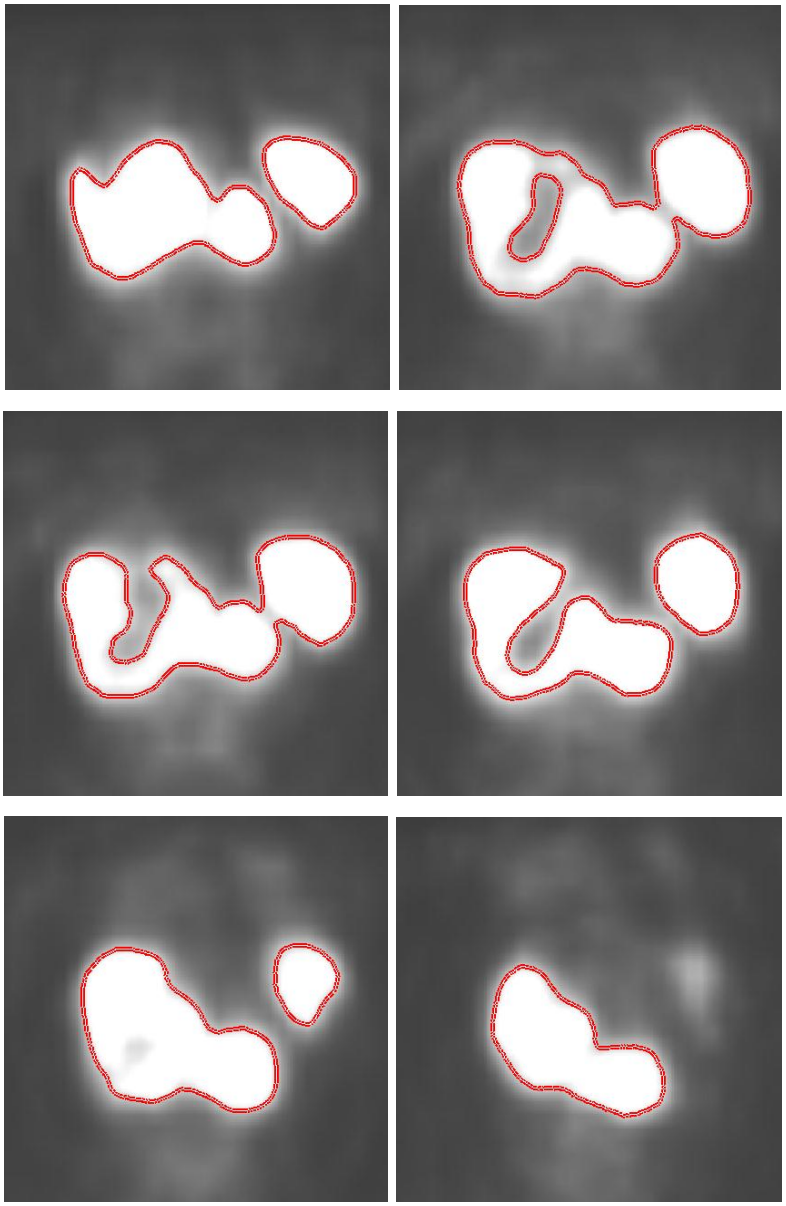

Patient no.	8
Gender	male
Age (years)	55
Patient weight (kg)	56.2
^{18}F-FDG injected activity (MBq)	345
Tumor volume traced by radiation oncologist (cc)	145.51
Tumor volume traced by automated algorithm (cc)	140.92
Volume mismatch (%)	3.15

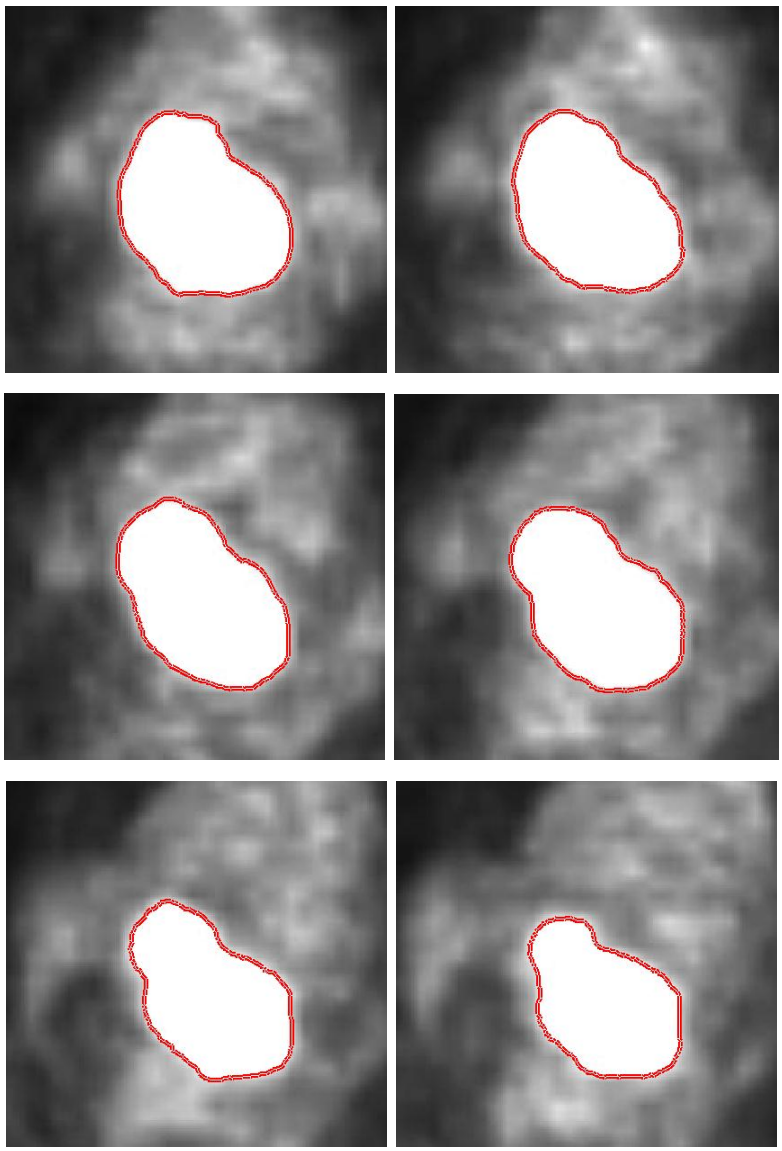

Patient no.	9
Gender	male
Age (years)	59
Patient weight (kg)	54
^{18}F-FDG injected activity (MBq)	443
Tumor volume traced by radiation oncologist (cc)	171.74
Tumor volume traced by automated algorithm (cc)	166.80
Volume mismatch (%)	2.88

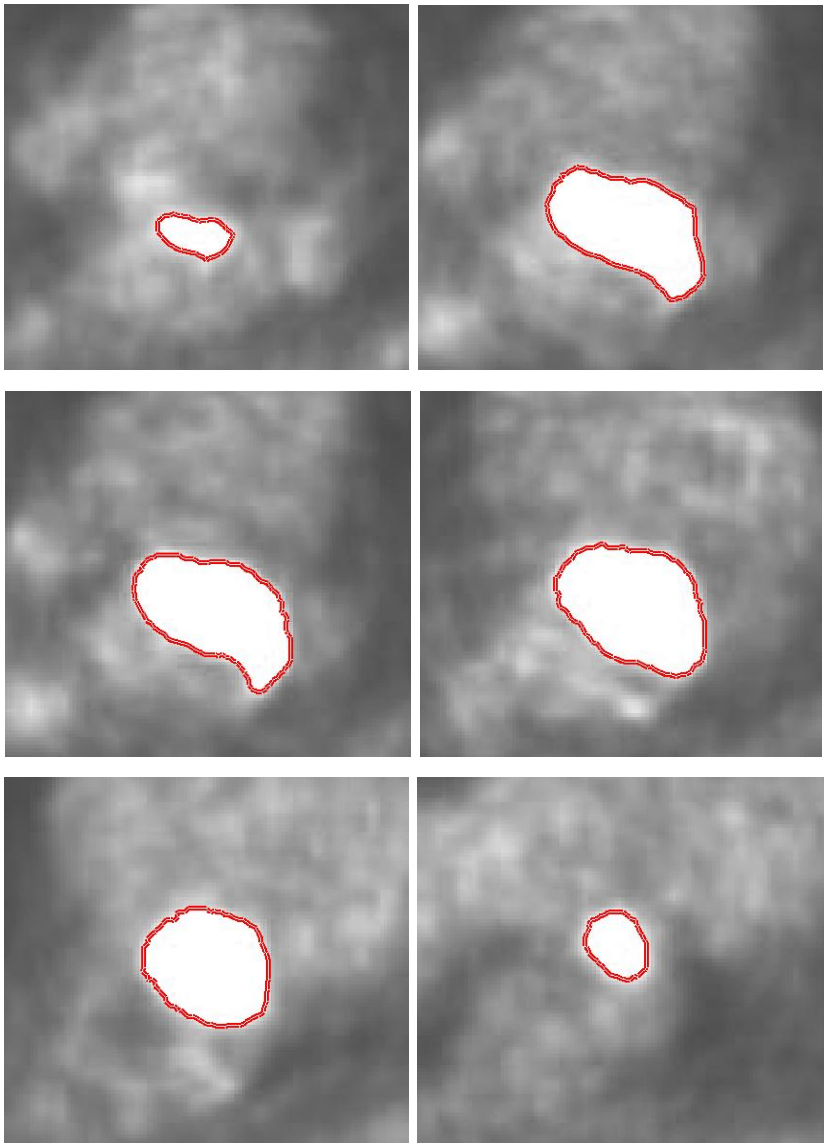

Patient no.	10
Gender	male
Age (years)	50
Patient weight (kg)	50
^{18}F-FDG injected activity (MBq)	282
Tumor volume traced by radiation oncologist (cc)	178.30
Tumor volume traced by automated algorithm (cc)	169.24
Volume mismatch (%)	5.08

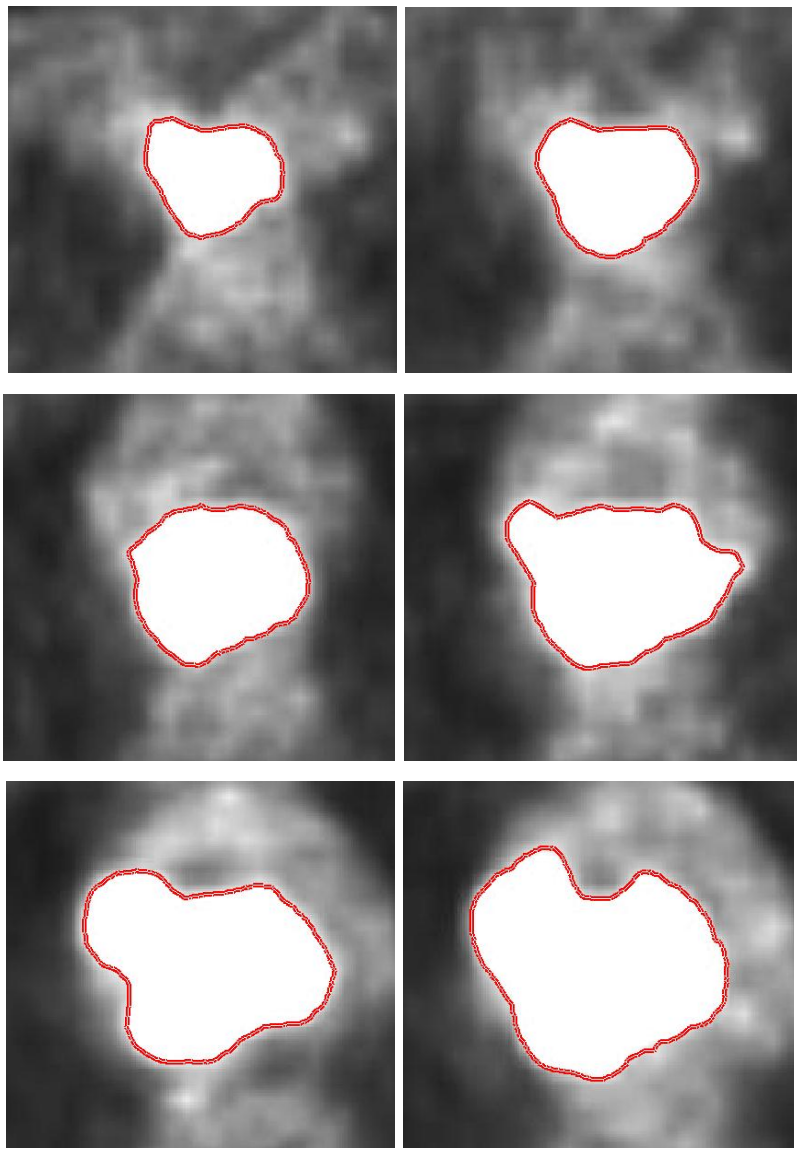

Appendix B

Performance measurement of positron emission tomography (PET)

Manufacturer: Siemens, Model Biograph 16 PET/CT HI-REZ system
Location: PET/CT center, King Chulalongkorn Memorial Hospital
Date: 2 February 2010

The characteristic performances of the PET system in terms of the spatial resolution and image quality have been tested according to NEMA NU2-2007.

1. Spatial resolution

This test is aimed to measure the tomographic spatial resolution of the PET system to ensure that it is not degraded by either the tomographic acquisition or the reconstruction process. The spatial resolution indicates the system's ability to distinguish minimal distance between two points of radioactivity in an image after image reconstruction. This test is also an important factor in determining the size of a lesion that can be detected (Daube-Witherspoon *et al.*, 2002; NEMA, 2007).

Methods

Prepare 3 ^{18}F point sources in capillary tubes with the inner diameter of less than 1 mm. Set three point sources in air at positions (a), (b) and (c) as the followings:

(a) x = 0 and y = 1 cm,

(b) x = 0 and y = 10 cm,

(c) x = 10 and y = 0 cm (figure 1). A total of 200,000 counts were acquired to obtain the tomographic PET image. The filter-back projection algorithm and all-pass filters were used for image reconstruction. All three point sources were imaged at the center of axial FOV and also at one quarter of the axial FOV away from the center. The full width at half maximum (FWHM) of the point spread function (PSF) was then measured using the *ImageJ* program to report the spatial resolution at different positions of PET image.

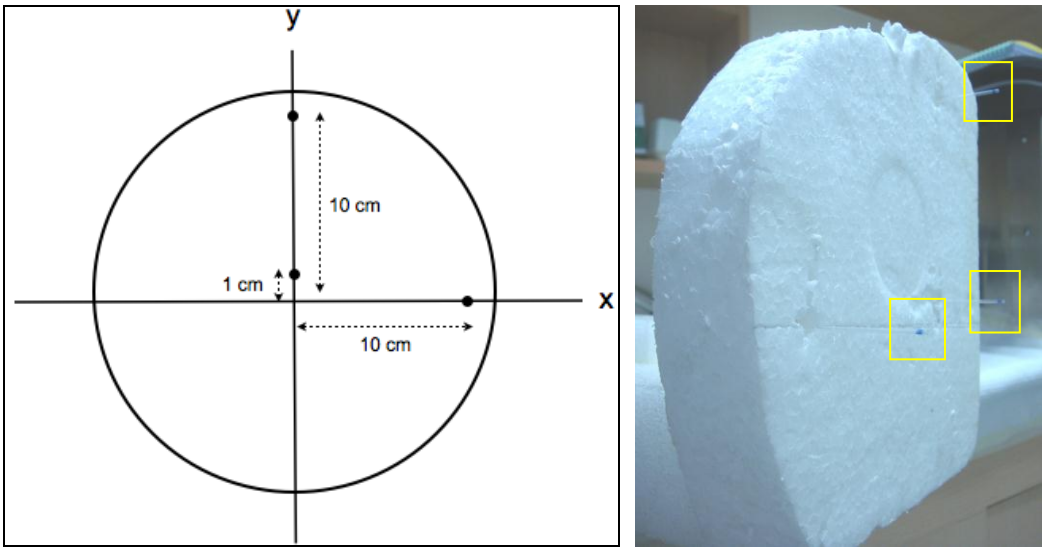

Figure 1. Position of point sources for measurement of spatial resolution.

Results

The results of the spatial resolution, FWHM of 3 point source at different positions are shown in table 1. The example of the profile at center of axial FOV to determine FWHM in *x* and *y* directions are also illustrated in figure 2 and figure 3 respectively.

Table 1. The spatial resolution, FWHM of 3 point source at different positions in air.

Position	Spatial resolution, FWHM (mm)					
	Center of FOV			Offset center ¼ FOV*		
	x-axis	*y-axis*	*average*	*x-axis*	*y-axis*	*average*
0,1	4.43	4.39	4.41	4.55	4.45	4.50
0,10	4.66	5.02	4.84	4.86	5.15	5.01
10,0	4.87	4.64	4.76	5.07	4.91	4.99

* The distance at 1/4 axial FOV = 4 cm.

Table 2. Formulas for computing spatial resolution.

Description		Formula
At 1 cm radius		
Transverse	Average *x* and *y* for both *z* positions	$\mathrm{RES} = (\mathrm{RES}x_{x=0,y=1,z=center} + \mathrm{RES}y_{x=0,y=1,z=center} + \mathrm{RES}x_{x=0,y=1,z=1/4\,FOV} + \mathrm{RES}y_{x=0,y=1,z=1/4\,FOV})/4$
Axial	Average two *z* positions (two numbers)	$\mathrm{RES} = (\mathrm{RES}z_{x=0,y=1,z=center} + \mathrm{RES}z_{x=0,y=1,z=1/4\,FOV})/2$
At 10 cm radius		
Transverse radial	Average two transverse positions for both *z* positions (four numbers)	$\mathrm{RES} = (\mathrm{RES}x_{x=10,y=0,z=center} + \mathrm{RES}y_{x=0,y=10,z=center} + \mathrm{RES}x_{x=10,y=0,z=1/4\,FOV} + \mathrm{RES}y_{x=0,y=10,z=1/4\,FOV})/4$
Transverse tangential	Average two transverse positions for both *z* positions (four numbers)	$\mathrm{RES} = (\mathrm{RES}y_{x=10,y=0,z=center} + \mathrm{RES}x_{x=0,y=10,z=center} + \mathrm{RES}y_{x=10,y=0,z=1/4\,FOV} + \mathrm{RES}x_{x=0,y=10,z=1/4\,FOV})/4$
Axial resolution	Average two transverse positions for both *z* positions (four numbers)	$\mathrm{RES} = (\mathrm{RES}z_{x=10,y=0,z=center} + \mathrm{RES}z_{x=0,y=10,z=center} + \mathrm{RES}z_{x=10,y=0,z=1/4\,FOV} + \mathrm{RES}z_{x=0,y=10,z=1/4\,FOV})/4$

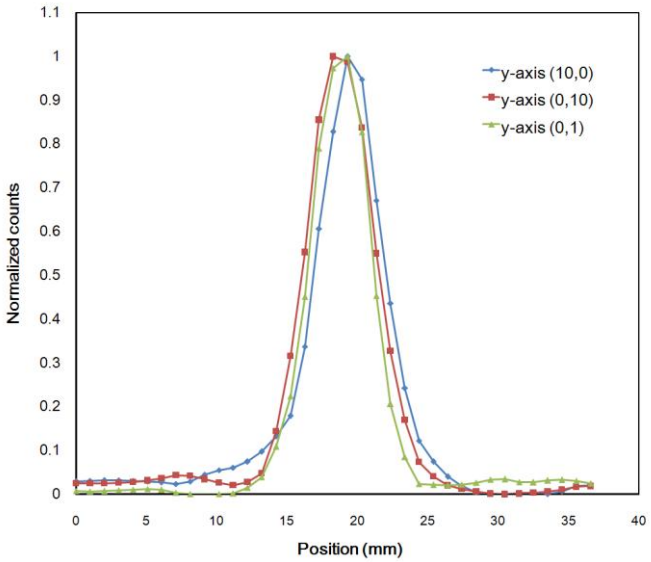

Figure 2. PSF in *y*-direction at center of axial FOV.

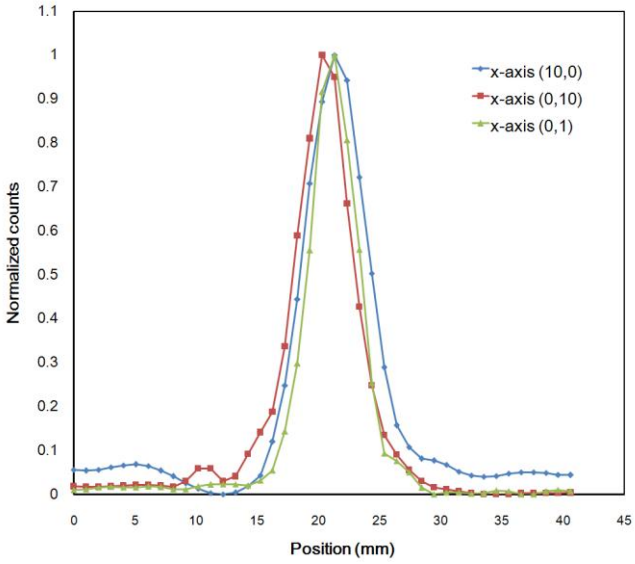

Figure 3. PSF in *x*-direction at center of axial FOV.

2. Image quality measurement

The purpose of this test is to evaluate the images quality of the PET system by simulating a whole-body imaging study with both hot and cold lesions (Erdi *et al*., 2004; IAEA human health series no.1, 2009; NEMA, 2007). The image quality measurement was performed in IEC torso phantom containing hot and cold spheres in a warm background. The four hot spheres have inner diameters of 1.0, 1.3, 1.7 and 2.2 cm, while the two larger cold spheres have inner diameters of 2.8 and 3.7 cm. A 5 cm

diameter insert with an attenuation coefficient approximately equal to the average value in lung (density 0.30 g/cc) is also placed in the center of the phantom.

Methods

The warm background within the body compartment of the phantom was first filled with ^{18}F solution activity concentration of 5.3 kBq/cc. The four hot spheres were sequentially filled with activity concentrations of 8 and 4 times of the background. The two larger cold spheres were then filled with non radioactive water. To simulate the activity outside the scanner FOV, the line source of the 70 cm scatter phantom was filled with 116 MBq (3.08 mCi) of ^{18}F solution to yield an effective activity concentration equal to the background activity concentration used in the torso phantom. Each line source was also placed together at the lower edge of the body phantom.

The acquisition protocol was set as a routine whole body protocol. Ordered subset expectation maximization (OSEM) iterative algorithm with 4 iterations and 8 subsets, matrix size of 168 x 168, slice thickness of 4 mm were used for image reconstruction.

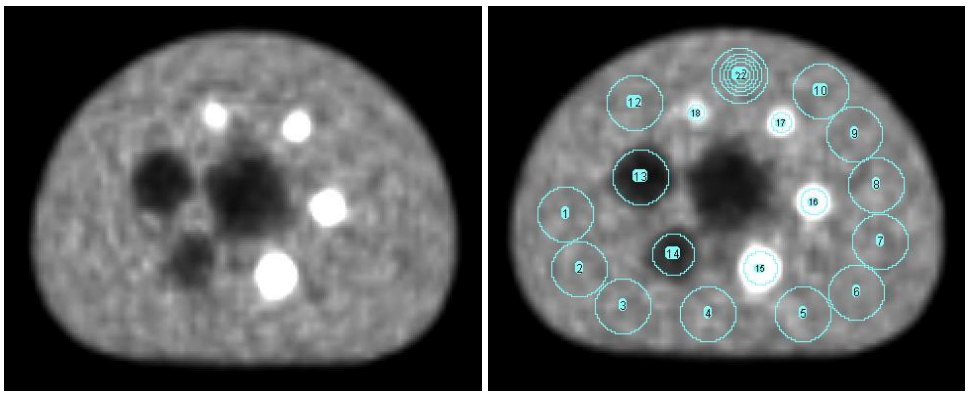

Figure 4. Example of torso phantom image (left) and placement of ROIs for quantitative analysis (right).

Analysis

The percent contrast for both hot and cold spheres were then analyzed. The background variability and residual error in the lung region were also reported. In order to determine the contrast in transverse image, the hot and cold lesions were drawn circular ROIs according to the inner diameter in each sphere. Twelve 3.7 cm diameter circular ROIs were also drawn throughout the background at a distance of 1.5 cm from the edge of the phantom (NEMA, 2007).

The percent contrast (Q_H) in hot sphere can be calculated as in (1):

$$Q_H = \frac{(C_{hot} - C_{bkgd})/C_{bkgd}}{(a_{hot} - a_{bkgd})/a_{bkgd}} \times 100 \quad (1)$$

where C_{hot} is the average counts in the ROI for each hot sphere, C_{bkgd} is the average of the background ROI counts, a_{hot} is the radioactivity concentration in the hot spheres and a_{bkgd} is the activity concentration in the background.

The percent contrast in cold sphere (Q_C) can be then computed as in (2):

$$Q_c = \frac{(C_{bkgd} - C_{cold})}{C_{bkgd}} \times 100 \quad (2)$$

where C_{bkgd} is the average of the background ROI counts and C_{cold} is the average of the counts in the ROI for each cold sphere.

The percent background variability (N) can be calculated as in (3):

$$N = (SD/C_{bkgd}) \times 100 \quad (3)$$

where SD is the standard deviation of the background ROI counts for sphere. To measure the residual error in scatter and attenuation corrections, the relative error (ΔC_{lung}) in percentage units for each slice can be calculated as in (4):

$$\Delta C_{lung} = (C_{lung}/C_{bkgd}) \times 100 \quad (4)$$

where C_{lung} is the average counts in the ROI placed over the lung insert and C_{bkgd} is the average of the twelve 3.7 cm background ROIs drawn for the image quality analysis.

Results

Table 3. Percent contrast, background variability, and lung residual error (SBR 4:1).

Sphere diameter (cm)	Contrast (%)	Background variability (%)
1.0	25.39	7.74
1.3	41.86	7.72
1.7	57.18	7.69
2.2	63.37	7.23
2.8	67.35	6.47
3.7	70.15	5.30
The residual error in the lung region	22.85	

Table 4. Percent contrast, background variability, and lung residual error (SBR 8:1).

Sphere diameter (cm)	Contrast (%)	Background variability (%)
1.0	26.43	4.84
1.3	43.55	5.22
1.7	58.19	5.90
2.2	64.39	5.07
2.8	72.05	5.94
3.7	73.63	4.64
The residual error in the lung region	20.29	

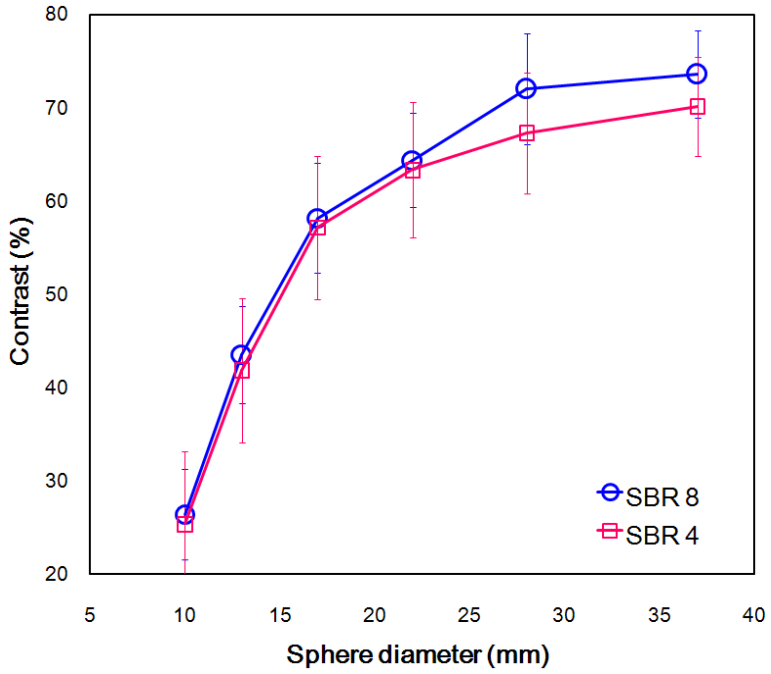

Figure 5. Percent contrast at SBR of 4 and 8.

The percent contrast of 25.39-70.15 was seen in both hot and cold spheres at SBR 4, while the percent contrast of 26.43-73.63 was observed at SBR 8. Both SBRs were reconstructed with the parameters used as in patient study (OSEM, 4 iterations and 8 subsets). Background variability of 5.30-7.74 and 4.64-5.94 were seen (the values were presented as the error bars). The residual error in lung region were 22.85 (SBR 4) and 20.29 (SBR 8) respectively. As expected, at SBR 8 provides the percent contrast better than SBR 4. The contrast was significantly different with two largest spheres. The percent contrast was increased with increasing sphere diameter at both SBRs.

Based on the IAEA human health series no.1 recommendation, the tolerance criterion should be within 5% compared to the baseline established values for all image quality parameters. According to the results, the image quality was still within the tolerance of the baseline established in 2006 (Pasawang *et al*., 2006).

Appendix C

List of publications

Journal & Proceedings

[1] Kitiwat Khamwan, Anchali Krisanachinda, Charnchai Pluempitiwiiyawej. Determination of tumor boundary on PET images using active contour coupled with optimal thresholding: a phantom study. 11th Asia-Oceania Congress of Medical Physics (AOCMP), 29 September-1 October 2011, Fukuoka, Japan (Proceedings).

[2] Kitiwat Khamwan, Anchali Krisanachida, Panya Pasawang. Determination of patient dose from ^{18}F-FDG PET/CT examination. *Radiation Protection Dosimetry* 2010; 141: 50-55.

International conferences

[3] Kitiwat Khamwan, Anchali Krisanachinda, Panya Pasawang. Optimal thresholding of volumetric ^{18}F-FDG PET images delineation. 8th South-East Asian Congress of Medical Physics (SEACOMP), 10-12 December 2010, Bandung, Indonesia.

[4] Kitiwat Khamwan, Anchali Krisanachida, Panya Pasawang. Patient effective dose from ^{18}F-FDG PET imaging, 9th Asia-Oceania Congress of Medical Physics (AOCMP) and 7th South-East Asian Congress of Medical Physics (SEACOMP), October 22-24, 2009, Chiang Mai, Thailand.

VITAE

Name	Mr. Kitiwat Khamwan
Date of birth	15 December 1980
Place of birth	Nakhonphanom, Thailand
Education	B.Sc. in Radiological Technology (1999-2003) Faculty of Allied Health Science, Naresuan University
	M.Sc. in Medical Imaging (2006-2008) Faculty of Medicine, Chulalongkorn University
	Ph.D. in Biomedical Engineering (2008-2012) Faculty of Engineering, Chulalongkorn University
Scholarships	The 90th Anniversary of Chulalongkorn University Fund (Ratchadaphiseksomphot Endowment Fund) Conference grant for Ph.D. student IAEA research assistant
Awards	1st best diagnostic radiology oral presentation from the 8th SEACOMP, Biophysics, Biomedical Engineering, December 10-12, 2010 Bandung, Indonesia.
	1st best oral presentation in imaging physics from the 9th Asia-Oceania Congress of Medical Physics (AOCMP) in conjunction with the 7th South-East Asian Congress of Medical Physics (SEACOMP), October 22-24, 2009 Chiang Mai, Thailand.
Address	233 Rama 6 Rd. Samsennai, Phayathai, Bangkok 10400